

Catalysts and Operating Conditions for Electrochemical Reduction of Carbon Dioxide

Liu, K.

DOI

[10.4233/uuid:7e395294-c8da-4f71-8422-7d0f8a2be9c8](https://doi.org/10.4233/uuid:7e395294-c8da-4f71-8422-7d0f8a2be9c8)

Publication date

2022

Document Version

Final published version

Citation (APA)

Liu, K. (2022). *Catalysts and Operating Conditions for Electrochemical Reduction of Carbon Dioxide*. [Dissertation (TU Delft), Delft University of Technology]. <https://doi.org/10.4233/uuid:7e395294-c8da-4f71-8422-7d0f8a2be9c8>

Important note

To cite this publication, please use the final published version (if applicable).
Please check the document version above.

Copyright

Other than for strictly personal use, it is not permitted to download, forward or distribute the text or part of it, without the consent of the author(s) and/or copyright holder(s), unless the work is under an open content license such as Creative Commons.

Takedown policy

Please contact us and provide details if you believe this document breaches copyrights.
We will remove access to the work immediately and investigate your claim.

Catalysts and Operating Conditions for Electrochemical Reduction of Carbon Dioxide

Kai Liu

Catalysts and Operating Conditions for Electrochemical Reduction of Carbon Dioxide

Proefschrift

ter verkrijging van de graad van doctor
aan de Technische Universiteit Delft,
op gezag van de Rector Magnificus Prof.dr.ir. T.H.J.J. van der Hagen,
voorzitter van het College voor Promoties,
in het openbaar te verdedigen op
maandag 10 oktober 2022 om 17:30 uur

door

Kai LIU

Master of Engineering in Materials Engineering, Hainan University, China
geboren te Shaanxi, China

Dit proefschrift is goedgekeurd door de:
promotoren: Prof. Dr. W. A. Smith

Prof. Dr. B. Dam

copromotor: Dr. T. E. Burdyny

Samenstelling promotiecommissie:

Rector Magnificus,	voorzitter
Prof. Dr. W. A. Smith,	Technische Universiteit Delft, promotor
Prof. Dr. B. Dam,	Technische Universiteit Delft, promotor
Dr. T. E. Burdyny,	Technische Universiteit Delft, copromotor

Onafhankelijke leden:

Prof.dr. F.M. Mulder	Technische Universiteit Delft
Prof.dr. S. Gimenez	Universitat Jaume I de Castello, Spain
Dr. S. Hernandez	Politecnico di Torino, Italy
Dr. Y. C. Li	University at Buffalo, the State University of New York, USA
Prof.dr.ir. J.T. Padding	Technische Universiteit Delft, reservelid

The work described in this thesis was carried out in the Materials for Energy Conversion and Storage (MECS), Department of Chemical Engineering, Faculty of Applied Sciences, Delft University of Technology. This work was funded by China Scholarship Council.



Front & back cover: Designed by Jing Liu.

Printed by: Ridderprint | www.ridderprint.nl

Copyright © 2022 by K. Liu

ISBN 978-94-6458-605-3

An electronic version of this dissertation is available at

<http://repository.tudelft.nl/>.

Contents

WHY ELECTROCHEMICAL REDUCTION OF CO ₂ DESERVES OUR EFFORTS.....	1
1.1 Introduction	2
1.2 Renewable Energy.....	3
1.3 The Gap between Current Warming Trends and Our Dream Goal	4
1.4 Electrochemical Reduction of CO ₂	6
1.5 Thesis Outline and Research Questions	9
References	10
INFLUENCES OF CATALYSTS AND THE LOCAL REACTION ENVIRONMENT ON CO ₂ RR.....	13
2.1 Introduction	14
2.2 Catalysts for Carbon Dioxide Reduction.....	15
2.3 The Local Reaction Environment around the Catalyst in a Gas-Diffusion Electrode System	19
2.4 Operating Conditions of GDE Experiments	27
References	32
ELECTRONIC EFFECTS DETERMINE THE SELECTIVITY OF PLANAR AU-CU BIMETALLIC THIN FILMS FOR ELECTROCHEMICAL CO ₂ REDUCTION.....	37
3.1 Introduction	38
3.2 Results and Discussion	40
3.3 Conclusions	54
3.4 Experimental Section.....	55
References	57
Supporting Information for Chapter 3	63
EXPERIMENTAL INTRICACIES OF PERFORMING CO ₂ REDUCTION AT HIGHER CURRENT DENSITIES USING GAS-DIFFUSION LAYERS	75
4.1 Introduction	76
4.2 Results and Discussion	77
4.3 Conclusions	84
4.4 Experimental Section.....	84
References	86
Supporting Information for Chapter 4	89
HOW LOCAL REACTION AND PROCESS CONDITIONS INFLUENCE CO ₂ REDUCTION TO MULTICARBON PRODUCTS ON COPPER GAS-DIFFUSION ELECTRODES	93

5.1 Introduction	94
5.2 Results and Discussion	96
5.3 Conclusions	109
5.4 Experimental Section.....	110
References	111
Supporting Information for Chapter 5	117
SUMMARY AND OUTLOOK	141
SAMENVATTING EN VOORUITZICHT	145
ACKNOWLEDGEMENTS	149
LIST OF PUBLICATIONS.....	153
CURRICULUM VITAE	155

Why Electrochemical Reduction of CO₂ Deserves Our Efforts

1

1.1 Introduction

The Earth's global average temperature has continuously increased since 1850, using the average temperature of the period between 1961 and 1990 as the baseline. Figure 1.1 clearly shows that the global average temperature has increased by $>1\text{ }^{\circ}\text{C}$ in the past 170 years. During the last 30 years in particular, the global temperature has risen alarmingly, which is approximately $0.7\text{ }^{\circ}\text{C}$ higher than the baseline. Almost all of the warming can be ascribed to the greenhouse gas emissions from human activities since the pre-industrial era, as asserted in the report of the Intergovernmental Panel on Climate Change (IPCC).^[1]

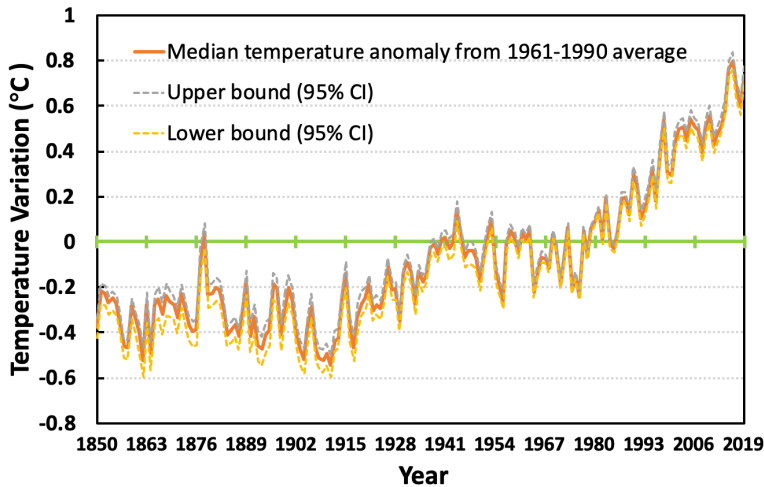


Figure 1.1: Global average temperature. The green horizontal solid line at $0\text{ }^{\circ}\text{C}$ represents the average temperature from 1961 to 1990. The orange solid line represents the median average temperature change. The grey and yellow dashed lines represent the upper and lower 95% confidence intervals, respectively. Adapted from Ref [2]. Data published by Met Office Hadley Centre and details of the dataset in Ref [3].

Greenhouse gases (GHG) can absorb heat and gradually radiate it over time, providing a link between atmospheric GHG concentration and global temperatures. This link has existed for millions of years due to natural cyclings of GHG concentrations in the atmosphere, especially with CO_2 as the major compositional greenhouse gas.^[4] The rapid anthropological

increase in GHG's has then led to rapidly increasing global average temperature over the past hundred years. In modern ages, the increased greenhouse gases are a result of increased energy demand, agriculture and feedstock production which require the consumption of fossil fuels that emit CO_2 as a waste product (as shown in Figure 1.2).

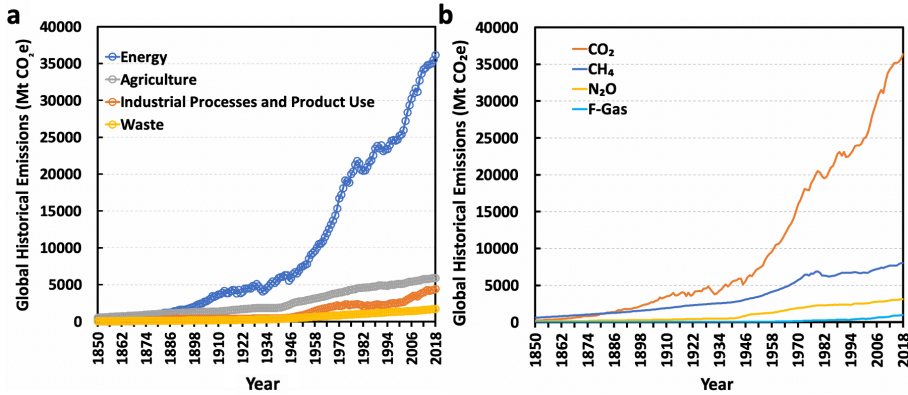


Figure 1.2: (a) The historical green-house gas emitted from different human activities. (b) The historical emissions of carbon dioxide (CO_2), methane (CH_4), nitrous oxide (N_2O) and fluorinated gases (F-gas). Data published by Refs [5] and [6].

1.2 Renewable Energy

For the sake of halting anthropogenic global warming, we need to delink the growing energy demand needed to maintain our society, and CO_2 emissions. In an ideal setting, our lifestyles that depend on substantial energy and carbon-based compounds can be maintained, without the bad side effects of climate change. If most of the current power sources can be replaced by renewable energy, we can achieve this goal while directly cutting off a huge amount of the CO_2 emissions.

Instead of burning fossil fuels, non-emission energy – “green energy” – techniques have been developed and brought into industrials, such as solar panels, wind turbines, hydropower plants, and some other renewable energy sources. In the past decades, these zero-emission energy sources have

developed rapidly. Nowadays, nearly 30% of the total electricity comes from renewables. (shown in Figure 1.3b)

Despite this progress there still remains a large amount of electricity generation derived from fossil fuels. And further, electricity generation only accounts for about 30% of all energy usage. Thus, renewable energy in the form of electricity must somehow find a way to replace fossil fuels that utilized as a transportation fuel, heating source and chemical feedstock (plastics, steel, etc.). The only way this can be done is by pairing a renewable energy source with a chemical transformation technology and renewable base molecules such as water, CO₂ and nitrogen.

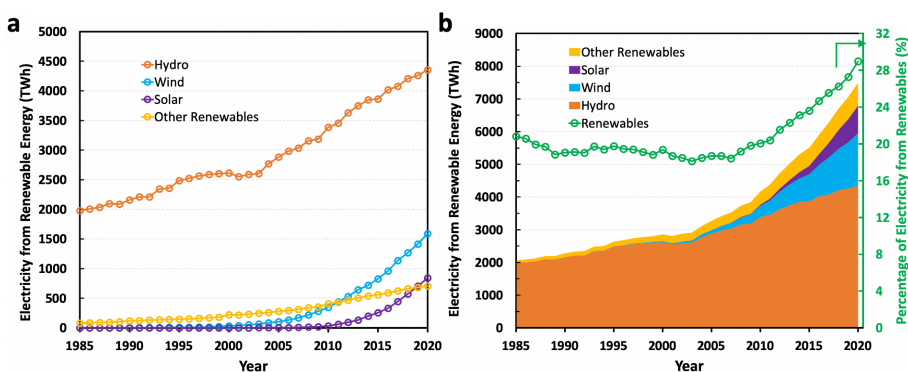


Figure 1.3: (a) Global renewable energy generation and (b) the growth of total renewable energy and share of electricity production from renewables. Data published by Refs [7] and [8].

1.3 The Gap between Current Warming Trends and Our Dream Goal

Most of the world's global governments and individuals in society have realized and agreed with the importance of lowering CO₂ emissions, and have been putting more and more efforts to addressing the core causes, especially as it relates to developing and deploying renewable energy generation technologies. Although current climate policies will reduce CO₂ emissions, their impact may be too slow to meet our targets of warming control. (shown

in Figure 1.4) Further, the lowest hanging fruit of electricity generation is becoming harder and harder to supplant at higher percentages.

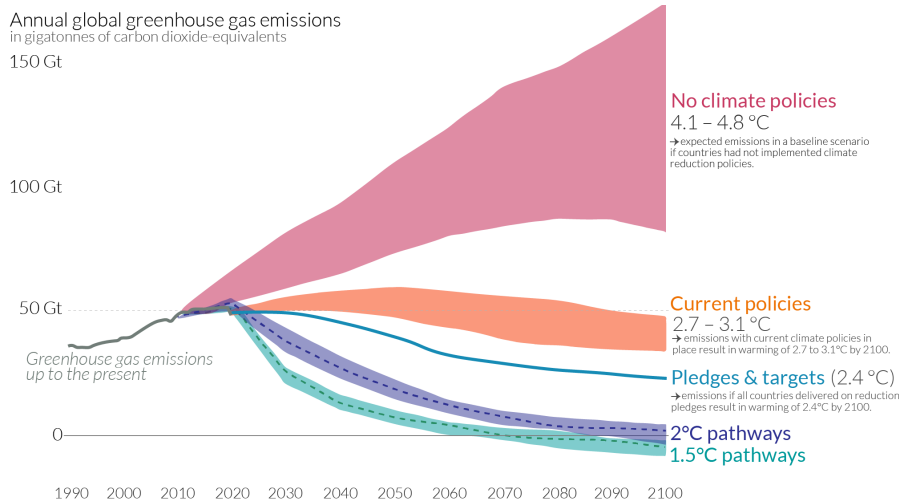


Figure 1.4: Global greenhouse gas emissions and warming prospect. Adapted from Ref [2].

Obviously, the application of non-emission energy alone cannot reduce the already high atmospheric CO₂ concentration. Additionally, due to the “lag” between GHG concentrations and final temperature increase, which means the later we reach the emission peak, the more drastic reduction we need^[9,10]. In the future, we then need to not only reduce the emissions, but also diminish the excessive CO₂ in the atmosphere. For these reasons the combination of renewable energy and chemical technologies is essential. However, the technological options to convert renewable electricity into things like plastics, ammonia, kerosene, etc. are surprisingly limited. The two most available approaches are thermochemical and electrochemical conversion technologies, which use electricity from renewable sources as a driver to convert water, CO₂ and nitrogen into fuels and feedstocks. (as shown in Figure 1.5)

The thesis focuses on research into the electrochemical route to reduce atmospheric CO₂ concentrations through the novel technology of electrochemical CO₂ reduction.

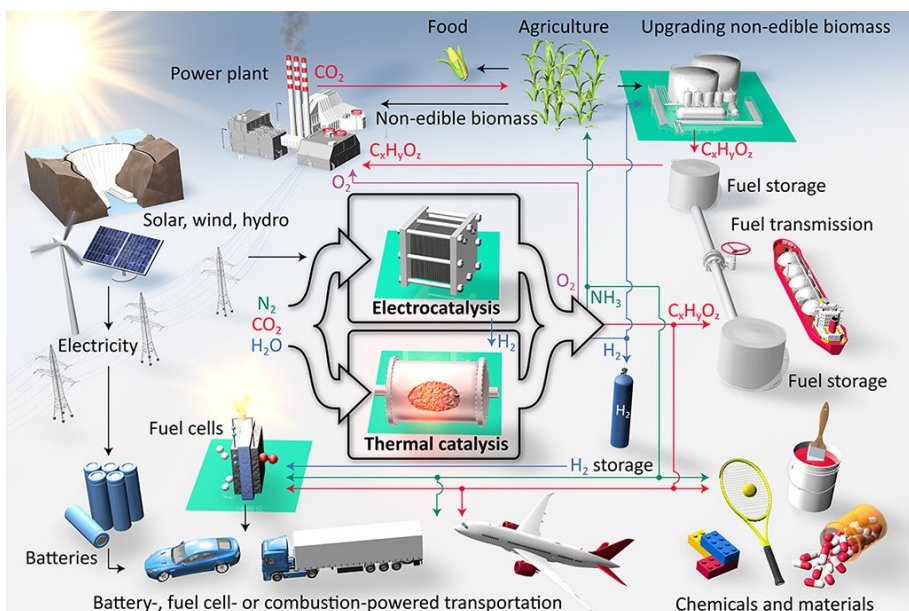


Figure 1.5: Future approaches of sustainable techniques. Adapted from EU Energy-X project in Ref [11].

1.4 Electrochemical Reduction of CO₂

Currently, our society still largely relies on the fossil energy, although it has caused tremendous amounts of CO₂ emissions. If we could reuse the generated CO₂ instead of releasing it into the atmosphere, it would be the most effective way to cut off the CO₂ emissions. The approach based on electrochemical reduction of CO₂ can create an artificial carbon cycle integrated with renewable electricity, in which CO₂ is converted into valuable chemicals, economically improving the energy efficiency. Promisingly, this technical method can play a key role in dealing with the challenges of global warming, helping us reshape our energy paradigm and move towards a sustainable society in the next decades. The challenge facing researchers today is to improve the technical and economic aspects of this technology in order for it to be a globally applied technology that meaningfully impacts emissions.

Systematic research on electrochemical reduction of CO_2 started in the 1980s with the pioneering work of Hori and coworkers. Their foundational studies on pure transition metallic catalysts have attracted and inspired great efforts devoted to the exploration of CO_2 reduction reaction (CO_2RR). Due to a lack of global interests in climate change at the time, however, there was a lack of additional researchers and funding to pick this research up. This has since changed, and now the field of electrochemical CO_2 reduction is moving at a fast pace with multiple large advancements made each year, in addition to a growing number of start-up companies.

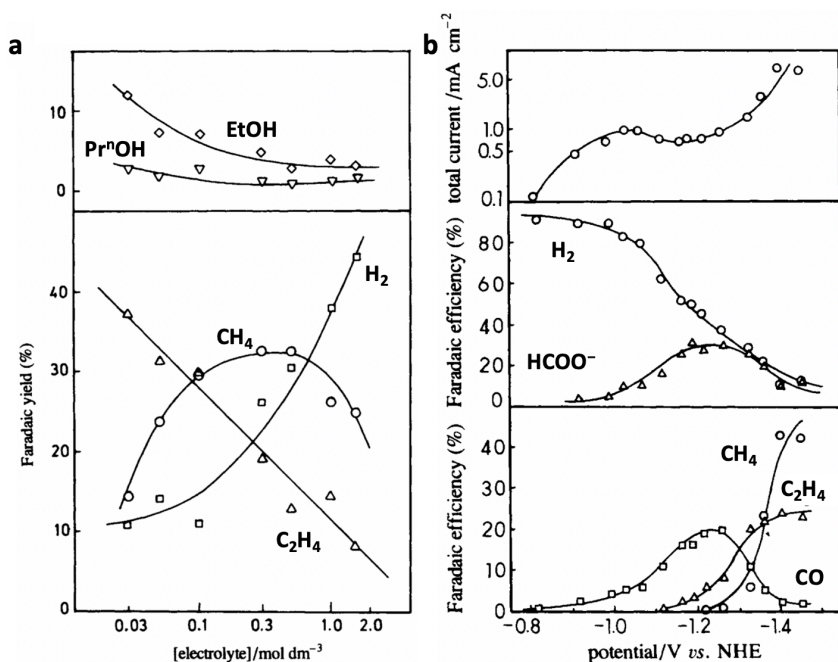


Figure 1.6: Hori's pioneering works of CO_2 reduction on polycrystalline Cu. The relationship between (a) the electrolyte concentration, and (b) CO_2RR onset potential, and the Faradaic efficiency of detected products. Adapted from Ref [12].

Overviewing the foundational CO_2RR research done by Hori, the monometallic cathode materials can be categorized into four groups based on the products selectivities: (1) post-transition metals that convert CO_2 to formate, e.g. Sn, In and Pb; (2) carbon monoxide (CO) is the dominant product on metals like Au, Ag and Zn; (3) copper as the only metal that can

produce up to several different kinds of products, including hydrocarbons, alcohols, formate, CO, with a wide distribution; (4) metals favor hydrogen evolution reaction (HER) with low CO₂RR activity, e.g. Pt, Ni, Fe.^[13, 14] (as shown in Figure 1.7)

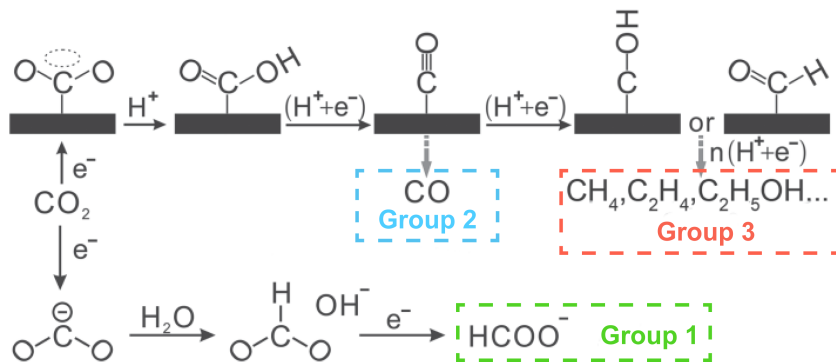


Figure 1.7: Reaction mechanisms of CO₂ reduction on different metallic electrocatalysts in aqueous solutions. Adapted from Ref [15].

Combinations of these materials, variations in their morphology and facets, and the quantity of catalysts within a system all impact the observed performance metrics towards CO₂ reduction products, thus making the testing domain vast. For several years this type of research was dominant within the field until over potentials became drastically reduced and product selectivity became more reputable.

In recent years, great efforts have been devoted to the catalyst engineering, theoretical simulation and reactor design. These intensive studies have extended the fundamental research towards industrial applications, while showing that device engineering can greatly enhance the intrinsic behavior of the utilized catalysts. Modern day research now combines the best of both worlds, to lead to performance metrics warranting even pilot scale testing of the technology. Despite these advancements, many uncertainties and questions remain, leaving room for researchers to continue advancing the field.

1.5 Thesis Outline and Research Questions

This thesis is composed of five chapters. In Chapter 2 an overview of CO₂ electrolysis is presented from the perspective of how experimental parameters can tune the local reaction environment and thus vary electrochemical performance. Chapter 3 then presents a work published in ACS Applied Materials and Interfaces examining bimetallic catalysts and their CO₂RR performance. Chapter 4 sets focus on the discussion over operating conditions of gas-diffusion electrodes, which has been published in ACS Energy Letters. And lastly, in Chapter 5, the work investigates how the surrounding reaction environment near Cu surfaces under various operating conditions impacts CO₂ reduction performance.

The following research questions for this PhD thesis are addressed through several of these scientific chapters. Namely:

- What are the influences of catalysts and the local reaction environment on CO₂ electrolysis? (Chapter 2)
- Can bimetallic thin films of Au-Cu improve multicarbon product formation? (Chapter 3)
- What are the experimental intricacies of performing CO₂ reduction at higher current densities on gas-diffusion layers? (Chapter 4)
- How do local reaction and process conditions affect CO₂ reduction to multicarbon products on copper gas-diffusion electrodes? (Chapter 5)

Lastly, the summary provides conclusions for the broader research field as determined from this thesis work.

References

- (1) IPCC, **2014**: Climate Change 2014: Synthesis Report. Contribution of Working Groups I, II and III to the Fifth Assessment Report of the Intergovernmental Panel on Climate Change [Core Writing Team, R.K. Pachauri and L.A. Meyer (eds.)]. IPCC, Geneva, Switzerland, 151.
- (2) Hannah Ritchie and Max Roser (**2020**) - "CO₂ and Greenhouse Gas Emissions". Published online at OurWorldInData.org. Retrieved from: 'https://ourworldindata.org/co2-and-other-greenhouse-gas-emissions' [Online Resource]
- (3) Morice, C. P., J. J. Kennedy, N. A. Rayner, & P. D. Jones (**2012**), Quantifying uncertainties in global and regional temperature change using an ensemble of observational estimates: The HadCRUT4 dataset, *J. Geophys. Res.*, 117, D08101, doi:10.1029/2011JD017187
- (4) Lacis, A. A., Schmidt, G. A., Rind, D., & Ruedy, R. A. (**2010**). Atmospheric CO₂: Principal control knob governing Earth's temperature. *Science*, 330(6002), 356-359.
- (5) Gütschow, J.; Günther, A.; Jeffery, L.; Gieseke, R. (**2021**): The PRIMAP-hist national historical emissions time series v2.2 (1850-2018). zenodo. doi:10.5281/zenodo.4479172.
- (6) Gütschow, J.; Jeffery, L.; Gieseke, R.; Gebel, R.; Stevens, D.; Krapp, M.; Rocha, M. (**2016**): The PRIMAP-hist national historical emissions time series, *Earth Syst. Sci. Data*, 8, 571-603, doi:10.5194/essd-8-571-2016
- (7) Global Carbon Project. (**2021**). Supplemental data of Global Carbon Project 2021 (1.0) [Data set]. Global Carbon Project. <https://doi.org/10.18160/gcp-2021>.
- (8) Andrew, Robbie M., & Peters, Glen P. (**2021**). The Global Carbon Project's fossil CO₂ emissions dataset [Data set]. Zenodo. <https://doi.org/10.5281/zenodo.5569235>.
- (9) Mitchell, J. F. B., Johns, T. C., Ingram, W. J., & Lowe, J. A. (**2000**). The effect of stabilising atmospheric carbon dioxide concentrations on global and regional climate change. *Geophysical Research Letters*, 27(18), 2977-2980.

-
- (10) Samset, B.H., Fuglestad, J.S. & Lund, M.T. Delayed emergence of a global temperature response after emission mitigation. *Nature Communications*, 11, 3261 (2020). <https://doi.org/10.1038/s41467-020-17001-1>.
- (11) EU Energy-X project. Research needs towards sustainable production of fuels and chemicals. [<https://www.energy-x.eu/about/>]
- (12) Hori Y., Murata A., & Takahashi R. Formation of hydrocarbons in the electrochemical reduction of carbon dioxide at a copper electrode in aqueous solution. *J Chem Soc Faraday Trans.* **1989**;1(85):2309-2326.
- (13) Hori, Y., Kikuchi, K., & Suzuki, S. Production of CO and CH₄ in Electrochemical Reduction of CO₂ at Metal Electrodes in Aqueous Hydrogencarbonate Solution. *Chemistry Letters*, **1985**. 14(11): p. 1695-1698.
- (14) Tomita, Y., Teruya, S., Koga, O., & Hori, Y. Electrochemical Reduction of Carbon Dioxide at a Platinum Electrode in Acetonitrile-Water Mixtures. *Journal of The Electrochemical Society*, **2000**. 147(11): p. 4164-4167.
- (15) Zhu, D.D., Liu, J.L., & Qiao, S.Z., Recent Advances in Inorganic Heterogeneous Electrocatalysts for Reduction of Carbon Dioxide. *Advanced Materials*, **2016**. 28(18): p. 3423-3452.

Influences of Catalysts and the Local Reaction Environment on CO₂RR

2

This chapter of the thesis introduces the variety of ways in which the catalyst and the surrounding reaction environment directly influences the electrochemical reduction of CO₂. The chapter begins with a discussion of the catalysts utilized for CO₂RR and a brief overview of factors influencing catalytic activity, which motivated the published work presented in Chapter 3. Greater discussion is then given to discussing the local reaction environment occurring in the electrolyte, which in recent years has been given even greater emphasis in the research field. Extra emphasis will be specifically given to gas-diffusion electrode architectures, though many of the phenomena first are described microscopically such as through the choice of cations or electrolyte concentrations. The end of Chapter 2 will then describe how macroscopic operating effects such as catholyte flow rate or system stability change the local reaction environment and thus CO₂RR. These latter discussions are relevant for the work presented in Chapters 4 and 5 of this thesis.

2.1 Introduction

Electrocatalysts are the central active component in electrolysis systems and have attracted substantial attention from researchers in the past years. In the CO₂RR field numerous catalysts have been developed by varying the type of electrode material, morphology and surface area among others. These catalysts have been examined under a subset of operating conditions in a variety of cell architectures. Such variations in experimental setups and the wide variability in the performance of similar controlled catalysts reported in various works (e.g. polycrystalline copper), however, have shed light on the importance the local reaction environment on CO₂RR performance metrics. Thus, while catalysts are critically important, they do not solely govern the overall catalytic performance. In some cases, a suitable reaction environment plays an even more dominant role.

The local reaction environment is loosely defined in literature but represents the region in the near vicinity of the electrode which can influence the various steps of CO₂RR. It consists of the catalyst's surface, the double layer and the local species in the finite region, and can be strongly influenced by the electrolyzer design and operating conditions. In the past decades, there are abundant mechanistic studies based on well-established models that are derived from relatively steady local reaction environments within conventional electrochemical cells and mild operating conditions. Compared to those moderately varied local circumstances, direct gas-feed systems, such as gas-diffusion electrode (GDE), possessing an opposite and effective CO₂ supply pathway, help to build up diversified local reaction environments, realizing the examinations of CO₂RR under various critical conditions that are constrained in conventional H-type cells.

Recently, researches have shown that the local reaction environment can be modified by different means (thermodynamically, physically), leading to an abrupt change in performance. Therefore, the synergetic effects originated/derived from the whole experimental system determine the observed catalytic performance. This chapter focuses on the discussion of catalysts, local species and operating conditions as well as their influences on

the construction of a local reaction environment for electrochemical CO₂ reduction.

2.2 Catalysts for Carbon Dioxide Reduction

Activation of carbon dioxide

The activation of a linear aqueous CO₂ molecule is the initial step of CO₂RR. Without electrocatalysts, the activation of CO₂ reduction is considered to be difficult, due to the stability of CO₂ molecule and the very negative redox potential for the first electron transfer to form the CO₂^{•−} radical intermediate. Owing to the feasible stabilization of CO₂^{•−} radical or other intermediates on the surface of electrocatalysts, a much less negative required potential can be achieved.^[1]

Table 2.1: Representative standard potentials for electroreductions of CO₂ in aqueous solutions.

Cathodic half-reaction	<i>E</i> ^o vs. SHE (V) at pH 7
CO ₂ (g) + e [−] → *COO [−]	−1.90
CO ₂ (g) + 2H ⁺ + 2e [−] → HCOOH (l)	−0.61
CO ₂ (g) + H ₂ O (l) + 2e [−] → HCOO [−] (aq) + OH [−]	−0.43
CO ₂ (g) + 2H ⁺ + 2e [−] → CO (g) + H ₂ O (l)	−0.53
CO ₂ (g) + H ₂ O (l) + 2e [−] → CO (g) + 2OH [−]	−0.52
CO ₂ (g) + 4H ⁺ + 2e [−] → HCHO (l) + H ₂ O (l)	−0.48
CO ₂ (g) + 3H ₂ O (l) + 4e [−] → HCHO (l) + H ₂ O (l)	−0.89
CO ₂ (g) + 6H ⁺ (l) + 6e [−] → CH ₃ OH (l) + H ₂ O (l)	−0.38
CO ₂ (g) + 5H ₂ O (l) + 6e [−] → CH ₃ OH (l) + 6OH [−]	−0.81
CO ₂ (g) + 8H ⁺ + 8e [−] → CH ₄ (g) + 2H ₂ O (l)	−0.24
CO ₂ (g) + 6H ₂ O (l) + 8e [−] → CH ₄ (g) + 8OH [−]	−0.25
2CO ₂ (g) + 12H ⁺ + 12e [−] → C ₂ H ₄ (g) + 4H ₂ O (l)	0.06
2CO ₂ (g) + 8H ₂ O (l) + 12e [−] → C ₂ H ₄ (g) + 12OH [−]	−0.34
2CO ₂ (g) + 12H ⁺ + 12e [−] → CH ₃ CH ₂ OH (l) + 3H ₂ O (l)	0.08
2CO ₂ (g) + 9H ₂ O (l) + 12e [−] → CH ₃ CH ₂ OH (l) + 12OH [−] (l)	−0.33

As seen in Table 2.1, due to the multiple electrons and protons required for CO₂RR products, a series of transfer steps are needed to obtain a certain product. For some catalysts multiple reaction products are also possible (e.g.

both CO and HCOO^- are possible on Ag). It is then challenging to directly regulate product selectivity for species formed at similar thermodynamic potentials. Many approaches in research have attempted to overcome this challenge through the rational design of electrocatalysts, where the CO_2RR activity of different reactions can be promoted through feasible reaction pathways towards desired products.

Intrinsic catalyst activity

In line with the above goal of selectively producing singular products, as well as doing so at the lowest overpotential, efforts have been taken to understand and improve intrinsic catalytic activity. The binding energy of key intermediates in the rate-limiting step is known to drive the observed outputted reaction activity. As such binding energies are a key means of finding better catalysts and comparing the activity of existing ones.

Based on the Sabatier principle, an optimal binding energy of key CO_2RR intermediates to a catalytic surface will exist, and lead to the maximum activity (as illustrated in Figure 2.1).^[2, 3] For example, with a very weak binding energy, the adsorption of reactants may not be stable enough on the catalyst's surface for further electrochemical reduction, instead desorbing. However, with a too high binding energy, the active sites may be occupied by the adsorbents instead of releasing the products and capturing other reactive species, resulting in surface poisoning and/or a low turnover number.^[4] Au possesses the optimal CO binding strength and exhibits the highest CO_2RR activity among other metals (shown in Figure 2.1). With a moderately tighter CO binding, Cu can maintain a high surface coverage of CO and further reduce the absorbed CO at a relatively low onset potential (indicated in Figure 2.1b).

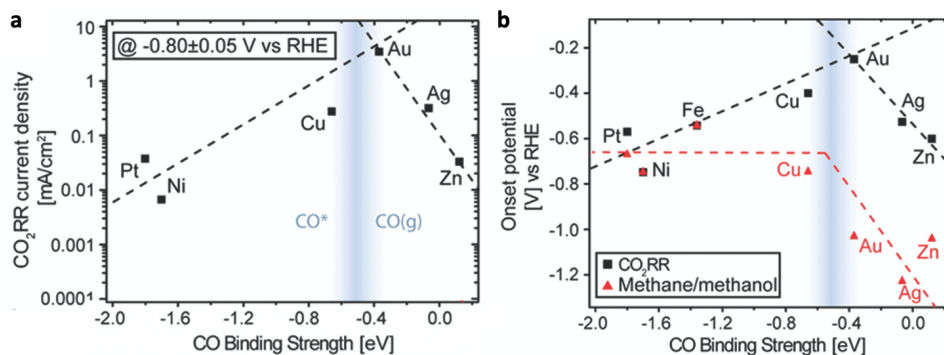


Figure 2.1: (a) Volcano plot of partial current density for CO₂RR vs CO binding strength. (b) The onset potentials of overall CO₂RR and methane/methanol as a function of CO binding energy. The vertical lines labeled refer to the thermodynamics of chemical CO adsorption/desorption, indicating the favored adsorbed state as CO* on the left and desorbed state as CO(g) on the right. Adapted from Ref [2].

Strategies to improve catalytic performance

In order to develop electrocatalysts with improved activity (or reaction rate) for CO₂RR, there are then two general approaches which can be used: (1) increasing the number of active sites in a defined electrolysis area, or (2) increasing the intrinsic activity of each active site.^[5]

In this first strategy, the number of active sites can be increased through the rational design of larger electrode nanostructures and/or through the precise control of particle size (as shown in Figure 2.2).^[6, 7] However, upon electroreduction many electrocatalysts undergo restructuring either due to the removal of an oxide layer, sintering, Ostwald ripening or even catalytic dissolution in the electrolyte. Higher surface area catalysts are a very important and easy strategy to boost activity, but these methods should result in stable surface areas over time.

The second strategy to increase the intrinsic activity of a desired reaction (or decrease the intrinsic activity of an undesired reaction), has a number of more design possibilities. The tuning of binding energy could be a relatively manageable strategy to develop metallic catalysts. Ideally, alloying offers a

promising approach to design catalyst with desired CO₂ performance, via the binding energy and/or active sites.^[8-10]

For boosting of CO₂ reduction activity with suppression of competing reaction, the decoration of the electrode with low HER activity adatoms has proven to be an effective approach. In one example Pb adatoms could be deposited onto a Cu cathode at active sites for HER or CO₂RR, thus weakening the *H adsorption and stabilizing the *OCHO intermediate, resulting in the significantly improved overall CO₂RR activity.^[11] Without adatoms, researchers have modified CO₂RR activity through a variety of other approaches such grain boundary^[12, 13] and lattice strain^[14] effects. In many of these claims, however, direct evidence of the mechanisms for increased activity remains challenging to confirm. Many reported examples may need additional efforts to remove the possibility of other factors playing a role in the observed change in CO₂RR and HER performance.^[15]

This said, by utilizing catalysts with improved intrinsic activity, the enhancement in the reaction activity can be more than 10 orders of magnitude, which is 3 or 10 orders of magnitude higher than that of simply increasing the mass loading of pristine catalysts.^[5, 16] Thus increasing intrinsic activity is a desired strategy which can afterwards be coupled to greater surface areas. However, this kind of significantly improved activity in high-energy required reactions can be concealed under high voltages due to CO₂ mass transport limitations at high reaction rates (as shown in Figure 2.2). With sufficient CO₂ supply in the direct gas-fed electrolyzers (e.g. GDE), it offers decent environments to examine the actual catalyst performance under various conditions.

In addition to the intrinsic activity, the surrounding chemical environments of electrocatalysts synergistically play a significant role in boosting the CO₂RR selectivities, which is discussed in the following sections.

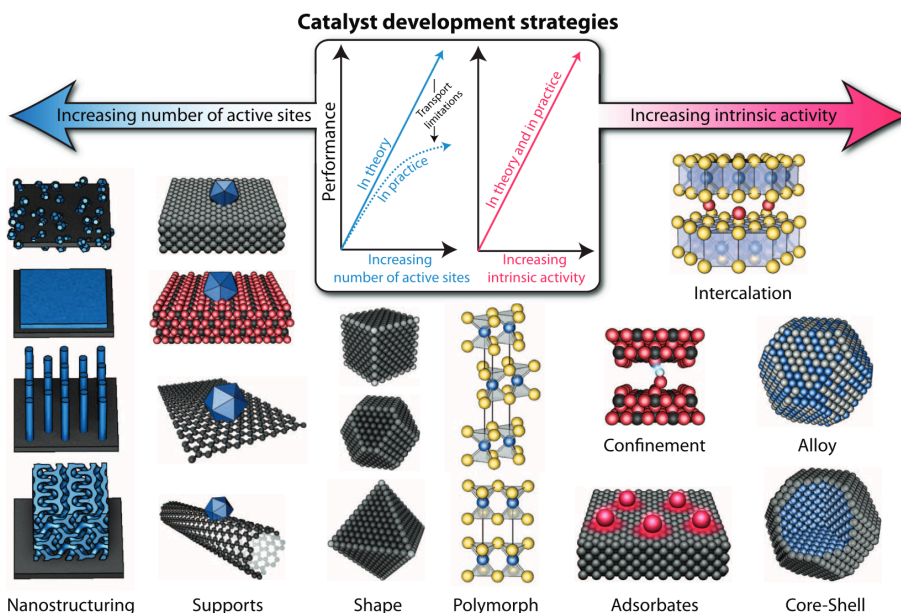


Figure 2.2: Electrocatalyst development strategies to increase the overall activity. Adapted from Ref [5].

2.3 The Local Reaction Environment around the Catalyst in a Gas-Diffusion Electrode System

To reach the maximized utilization of highly active catalysts, the emergence of gas-diffusion systems, e.g. gas-diffusion electrode, provides possibilities to conduct CO_2RR beyond the limiting current density constrained by $\text{CO}_2(\text{aq})$ solubility. The GDE's share the same fundamental knowledge learned from conventional H-type cells, but use an architecture that decreases some limitations, while introducing new ones. For example in GDE architectures and at higher current densities factors such as gas diffusion, aqueous products diffusion, drastic local ionic circumstances, gas-electrolyte-catalyst interfaces, surface wettability, impact the local reaction environment.

Local CO_2 concentration

In GDE-cells, the CO_2 reactant diffuses from the gas channel and through the gas-diffusion layer (GDL) in the gaseous phase before dissolving into a liquid

electrolyte and the immersed catalyst layer (shown in Figure 2.3). As a consequence, mass transport of CO_2 from the gas channel to the catalyst layer is significantly affected by the structure and composition of each layer inside the GDE, as well as diffusion through the aqueous electrolyte and the catalyst layer. This subsection briefly discusses how the local concentration of CO_2 near the catalyst's surface impact on CO_2RR performance.

The main importance of maintaining a high concentration of CO_2 in the local reaction environment is to avoid competing reactions, namely the hydrogen evolution reaction (HER). On many of the catalyst's utilized today, CO_2RR is a favorable reaction vs HER but this changes at elevated overpotentials or if a portion of the catalyst layer is devoid of CO_2 . As widely seen in H-type cell experiments, the selectivity to CO_2RR decreases in the more negative potential region, due to the higher rate of CO_2 consumption compared to that of replenishment via diffusion.^[17]

As CO_2 only approaches the catalyst layer from one direction, the local CO_2 concentration will also vary along the thickness of the catalyst layer as it is being converted into products, and reacting with aqueous species such as hydroxide. A thicker catalyst layer may then not have access to CO_2 at elevated current densities. Such a conclusion then provides a caveat on the maximization of catalyst surface area through structuring as mentioned in the section above. Although the local $[\text{CO}_2]$ is lowered with increasing thickness of catalyst layer (shown in Figure 2.3), impeding the maximum CO_2RR activity, a thicker layer may help to maintain a high local product concentration. In one case the local concentration of CO was found to benefit from a thicker catalyst layer, which can promote the formation of multi-carbon products and inhabitation of HER on Cu surfaces.^[18] However, the excessively thick catalyst layer would result in the rise of HER, owing to the fully immersed catalysts that suffer with CO_2 starvation.

On the other hand, as the catalyst layer is reduced, the overall CO_2RR performance is boosted with the suppression of HER, owing to the decreased CO_2 diffusion distance and higher local $[\text{CO}_2]$ (shown in Figure 2.3). However, the high local $[\text{CO}_2]$ can lead to restrained selectivities towards C_{2+}

products on Cu surfaces, due to the competition with CO for binding sites.^[19] By minimizing the thickness of catalyst layer, an abrupt reaction interface can be built up that allows sufficient CO₂ supply to catalyst surface in highly alkaline media achieving high C₂H₄ yield and constrains hydrogen evolution^[20].

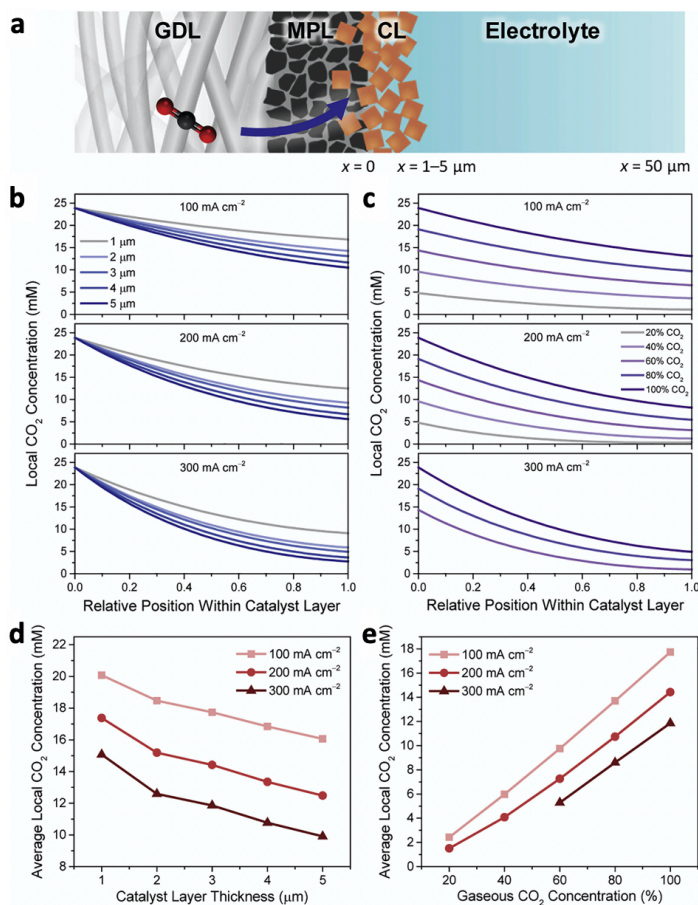


Figure 2.3: (a) Scheme of the boundaries adapted in the proposed model, which includes gas-diffusion layer (GDL), microporous layer (MPL), and catalyst layer (CL). Local CO₂ concentration across the catalyst layer for various (b) catalyst layer thicknesses and (c) gaseous CO₂ concentration at the interface. Adapted from Ref [19].

Products and by-products diffusion

The feasible and adequate CO₂ supply through GDL helps to sustain CO₂ conversion at high reaction rates and maintain a moderate selectivity. However, the mass transport of the generated species over catalyst surface, e.g. CO and OH⁻, can kinetically alter the local reaction environment during electrolysis.

Of critical importance for CO₂RR is the production of hydroxide as a by-product of water-splitting. Water-splitting provides the protons necessary for the reduction reaction, but simultaneously releases hydroxide which then interacts with CO₂. During elevated current densities movement of the locally generated hydroxides is limited to diffusion in the catalyst layer structure, leading to elevated pH. While the high local pH can suppress the HER and even aid CO₂RR, it accelerates the undesired consumption of local CO₂ within non-alkaline electrolyte. A great deal of research is now underway to minimize this effect through the use of either bipolar membranes, or acidic electrolytes.

The diffusion of gaseous products in the catalyst layer is influenced by GDL's physical properties in the same way as CO₂. The high production rate would give rise to the accumulation of CO in the catalyst layer, thus inhibiting the HER via the competition in active sites.^[18] High C₂₊ production efficiency and rate can be achieved on the tandem electrode with designed catalyst layers, by utilizing the back-diffused CO for sequential reduction.^[21] The integrated design of flow channel pattern and catalyst layer structure provides more possibilities to rationally create an optimal local environment for selective multi-carbon production.

Ions over catalyst surfaces

The complex interactions between catalyst surfaces, intermediates and electrolyte ions have a significant impact on tuning the activity and selectivity of CO₂RR. A number of hypothesis and experimental studies have been performed to clarify the effects of ions over catalyst surfaces. Meanwhile,

various strategies are developed to alter the local ionic environment and further selectively regulate the reactions during electrolysis.

In early work an effect of cation hydrolysis was shown to enhance the buffering near the electrode surface, resulting in elevated local pH with the increasing cation size.^[22] In the vicinity of catalyst, solvated cations have also been suggested to potentially interact with absorbed intermediates via a local electric field effect.^[23-26] The crucial role of metal ions in the activation of CO₂RR has been revealed in the mechanism study varying the presence of cations.^[27] Apart from the buffer ability, the anion effect can be attributed to the variation in electronic structure^[28], suppression of proton adsorption^[29] or reconstruction of catalyst morphology^[30].

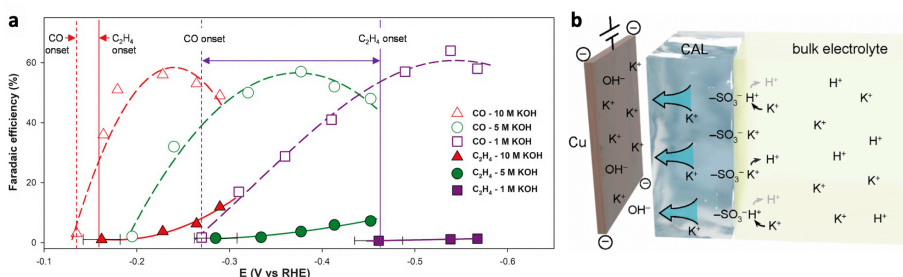


Figure 2.4: (a) Faradaic efficiencies of C₂H₄ and CO indicating the lowered of C-C coupling onset potential with increasing KOH concentrations. Adapted from Ref [20]. (b) Scheme of local ionic environment on the electrode modified with cation-augmenting layer in acidic electrolyte. Adapted from Ref [31].

Owing to the minimized CO₂ diffusion distance to the catalyst surface in GDE system, the CO₂ reduction can be operated in highly alkaline electrolyte, thus the CO₂ reduction and C–C coupling activation energy barriers significantly lowered with high [OH⁻] (shown in Figure 2.4a).^[20] While, in strong acidic media, the sustained high local K⁺ concentration at the catalyst surface has been suggested to be the key of accelerated CO₂ activation and suppressed HER on the electrode modified with a cation-augmenting layer (CAL), as illustrated in Figure 2.4b.^[31] On the other hand, during the cathodic electrolysis operated with cation exchange membrane (CEM), the heavily accumulated cations near catalysts results in the salt formation at the

electrolyte-MPL interface, leading to the GDE failure. (seen the discussion in the following section).

Water in the micro-porous layer

In the approaches towards high current density electrolysis, water is widely used as the solvent owing to its large capacity of soluble salts, thus minimizing the energy loss in electrolyte. During electrochemical reduction of CO₂, the aqueous electrolyte takes essential ions to catalyst surfaces and donates protons via splitting.^[27] On the other hand, water as the key component of electrolyte-MPL interface, its fluidity could physically govern the shifting of this crucial interface, thus significantly altering the local surroundings of catalysts, further impacting the selectivities towards CO₂RR. This sub-section focuses on the influences derived from the wettability of micro-porous layer over the water intrusion.

Within a micro-porous layer, the ideal gas-liquid interface can be constructed with an appropriate water intrusion, then the micropores inside deposited catalyst layer are partially coated with thin films of electrolyte. The well-established interface enables adequate supply of CO₂ from the gas phase across MPL and minimizing the diffusion distance of CO₂ (aq) to catalyst surfaces. However, when surplus water enters the GDE, gas-electrolyte interfaces at these gas-supply pores are pushed away from catalyst surface, thus resulting in the shortage of CO₂ on fully immersed catalyst due to the hindered replenishment through thick electrolyte then leading to the rise of HER and/or CH₄ formation (as illustrated in Figure 2.5a).

The water intrusion follows the hydrophilicity of layers assembled in GDL. The wettability of gas-diffusion electrode is impacted by several factors, such as the wetting properties of utilized materials, applied potentials, reaction time, electrode potential, as well as the architecture and physical properties of each layer including the pore size, porosity, fabrication, etc (as illustrated in Figure 2.5b-c).^[32, 33]

Owing to the excellent hydrophobicity of polytetrafluoroethylene (PTFE), it is widely used as the water proof layer of GDE, holding the electrolyte with

minimal seepage or leakage while maintaining the gas permeability. The water proof layer plays an essential role to establish a steady gas-liquid interface, which ensures the reproducibility and reliability of observed CO₂RR performance. Through a rational incorporation with catalysts, the nature of hydrophobicity and gas-philicity enables PTFE to tune the micro-reaction environment through the local confinement of reactive species, boosting the reduction of CO₂.^[33, 34]

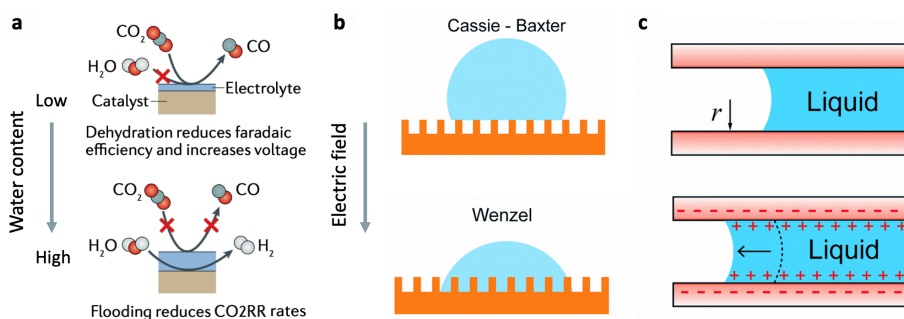


Figure 2.5: (a) The schematic shows undesired circumstances with improper local water content. Adapted from Ref [35]. (b) the transition from Cassies-Baxter to Wenzel wetting states under electric field. (c) Scheme of water intrusion in the micropore. Adapted from Ref [32].

Additives in catalyst layer upon deposition

Polymer binders are widely used to immobilize free-standing catalysts onto the supporting materials (e.g. gas diffusion layers), impacting both the local reaction environment by restricting certain species, as well as the wettability of the catalyst layer.

The water-repellent and gas-philic properties of hydrophobic additives allows CO₂ to be delivered to the catalyst surfaces located away from MPL's gas-liquid interface, thus enlarging the active area for CO₂RR (as illustrated in Figure 2.6a-b). With enhanced hydrophobicity of Cu incorporated with Nafion or fluorinated ethylene propylene (FEP), the CO₂ supply to catalyst surfaces at high reaction rates is effective enough to maintain a high local

concentration of reactive gases, boosting the selectivity towards C_{2+} and strongly suppressing HER as CO_2RR is more favored.^[36]

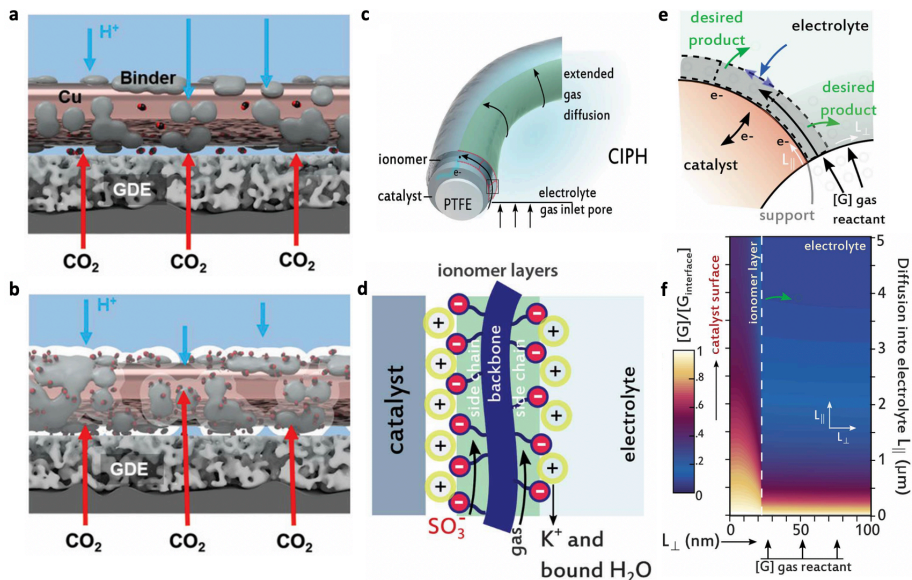


Figure 2.6: Schematic illustrations of the CO_2 accessibilities on the Cu surface with (a) hydrophilic and (b) hydrophobic polymer binders in a gas-diffusion layer. Adapted from Ref [36]. Schematic of (c) metal catalyst deposited onto a PTFE hydrophobic support, coated with ionomer, (d) Nafion endowed with bi-functionality derived from hydrophobic domains ($-CF_2$) and hydrophilic domains ($-SO_3^-$), and (e) the local reaction interface incorporated with Nafion. (f) Modeled gaseous reactant availability along the catalyst surface coated Nafion. L_{\parallel} and L_{\perp} represents the distance parallel and perpendicular to catalyst surface, respectively. Adapted from Ref [37].

In addition to its hydrophobic nature, Nafion also contains hydrophilic groups, endowing it with bi-functionality. As the deposited copper on PTFE-support is sprayed with Nafion solution prepared in polar solvents, the bi-functionality of polymer binders allows the facilitated gas transport over the coating surface shielded by hydrophobic domains and the adequate water uptake and ion transport through the hydrophilic blocks along the catalyst surface, thus potentially extending the transport from tens of nanometers to the micrometer scale (as shown in Figure 2.5c-f). The CO_2RR reaction

kinetics can be significantly improved through the decoupled transportation of gases, ions and electrons^[37].

2.4 Operating Conditions of GDE Experiments

Despite the species over the catalyst surface, the local reaction environment is also strongly affected by operating conditions of CO₂RR. In the electrolytic systems, the applied potential, current density and gas/liquid flowrate can thermodynamically or kinetically impact the reactions and tune the environment inside GDL. With attention to the cumulative variation in the local surroundings during long-term operations, the possible scenarios that break down the system stability resulting in the drastically degraded CO₂RR performance are put under discussion as well.

Applied potentials and current densities

Chronoamperometry is extensively adopted for the mechanistic study of CO₂RR in the past decades. The applied potential on electrode can directly determine the CO₂RR pathway, according to the activation energy of the intermediates or products. Depending on the total ohmic resistance of the whole electrolysis system, the applied potential indirectly influences the reaction rate. On the other hand, the applied potential could hinder the CO₂RR by causing the catalyst failure, such as metal dissolution^[38, 39], alloy segregation^[40]. In GDE systems, the applied potentials can also change the selectivity due to the electro-wetting effects (as mentioned above). These potential-driven effects can improve the wettability of the gas-diffusion layer, resulting the “flooding” of gas-channels in the porous layers, thus blocking the transfer of CO₂ to the catalyst layer^[32].

For the research aiming at commercial industrial conditions, the operating current densities are usually higher than 200 mA/cm². The bulk electrolyte resistance is minimized with high concentration ions (> 1 M), and the correspondingly applied voltages are still high enough to meet the energy requirement for possible products. Furthermore, it is hard to determine the exact potential on the electrode due to the significantly elevated local pH

surrounding catalysts. However, the amount of locally generated OH^- is almost proportionally associated with current densities based on the selectivities. Therefore, the current-control experimental techniques are feasible to establish a local reaction environment with controlled overall reaction rates.

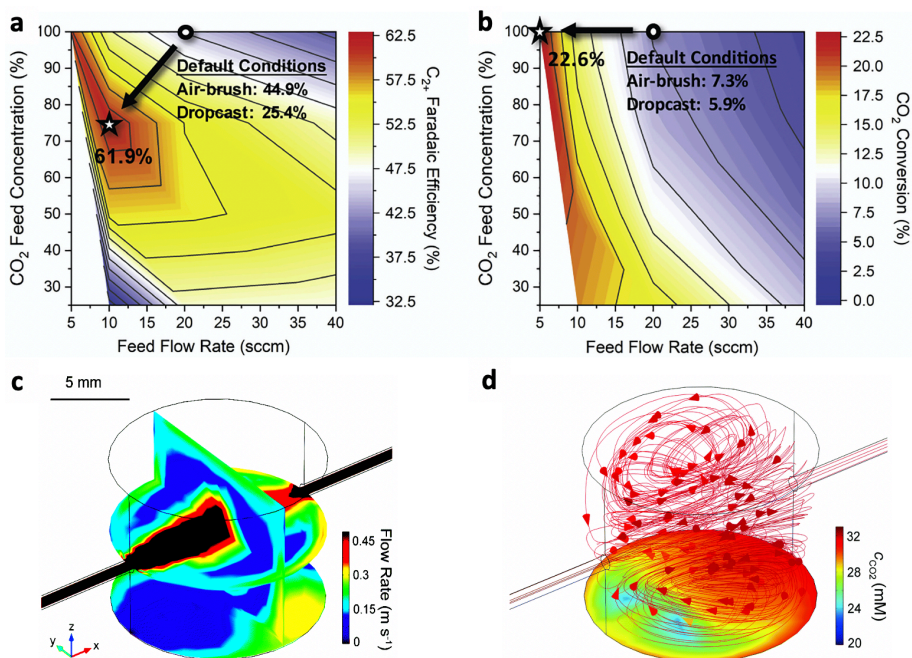


Figure 2.7: Colored contour map of (a) selectivity for C₂⁺ products and (b) single-pass conversion under various CO₂ feed flowrates and concentrations on Cu loaded GDE's. Adapted from Ref [19]. (c) simulated catholyte flow field and (d) corresponding CO₂ concentration distribution with pumping 0.1 M CO₂-saturated KHCO₃ at the rate of 128 mL/min. Adapted from Ref [41].

Flowrates of feed-gas and electrolyte

The delicate pressure balance at gas-liquid interface plays a vital role to sustain an optimal local environment and long reactor lifetime. Furthermore, the flowrates of feed-gas and electrolyte directly regulate the mass transport of local species in gaseous and liquid phases, e.g. CO and hydroxides, thereby attaining desired performance of CO₂RR. With rational control of operating conditions, the single-pass conversion can be effectively enhanced by

lowering the CO₂ flow rate while improving the C₂₊ selectivity on Cu surfaces.^[19] (indicated in Figure 2.7) On the other hand, depending on the chamber shape, flow pattern and feed flowrate, the varied local flowrates and nonuniform CO₂ concentrations over electrode surfaces pose challenges to the detailed investigations for mechanism studies.^[41] (as shown in Figure 2.7)

GDE failure modes

There are three common failure scenarios for GDE-based CO₂ electrolytic cells: catalyst deactivation, cathode flooding and (bi)carbonate salt blockage (Figure 2.8). These failures could either obviously interrupt the experiment or unnoticeably disturb the analysis. The CO₂RR operating tests without ruling out GDE failure may result in inappropriate interpretation of experimental data or misleading explanation of the mechanism.

Catalyst failure: The variation in the active sites causes the failure of catalysts, leading to the evidently lower CO₂ reduction rate or selectivity. The surface reconstruction and metal dissolution/leaching are the main failure mechanisms of metallic catalysts.^[38] For multi-metal catalysts, such as alloyed or nanostructured Cu-Ag, the segregation introduced by applied potentials or surface absorbed intermediates could notably tune the activity and selectivity.^[40] In addition to the change in intrinsic activity, the active sites may be poisoned by un-desorbed intermediates, reducing the amount of available active sites for CO₂RR, thus resulting in a decreased activity or lowered selectivity for multi-electron products.

The transition metal impurities play a vital role in the deactivation of CO₂RR even at ppm levels. However, except the deactivation scenarios also potentially occurring in H-cells, the catalysts loaded on GDE's could hold a better impurity resistance owing to the opposite direction of CO₂ transport. Within a GDL system, impurities are likely to deposit onto the catalyst surfaces furthest from the optimum micro-environment for CO₂RR.

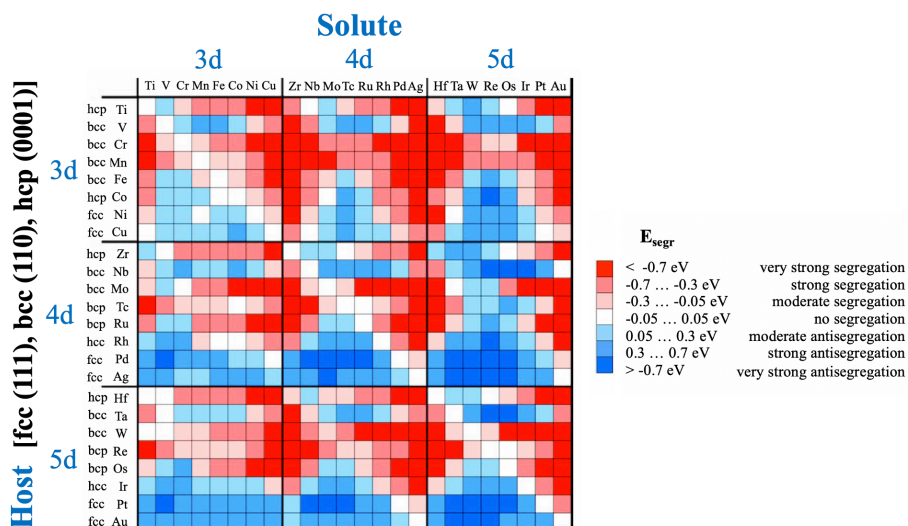


Figure 2.8: Surface segregation energies of transition-metal impurities (solute) for the closed-packed surfaces of transition metal hosts. Adapted from Ref [40].

Cathode flooding: Severe flooding resulted from pressure imbalance could give rise to the disruption of experiments, which can be regulated by manipulating the CO₂ or electrolyte flow rate.^[42] In addition to the visible water penetration through GDL, the flooding occurring inside porous layers could unnoticeably inhibit CO₂RR due to the suppression of CO₂ transport.

The water intrusion within micro-channels could spread widely with increased electrolyte concentrations and applied voltages, occupying more space of GDL' pores and driving the liquid-MPL interface shift towards gas phase, thus hampering the feed of CO₂.^[43] During cathodic CO₂ reduction, the local alkaline environment also gradually impairs the water resistance surface, resulting in the loss of hydrophobic nature. The application of less-basic electrolytes and additional hydrophobic layers/additives are practical means to alleviate the decreasing hydrophobicity.

Carbonate salt formation: For CO₂RR operated in GDE systems, carbonate salts are continuously generated and precipitated at the cathode through the, owing to the high local ion concentrations arose from the reaction of CO₂ with OH⁻ ions inside the confined pores, notwithstanding the moderate solubility of alkali (bi)carbonates in aqueous media. The locally formed solids cause

blockage in gas channels, hindering gaseous products/ CO_2 transport, thus decreasing CO_2RR activity. These hygroscopic solids also could lower the water resistance, resulting in electrolyte intrusion.^[43] The locally formed carbonates can be removed with water flushed through the gas diffusion layer. With the rational cell design and use of pure water as electrolyte, the salts precipitation can be completely eliminated.^[44]

In this chapter, with the focus on variations in catalysts and local reaction environments during CO_2 electrolysis on gas-diffusion electrodes, the key influential factors, such as CO_2 transport, products diffusion, electrolytic ions, local water content, ionomers, operating conditions, are outlined as they can effectively regulate the local circumstances in various aspects. While developing novel catalysts with distinguished activity for CO_2 reduction, the system-level design strategy integrated with the construction of prompting local circumstances presents the opportunity to achieve upgraded CO_2RR performance in gas-fed electrolyzers.

References

- (1) Birdja, Y.Y., Pérez-Gallent, E., Figueiredo, M.C., Göttle, A.J., Calle-Vallejo, F., and Koper, M.T.M., Advances and challenges in understanding the electrocatalytic conversion of carbon dioxide to fuels. *Nat. Energy* **2019**, 4(9): p. 732-745.
- (2) Kuhl, K.P., Hatsukade, T., Cave, E.R., Abram, D.N., Kibsgaard, J., and Jaramillo, T.F., Electrocatalytic Conversion of Carbon Dioxide to Methane and Methanol on Transition Metal Surfaces. *J. Am. Chem. Soc.* **2014**, 136(40): p. 14107-14113.
- (3) Feaster, J.T., Shi, C., Cave, E.R., Hatsukade, T., Abram, D.N., Kuhl, K.P., Hahn, C., Nørskov, J.K., and Jaramillo, T.F., Understanding Selectivity for the Electrochemical Reduction of Carbon Dioxide to Formic Acid and Carbon Monoxide on Metal Electrodes. *ACS Catal.* **2017**, 7(7): p. 4822-4827.
- (4) Sun, K., Cheng, T., Wu, L., Hu, Y., Zhou, J., Maclellan, A., Jiang, Z., Gao, Y., Goddard, W.A., and Wang, Z., Ultrahigh Mass Activity for Carbon Dioxide Reduction Enabled by Gold–Iron Core–Shell Nanoparticles. *J. Am. Chem. Soc.* **2017**, 139(44): p. 15608-15611.
- (5) Seh, Z.W., Kibsgaard, J., Dickens, C.F., Chorkendorff, I., Nørskov, J.K., and Jaramillo, T.F., Combining theory and experiment in electrocatalysis: Insights into materials design. *Science* **2017**, 355(6321).
- (6) Lysgaard, S., Mýrdal, J.S.G., Hansen, H.A., and Vegge, T., A DFT-based genetic algorithm search for AuCu nanoalloy electrocatalysts for CO₂ reduction. *Phys. Chem. Chem. Phys.* **2015**, 17(42): p. 28270-28276.
- (7) Reske, R., Mistry, H., Behafarid, F., Roldan Cuenya, B., and Strasser, P., Particle Size Effects in the Catalytic Electroreduction of CO₂ on Cu Nanoparticles. *J. Am. Chem. Soc.* **2014**, 136(19): p. 6978-6986.
- (8) Kim, D., Xie, C., Becknell, N., Yu, Y., Karamad, M., Chan, K., Crumlin, E.J., Nørskov, J.K., and Yang, P., Electrochemical Activation of CO₂ through Atomic Ordering Transformations of AuCu Nanoparticles. *J. Am. Chem. Soc.* **2017**, 139(24): p. 8329-8336.
- (9) Jovanov, Z.P., Hansen, H.A., Varela, A.S., Malacrida, P., Peterson, A.A., Nørskov, J.K., Stephens, I.E.L., and Chorkendorff, I., Opportunities and

- challenges in the electrocatalysis of CO₂ and CO reduction using bifunctional surfaces: A theoretical and experimental study of Au–Cd alloys. *J. Catal.* **2016**, 343: p. 215-231.
- (10) Peterson, A.A. and Nørskov, J.K., Activity Descriptors for CO₂ Electroreduction to Methane on Transition-Metal Catalysts. *J. Phys. Chem. Lett.* **2012**, 3(2): p. 251-258.
- (11) Kim, C., Möller, T.F., Schmidt, J., Thomas, A., and Strasser, P., Suppression of Competing Reaction Channels by Pb Adatom Decoration of Catalytically Active Cu Surfaces During CO₂ Electroreduction. *ACS Catal.* **2018**.
- (12) Feng, X., Jiang, K., Fan, S., and Kanan, M.W., Grain-Boundary-Dependent CO₂ Electroreduction Activity. *J. Am. Chem. Soc.* **2015**, 137(14): p. 4606-4609.
- (13) Mariano, R.G., McKelvey, K., White, H.S., and Kanan, M.W., Selective Increase in CO₂ Electroreduction Activity at Grain-Boundary Surface Terminations. *Science* **2017**, 358(6367): p. 1187-1192.
- (14) Clark, E.L., Hahn, C., Jaramillo, T.F., and Bell, A.T., Electrochemical CO₂ Reduction over Compressively Strained CuAg Surface Alloys with Enhanced Multi-Carbon Oxygenate Selectivity. *J. Am. Chem. Soc.* **2017**, 139(44): p. 15848-15857.
- (15) Jansonius, R.P., Reid, L.M., Virca, C.N., and Berlinguette, C.P., Strain Engineering Electrocatalysts for Selective CO₂ Reduction. *ACS Energy Lett.* **2019**: p. 980-986.
- (16) Benck, J.D., Hellstern, T.R., Kibsgaard, J., Chakthranont, P., and Jaramillo, T.F., Catalyzing the Hydrogen Evolution Reaction (HER) with Molybdenum Sulfide Nanomaterials. *ACS Catal.* **2014**, 4(11): p. 3957-3971.
- (17) Xu, J., Li, X., Liu, W., Sun, Y., Ju, Z., Yao, T., Wang, C., Ju, H., Zhu, J., Wei, S., and Xie, Y., Carbon Dioxide Electroreduction into Syngas Boosted by a Partially Delocalized Charge in Molybdenum Sulfide Selenide Alloy Monolayers. *Angew. Chem. Int. Ed.* **2017**, 56(31): p. 9121-9125.
- (18) Marcel, S., Youngmin, Y., N, J.M., and Yogesh, S., Competition between H and CO for Active Sites Governs Cu Mediated Electrosynthesis of Hydrocarbon Fuels. *Angew. Chem. Int. Ed.* **2018**, 57(32): p. 10221-10225.

- (19) Tan, Y.C., Lee, K.B., Song, H., and Oh, J., Modulating Local CO₂ Concentration as a General Strategy for Enhancing C–C Coupling in CO₂ Electroreduction. *Joule* **2020**, 4(5): p. 1104-1120.
- (20) Dinh, C.-T., Burdyny, T., Kibria, M.G., Seifitokaldani, A., Gabardo, C.M., García de Arquer, F.P., Kiani, A., Edwards, J.P., De Luna, P., Bushuyev, O.S., Zou, C., Quintero-Bermudez, R., Pang, Y., Sinton, D., and Sargent, E.H., CO₂ Electroreduction to Ethylene via Hydroxide-Mediated Copper Catalysis at an Abrupt Interface. *Science* **2018**, 360(6390): p. 783-787.
- (21) She, X., Zhang, T., Li, Z., Li, H., Xu, H., and Wu, J., Tandem Electrodes for Carbon Dioxide Reduction into C₂⁺ Products at Simultaneously High Production Efficiency and Rate. *Cell Reports Physical Science* **2020**, 1(4): p. 100051.
- (22) Singh, M.R., Kwon, Y., Lum, Y., Ager, J.W., and Bell, A.T., Hydrolysis of Electrolyte Cations Enhances the Electrochemical Reduction of CO₂ over Ag and Cu. *J. Am. Chem. Soc.* **2016**, 138(39): p. 13006-13012.
- (23) Pérez-Gallent, E., Marcandalli, G., Figueiredo, M.C., Calle-Vallejo, F., and Koper, M.T.M., Structure- and Potential-Dependent Cation Effects on CO Reduction at Copper Single-Crystal Electrodes. *J. Am. Chem. Soc.* **2017**, 139(45): p. 16412-16419.
- (24) Chen, L.D., Urushihara, M., Chan, K., and Nørskov, J.K., Electric Field Effects in Electrochemical CO₂ Reduction. *ACS Catal.* **2016**, 6(10): p. 7133-7139.
- (25) Ringe, S., Clark, E.L., Resasco, J., Walton, A., Seger, B., Bell, A.T., and Chan, K., Understanding cation effects in electrochemical CO₂ reduction. *Energy Environ. Sci.* **2019**, 12(10): p. 3001-3014.
- (26) Resasco, J., Chen, L.D., Clark, E., Tsai, C., Hahn, C., Jaramillo, T.F., Chan, K., and Bell, A.T., Promoter Effects of Alkali Metal Cations on the Electrochemical Reduction of Carbon Dioxide. *J. Am. Chem. Soc.* **2017**, 139(32): p. 11277-11287.
- (27) Monteiro, M.C.O., Dattila, F., Hagedoorn, B., García-Muelas, R., López, N., and Koper, M.T.M., Absence of CO₂ electroreduction on copper, gold and silver electrodes without metal cations in solution. *Nat. Catal.* **2021**, 4(8): p. 654-662.

- (28) Varela, A.S., Ju, W., Reier, T., and Strasser, P., Tuning the Catalytic Activity and Selectivity of Cu for CO₂ Electroreduction in the Presence of Halides. *ACS Catal.* **2016**, 6(4): p. 2136-2144.
- (29) Ogura, K., Ferrell, J.R., Cugini, A.V., Smotkin, E.S., and Salazar-Villalpando, M.D., CO₂ attraction by specifically adsorbed anions and subsequent accelerated electrochemical reduction. *Electrochim. Acta* **2010**, 56(1): p. 381-386.
- (30) Gao, D., Scholten, F., and Roldan Cuenya, B., Improved CO₂ Electroreduction Performance on Plasma-Activated Cu Catalysts via Electrolyte Design: Halide Effect. *ACS Catal.* **2017**, 7(8): p. 5112-5120.
- (31) Huang, J.E., Li, F., Ozden, A., Rasouli, A.S., Arquer, F.P.G.d., Liu, S., Zhang, S., Luo, M., Wang, X., Lum, Y., Xu, Y., Bertens, K., Miao, R.K., Dinh, C.-T., Sinton, D., and Sargent, E.H., CO₂ electrolysis to multicarbon products in strong acid. *Science* **2021**, 372(6546): p. 1074-1078.
- (32) Li, M., Idros, M.N., Wu, Y., Burdyny, T., Garg, S., Zhao, X.S., Wang, G., and Rufford, T.E., The role of electrode wettability in electrochemical reduction of carbon dioxide. *J. Mater. Chem. A* **2021**, 9(35): p. 19369-19409.
- (33) Xing, Z., Hu, L., Ripatti, D.S., Hu, X., and Feng, X., Enhancing carbon dioxide gas-diffusion electrolysis by creating a hydrophobic catalyst microenvironment. *Nat. Commun.* **2021**, 12(1): p. 136.
- (34) Xing, Z., Hu, X., and Feng, X., Tuning the Microenvironment in Gas-Diffusion Electrodes Enables High-Rate CO₂ Electrolysis to Formate. *ACS Energy Lett.* **2021**, 6(5): p. 1694-1702.
- (35) Lees, E.W., Mowbray, B.A.W., Parlane, F.G.L., and Berlinguette, C.P., Gas diffusion electrodes and membranes for CO₂ reduction electrolyzers. *Nat Rev Mater* **2022**, 7(1): p. 55-64.
- (36) Pham, T.H.M., Zhang, J., Li, M., Shen, T.H., Ko, Y., Tileli, V., Luo, W., and Züttel, A., Enhanced Electrocatalytic CO₂ Reduction to C₂⁺ Products by Adjusting the Local Reaction Environment with Polymer Binders. *Advanced Energy Materials* **2022**, 12(9): p. 2103663.
- (37) García de Arquer, F.P., Dinh, C.-T., Ozden, A., Wicks, J., McCallum, C., Kirmani, A.R., Nam, D.-H., Gabardo, C., Seifitokaldani, A., Wang, X., Li, Y.C., Li, F., Edwards, J., Richter, L.J., Thorpe, S.J., Sinton, D., and Sargent,

- E.H., CO₂ electrolysis to multicarbon products at activities greater than 1 A cm⁻². *Science* **2020**, 367(6478): p. 661-666.
- (38) Vavra, J., Shen, T.H., Stoian, D., Tileli, V., and Buonsanti, R., Real-time monitoring reveals dissolution/redeposition mechanism in copper nanocatalysts during the initial stages of the CO₂ reduction reaction. *Angew. Chem. Int. Ed.* **2021**.
- (39) Rossi, K. and Buonsanti, R., Shaping Copper Nanocatalysts to Steer Selectivity in the Electrochemical CO₂ Reduction Reaction. *Acc. Chem. Res.* **2022**, 55(5): p. 629-637.
- (40) Ruban, A.V., Skriver, H.L., and Nørskov, J.K., Surface segregation energies in transition-metal alloys. *Phys. Rev. B* **1999**, 59(24): p. 15990-16000.
- (41) Ye, K., Zhang, G., Ma, X.-Y., Deng, C., Huang, X., Yuan, C., Meng, G., Cai, W.-B., and Jiang, K., Resolving local reaction environment toward an optimized CO₂-to-CO conversion performance. *Energy Environ. Sci.* **2022**, 15(2): p. 749-759.
- (42) Verma, S., Hamasaki, Y., Kim, C., Huang, W., Lu, S., Jhong, H.-R.M., Gewirth, A.A., Fujigaya, T., Nakashima, N., and Kenis, P.J.A., Insights into the Low Overpotential Electroreduction of CO₂ to CO on a Supported Gold Catalyst in an Alkaline Flow Electrolyzer. *ACS Energy Lett.* **2018**, 3(1): p. 193-198.
- (43) Leonard, M.E., Clarke, L.E., Forner-Cuenca, A., Brown, S.M., and Brushett, F.R., Investigating electrode flooding in a flowing electrolyte, gas-fed carbon dioxide electrolyzer. *ChemSusChem* **2020**, 13(2): p. 400-411.
- (44) Xu, Y., Edwards, J.P., Liu, S., Miao, R.K., Huang, J.E., Gabardo, C.M., O'Brien, C.P., Li, J., Sargent, E.H., and Sinton, D., Self-Cleaning CO₂ Reduction Systems: Unsteady Electrochemical Forcing Enables Stability. *ACS Energy Lett.* **2021**, 6(2): p. 809-815.

Electronic Effects Determine the Selectivity of Planar Au-Cu Bimetallic Thin Films for Electrochemical CO₂ Reduction

3

Au-Cu bimetallic thin films with controlled composition were fabricated by magnetron sputtering co-deposition, and their performance for the electrocatalytic reduction of CO₂ was investigated. The uniform planar morphology served as a platform to evaluate the electronic effect isolated from morphological effects while minimizing geometric contributions. The catalytic selectivity and activity of Au-Cu alloys was found to be correlated with the variation of electronic structure that was varied with tunable composition. Notably, the *d*-band center gradually shifted away from the Fermi level with increasing the Au atomic ratio, leading to a weakened binding energy of *CO, which is consistent with low CO coverage observed in CO stripping experiments. The decrease of the *CO binding strength results in the enhanced catalytic activity for CO formation with the increase of Au content. In addition, it was observed that copper oxide/hydroxide species are less stable on Au-Cu surfaces compared to those on pure Cu surface, where the surface oxophilicity could be critical to tuning the binding strength of *OCHO. These results imply that the altered electronic structure could explain the decreased formation of HCOO[−] on the Au-Cu alloys. In general, the formation of CO and HCOO[−] as main CO₂ reduction products on planar Au-Cu alloys followed the shift of *d*-band center, which indicates the electronic effect is the major governing factor for the electrocatalytic activity of CO₂ reduction on Au-Cu bimetallic thin films.

The contents of this chapter have been published in:

Kai Liu, Ming Ma, Longfei Wu, Marco Valenti, Drialy Cardenas-Morcoso, Jan P. Hofmann, Juan Bisquert, Sixto Gimenez, and Wilson A. Smith. *ACS Applied Materials & Interfaces* **2019**, 11 (18), 16546-16555.

3.1 Introduction

The electrocatalytic reduction of CO₂ is a promising way to sustainably convert CO₂ into high-value added products, chemicals and fuels. A large amount of materials have been examined theoretically and experimentally as electrocatalysts for the CO₂ reduction reaction (CO₂RR) under various conditions.^[1-8] These studies show that the CO₂ reduction activity and selectivity of transition-metal catalysts is fundamentally limited by linear scaling relations between reaction intermediates.^[9] Among a wide variety of well-studied metallic catalysts for CO₂RR, Au and Cu are very attractive, as Au has shown the highest activity for the selective production of CO^[5], and Cu has the largest range of product selectivities with the ability to form up to 16 different products.^[10] While the activity of these transition metals has improved steadily in the past few years due to the increased global research efforts, their optimal performance is still hindered by the scaling relationship.^[11] Recently, it has been proposed that alloying two metals (or making bimetallic electrodes) is an efficient approach to promote improved activity and selectivity of the electro-reduction of CO₂ by tuning the binding strength of intermediates with a modified electronic structure.^[5, 6, 12] It has been found that tuning the composition of bimetallic/alloy materials can offer a simple way to effectively change the local electronic structure of the composite materials, which also has beneficial properties to create new binding sites at the interface of the two metals with different binding energies than the linearly extrapolated values of each individual metals.^[13, 14]

Au-Cu bimetallic alloys have been previously investigated for electrochemical CO₂RR and shown remarkable performance.^[14] However, recent works on bimetallic catalysts (including Au-Cu) have focused on nanostructured catalysts, which complicates mechanistic understanding due to the combined effects of both the metal composition/electronic structure, and the surface morphology^[8, 14-16] which affects mass transport of reactants and products near the surface and leads to different surface coverages. As a high turnover rate was observed on Au₃Cu bimetallic nanoparticles, and the enhanced activity for CO formation on Au-Cu bimetallic nanoparticles was

attributed to the synergistic geometric and electronic effects.^[8, 14] From the view of thermodynamics, the electronic effect results from the variation in the electronic structure, which can tune the binding strength of intermediates and even be able to provide new binding sites, e.g. optimizing the bind strength of the $\ast\text{CO}$ and $\ast\text{COOH}$ intermediates.^[13, 17] However, the geometric effect can control the kinetics of a reaction, as the morphology can affect the mass transport which may alter the interfacial reaction conditions.^[18, 19] Based on the published results^[7, 14], there is still a lack of comprehensive understanding of these effects or a potential synergistic effect, as the geometric and electronic effects simultaneously participate in CO_2RR on nanocatalysts, and it is difficult to distinguish the actual role of electronic structure and morphology individually. Therefore, it is important to decouple these phenomena and investigate the relative influences of each effect.

Other Au-based alloys, most notably, Au-Pt^[20] and Au-Pd^[21], have also been explored for CO_2RR . Au is near the peak of the Sabatier volcano plot for CO formation, while Pt and Pd bind very strongly to CO. The catalytic behavior of Au-Pt alloys for CO formation acts as expected from the relationship, and follows a linear scaling relation between $\ast\text{COOH}$ and $\ast\text{CO}$ binding energies. On the other hand, in the volcano plot of HCOO^- , Au, Pt and Pd all show a weak binding energy to $\ast\text{OCHO}$ and are far away from the volcano peak. However, alloys of Au-Pt can produce upwards of 5% Faradaic Efficiency of HCOO^- .^[20] This result is ascribed to the synergistic effect derived from the alloying, where new binding sites apart from Au and Pt can form a favorable pathway to produce HCOO^- . Cu is also on the weak binding side of the volcano plot for the formation of HCOO^- , having an intermediate binding strength of $\ast\text{OCHO}$ and lower $\ast\text{H}$ binding energy than Pt and Pd. However, the formation of HCOO^- on Au-Cu alloys in the kinetic-limited potential region is rarely discussed. A systematic and detailed investigation of the activity and selectivity for HCOO^- formation on Au-Cu alloys will therefore be useful for researchers to obtain a more complete understanding of the electronic effects of these alloys on their product selectivity.

In this work, the Au-Cu bimetallic thin films were fabricated by magnetron sputtering, which offers a flexible way to make compositionally variant thin films that are dense and relatively flat, giving an ideal platform to investigate compositional/electronic effects without having a nanostructured surface which may affect mass transport and local variations of reaction conditions. A systematic experimental investigation was applied to this planar bimetallic platform to quantitatively compare the intrinsic activity of the catalysts as a function of Au and Cu composition. With X-ray diffraction (XRD) and electrochemical impedance spectroscopy (EIS) characterization, it was possible to find a relationship between grain size, charge transfer resistance and microstrain to understand the reactivity of the catalysts. Combining these results with CO stripping measurements, it was found that as the content of Au rises, the desorption energy of $^*\text{CO}$ decreases, and therefore the release of CO becomes more efficient. The weakened oxygen binding strength on Au-Cu alloys is revealed by CV measurements, which leads to the low binding strength of oxygen-bonded $^*\text{OCHO}$ and further reduces the formation of HCOO^- . Given the variety of physical and electronic characteristics studied in these Au-Cu bimetallic films, it seems that the d -band energy is the most important factor that influences the reactivity of the bimetallic films. Insights gained from this well-defined system will help to understand the variation of intermediate binding strength owing to the local electronic effect, and further develop high-performance catalysts with desired selectivity and activity.

3.2 Results and Discussion

3.2.1 Morphological investigation of the Au-Cu bimetallic thin films deposited on Ti substrates

Magnetron sputtering deposition offers a highly reproducible process to fabricate high purity Au-Cu bimetallic films, as the deposition is performed in a vacuum chamber with a controlled Argon pressure. With the co-deposition of Au and Cu, the deposition rates of the two materials can be tuned by adjusting the sputtering powers of Au and Cu targets, thus precisely

controlling the atomic ratio of binary films.^[20] The surface of the films was first investigated by SEM. From the SEM images (seen in Figure S3.1), it is shown that the 80-nm-thick metallic films with different compositions exhibit a relatively uniform surface, suggesting that the as-prepared planar surface is ideal for reducing the impact of local pH effects associated with nano- or mesostructured morphologies, and provides a consistent platform across all the film compositions.^[22]

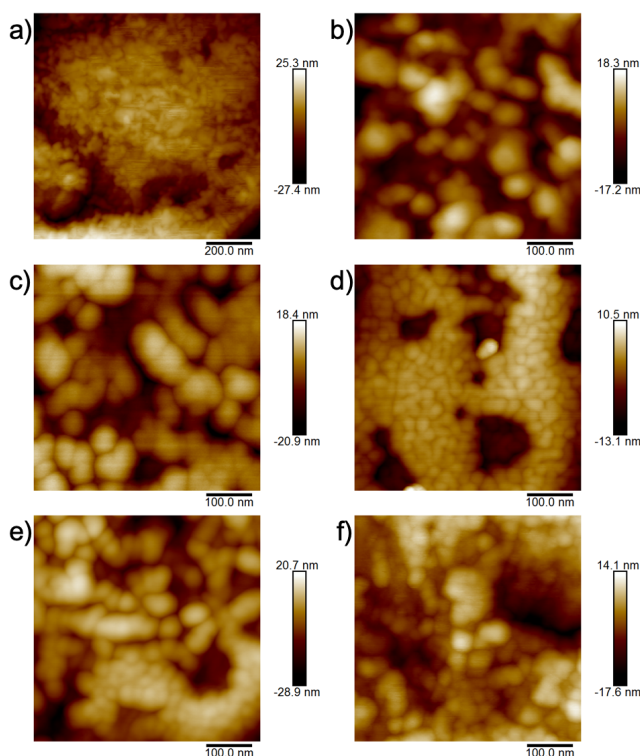


Figure 3.1: AFM images of (a) bare Ti foil and catalyst films after CO₂RR @ -0.7 V vs RHE for 1 h, (b) Au, (c) Au₇₅Cu₂₅, (d) Au₅₀Cu₅₀, (e) Au₂₅Cu₇₅, (f) Cu thin film.

To better understand the local structure of the thin films, AFM was carried out on the films deposited on Ti foils, with the results shown in Figure 3.1. The surface of sputtered thin films have a relatively smooth and uniform morphology, which is typical for sputtered metallic thin films that are expected to be formed through vertical columnar growth.^[23-25] The relative

deposition powers of Au and Cu were adjusted to achieve the desired compositional ratio, while the surface roughness was not significantly varied (as shown in Table S3.1), which demonstrates that the morphology is not affected by the different fabrication conditions. As presented in Figure S3.2, in this work, there is no evident nanostructuring or further roughening of the surface introduced by the deposition, which ensures the CO₂ RR activity would not be influenced by the variation of surface roughness and local mass transport. In addition, the surface was examined after CO₂RR experiments, which shows a similar morphology, indicating that the surface structure remained constant during electrolysis (seen in Figure 3.1). The double layer capacitance (C_{dl}) was measured to evaluate the relative electrochemically active surface area (ECSA) and surface roughness. As shown in Figure S3.3, all the capacitances of the as-prepared samples possess a similar value compared to those of flat Au and Cu foils with a smooth surface, revealing that the as-prepared films exhibit a low surface roughness and have a relative uniform distribution of active sites.^[26]

3.2.2 Structural characterization of the Au-Cu binary catalytic films

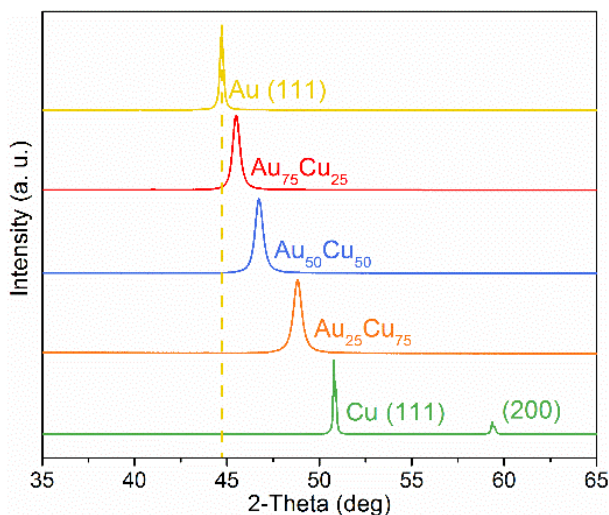


Figure 3.2: XRD patterns of the binary metallic films with varied composition.

In order to obtain an accurate stoichiometric ratio, the molar volume of Au ($10.21 \text{ cm}^3/\text{mol}$) and Cu ($7.124 \text{ cm}^3/\text{mol}$) were taken into consideration while the magnetron sputtering deposition was performed, such that the obtained films could contain a desired composition and have the same thickness. The crystal structure of the as-prepared films was examined by XRD, with the results shown in Figure 3.2. The XRD patterns show that all the sputtered samples have one dominant characteristic, which is assigned to the diffraction of the (111) plane from the face-centered cubic (FCC) crystal structure. As shown in the patterns, the position of the dominant peak gradually shifts from 44° to 50.7° as the stoichiometric ratio of Cu is increased, and no characteristic peak of pure Au or Cu was observed in the co-deposited samples, which demonstrates that Au and Cu are alloyed with each other rather than being randomly physically mixed or phase separated.

The as-deposited thin films were characterized by EDS and XPS to investigate the bulk and surface atomic ratio, with the results shown in Figure 3.3. It can be seen that the surface and bulk composition are in agreement with each other, representing that there is no obvious phase segregation near the surface and the stoichiometric ratio is identical from the bulk to the

surface. Besides the uniform composition, the increase of lattice parameter is linear with the rise of Au content (shown in Figure 3.3), suggesting that the uniform atomic arrangement is stable across the varied compositions and indicating that the formation of Au-Cu alloys is validated by Vegard's law.^[27]

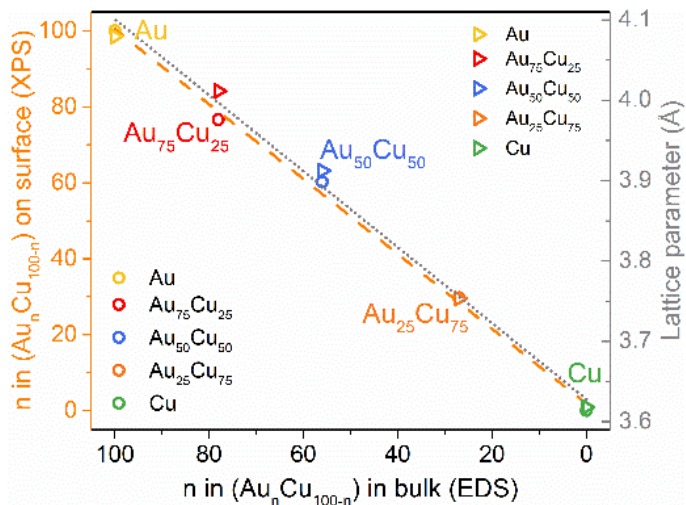


Figure 3.3: Comparison of the surface composition with bulk composition (○) and variation of lattice parameters of the as-prepared samples (▷). The dashed orange line provides a general guide to the trend of data points (slope: 0.9860, $R^2=0.9957$). The dotted black line presents the prediction of Vegard's law based on the lattice parameters of Au and Cu ($R^2= 0.9891$).

To further analyze the effect of crystallite structure, the structural parameters of the binary thin film electrodes were extracted from the XRD data and summarized in Table 3.1. It can be seen that the difference in radius of Au (166 pm) and Cu (140 pm) atoms leads to microstrain in the bimetallic thin films. It has been reported that grain boundaries play a vital role on the activity of CO₂RR, and the grain boundary density increases as the grain size becomes smaller.^[28-30] Therefore it is relevant to investigate the grain size as a function of binary composition. The grain size of the alloy thin films are similar to each other (represented in Table 3.1), and much smaller than the grain size of the pure Au and Cu films. The microstrain in the alloy samples is higher than that in the individual Au and Cu films, which is consistent with

the previous report.^[31] This result is expected since there is more strain with multi-component films than with a single atomic component.

Table 3.1: Structural Metrics of As-Deposited Electrodes

Sample	Grain size (nm)	Microstrain (%)
Au	27.49	0.0039
Au ₇₅ Cu ₂₅	19.00	0.0055
Au ₅₀ Cu ₅₀	17.37	0.0058
Au ₂₅ Cu ₇₅	16.24	0.0060
Cu	33.68	0.0028

In addition to the crystalline and morphological properties of the alloy thin films, the electronic structure can also play an important role in CO₂RR. By varying the electronic structure of transition metals, the interaction between adsorbates and *d*-band electronic structure can be tuned, which can in turn alter the binding strength of intermediates.^[14] The surface valence band XPS measurements were conducted to investigate the energy variation of *d*-orbital electrons. However, the copper can immediately react with oxygen forming a thin oxide layer even with short exposure to air. Additionally, the surface adsorbates could also introduce some electronic state influencing the valence band spectral region and the *d*-band center determination.^[32] Thus, depth profile XPS was conducted to understand the effects of the native oxide and adsorbates on the *d*-band center. As the oxidation layer is very thin and no obvious adsorbate-induced peak was found in the valence band integration region, the *d*-band center seems to not be affected by the thin surface oxide layer (seen in Figure S3.5 and Table S3.2). As presented in Figure 3.4, surface valence bands of Au-Cu bimetallic catalysts exhibit different patterns compared to those of Au or Cu, and the center of the *d*-band gradually shifts away from the Fermi level as the Au content increases. This *d*-band shift can affect the occupancy of anti-bonding states, which in turn suggests that the binding strength for intermediates is weakened.^[14, 33] XPS measurements were performed before and after electrolysis, showing the same overall trend of the *d*-orbital electron, and no new features or phase segregations occurred after performing CO₂ reduction (seen in Figure S3.7 and S3.8).

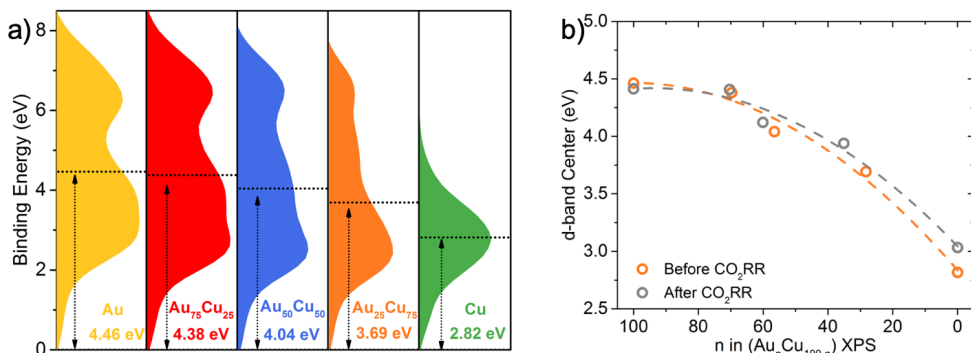


Figure 3.4: Surface valence band X-ray photoemission spectra of the as-prepared Au, Cu and alloys. (a) as-prepared samples before CO₂RR and (b) the *d*-band center of these samples before and after CO₂RR @ -0.7 V *vs* RHE for 1 h. The gravity center of the valence band center is shown by the dotted lines compared to 0 eV. The binding energy is the value of $|E - E_{\text{Fermi}}|$.

3.2.3 Electrochemical properties of the as-prepared thin films

The Au-Cu bimetallic catalysts were characterized by cyclic voltammetry (CV) in an alkaline solution to investigate the electrochemical properties of Cu, Au and alloys of the two metals. The sputtered Au thin film exhibited similar reduction features (shown in Figure 3.5a) as reported previously.^[34] The oxidation and reduction peaks of Cu are clearly shown in Figure 3.5e. In the oxidation region of Cu, Peak 1 indicates the formation of Cu₂O.^[35] As the potential increased positively, the Cu-containing film subsequently starts to form Cu(OH)₂ (indicated as Peak 2).^[36, 37] Under more anodic potentials, another broad oxidation peak starts to appear (Peak 3), implying the formation of a duplex surface film consisted of an inner Cu₂O layer and an outer CuO|Cu(OH)₂ layer.^[36, 37] In the reduction process, two obvious reduction peaks correspond to the Cu(II)-to-Cu(I) and Cu(I)-to-Cu(II) reduction reactions, which are denoted as Peak 4 and Peak 5, respectively.^[37] To obtain a more comprehensive understanding of the Cu oxidation process, a further study was performed in the less anodic region (as shown in Figure S3.9). From the results, it can be seen that the Cu oxidation is suppressed, indicating that the neighboring Au atoms potentially inhibit this oxidation process^[38], and the oxidation peak of Cu is slightly positively shifted, suggesting that the

oxygen binding is weakened on Au-Cu alloys due to the *d*-band center shifting away from Fermi level.^[39]

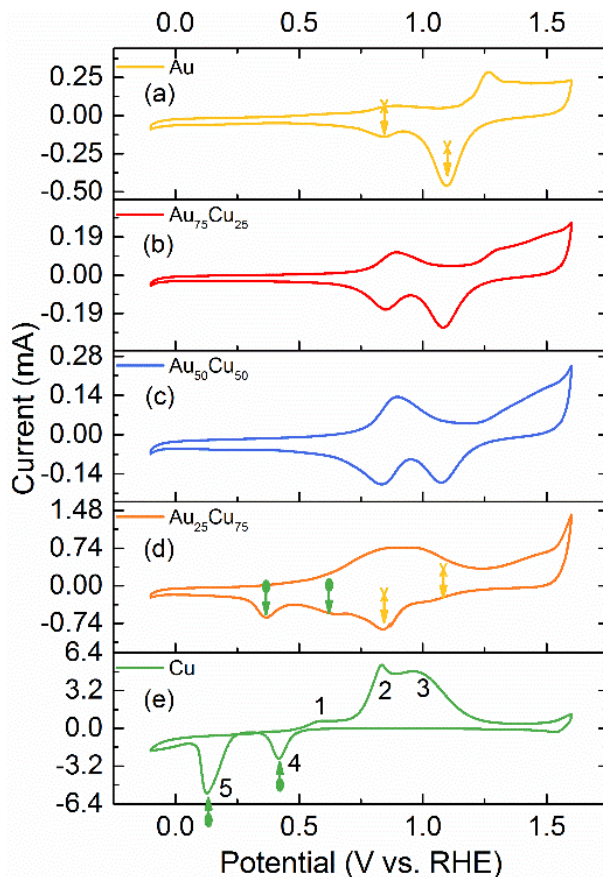


Figure 3.5: Cyclic voltammograms of sputtered catalysts in N_2 -saturated 0.5 M KOH at a scan rate of 50 mV/s. (a) Au, (b) $Au_{75}Cu_{25}$, (c) $Au_{50}Cu_{50}$, (d) $Au_{25}Cu_{75}$, (e) Cu. The reduction peaks of copper oxides species are marked by green arrows with dots. The reduction waves of gold are marked by yellow arrows with crosses.

As the sputtered samples exhibit an almost identical planar morphology, the effect owing to the adsorption/desorption of electrolyte species on the precise evaluation of interfacial capacitance can be extracted from electrochemical impedance spectroscopy (EIS).^[40] For CO_2RR , it can be assumed that the imaginary component of the impedance (Z'') represents the dynamic adsorption process occurring at the interface. The surface coverage is

extracted from EIS following a previously published method.^[41] When the electrode surface is fully covered by analyte, this imaginary component of the impedance is denoted as Z''_{\max} . The Z'' induced by faradaic adsorption of reactant species is denoted as Z''_{ads} . The surface coverage percentage is determined by the ratio of Z''_{ads} to Z''_{\max} .^[41] As shown in Figure 3.6, the descending trend of the surface coverage as a function of applied potentials over all the samples demonstrates the fast reaction kinetics under high overpotentials.^[41]

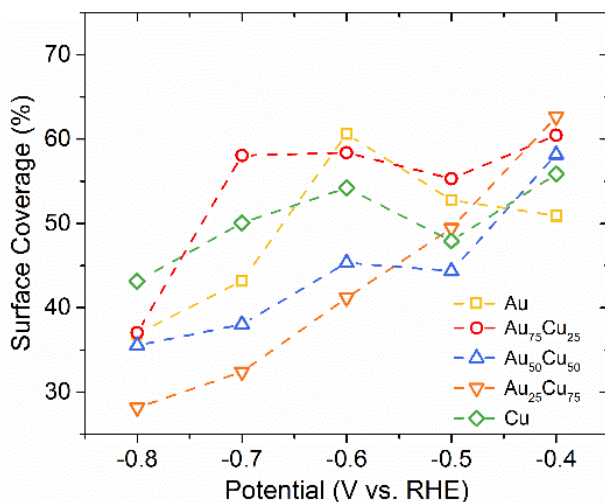


Figure 3.6: Potential-dependent surface coverage of faradaic adsorption extracted from EIS data.

Facile charge transfer kinetics is observed by EIS with negatively increased potentials. As gold has a relative lower onset potential than copper, the charge transfer resistance (R_{ct}) on Au is lower than that on Cu in the low potential region ($< -0.3\text{V}$ vs RHE). Also, the R_{ct} of Au-Cu alloys was decreased in the less negative potential region with increasing Au content (seen in Figure 3.7a). When the overpotential is high enough to efficiently prompt the CO_2RR , the difference in R_{ct} between the electrodes shrinks rapidly, indicating that a significant kinetical improvement in HER and CO_2RR driven by the applied potentials. The detailed plots of charge transfer resistance as a function of composition and applied potential are shown in Figure S3.13. As the lattice strain at the surface could influence the binding strength of

intermediates reducing the overall energy barrier,^[29] the relationship between microstrain and charge transfer resistance is presented in Figure 3.7b. It is clearly shown that the low charge transfer resistance is in line with the high microstrain, which implies that the microstrain derived from grain boundaries could promote the overall electrochemical kinetics. This direct correlation between microstrain and charge transfer resistance gives important insights to the significance of surface electronic properties of thin films, the adsorption of reactant molecules, and the kinetics of electrocatalysis.

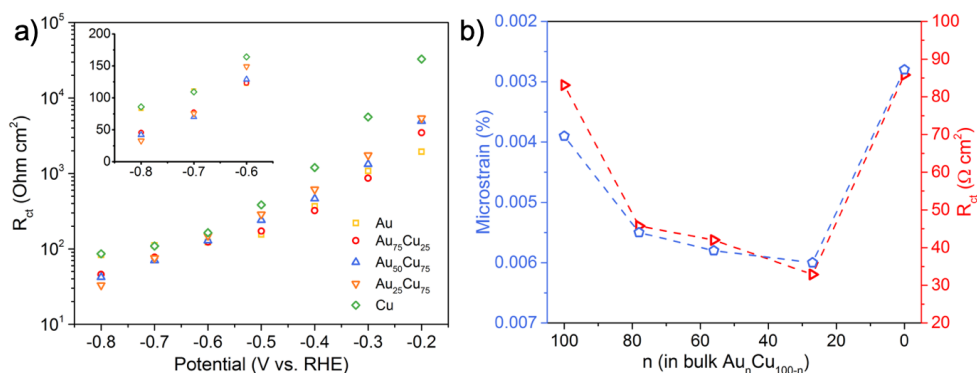


Figure 3.7: Comparison of charge transfer resistance. (a) Charge transfer resistance of bimetallic thin films in the potential range of -0.2 V to -0.8 V vs RHE. Inset: zoom in the potential region of -0.6 V to -0.8 V vs RHE. (b) Relationship between the microstrain derived from XRD data and charge transfer resistance (@ -0.8V vs RHE) extracted from EIS.

The adsorbed CO is a key intermediate for CO_2RR , and Cu has intermediate binding strength for $*CO$ allowing the formation of C2 or C3 products, while Au owns the optimum binding strength for $*COOH$ and $*CO$ prompting the conversion from CO_2 to CO.^[5] CO stripping experiments could elucidate the variation of CO binding strength introduced by the change of electronic structure and the amount of active sites by calculating the amount of absorbed-desorbed CO. As summarized in Table 3.2, the CO coverage was dramatically reduced even with a small content of Au, revealing that Au can significantly lower the desorption energy of CO and decrease the population of surface bounded CO, which is consistent with the large d -band center shift from pure Cu to $Au_{25}Cu_{75}$ (seen in Figure 3.4).

Table 3.2: CO coverage determined by CO stripping.

Samples	CO oxidation charge (μC)	CO coverage ($\text{nmol}^{-1} \text{cm}^{-2}$)
Au	4.9	0.13
Au ₇₅ Cu ₂₅	13.0	0.34
Au ₅₀ Cu ₅₀	10.0	0.26
Au ₂₅ Cu ₇₅	13.4	0.35
Cu	24.2	0.63

3.2.4 Electrocatalytic performance of Au-Cu bimetallic thin films for CO₂ RR

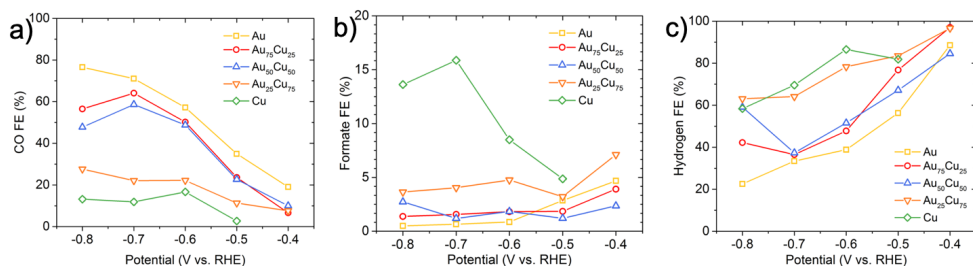


Figure 3.8: Comparison of the electrocatalytic performance for CO₂ reduction. Faradaic efficiency of (a) CO, (b) HCOO⁻ and (c) H₂ with varied potentials and compositions.

In the investigated potential region, no hydrocarbons were detected, as only H₂, CO and HCOO⁻ were found, indicating that the activation energy is not high enough or the concentration of hydrocarbons is below the detection limit of the gas chromatography.^[42] The FE_{CO} scales with the composition and applied potential (seen in Figure 3.8a), as the more negative potential can provide higher activation energy for CO₂RR and the higher Au content can decrease the *COOH formation energy and lower *CO binding energy, which selectively makes the formation of CO more favorable.^[14] As it is proposed that either the stronger or weaker oxygen binding on Cu sites could be able to optimize the binding strength of *COOH on Au-Cu interfaces,^[13, 16] however, no obvious enhancement is observed here, which could be ascribed to the significant weakened *CO binding.^[8] On the other hand, the formation of HCOO⁻ was strongly suppressed with the introduction of Au (seen in Figure 3.8b). This dramatic suppression can be ascribed to the significantly

weakened oxygen binding strength as the d -band center shifts away from the Fermi level with the increasing Au content, which limits the formation of $*\text{OCHO}$.^[3] As the CO_2RR requires higher activation energy than HER,^[43] there is no obvious inhibition of HER on the thin films under low overpotentials. In the high overpotential region, the HER on high Au-content catalysts is inhibited (Figure 3.8c), which is due to the improved CO_2RR activity in bimetallic samples with increased Au content and the more favorable binding of CO_2RR intermediates on Au-Cu alloys.^[44, 45]

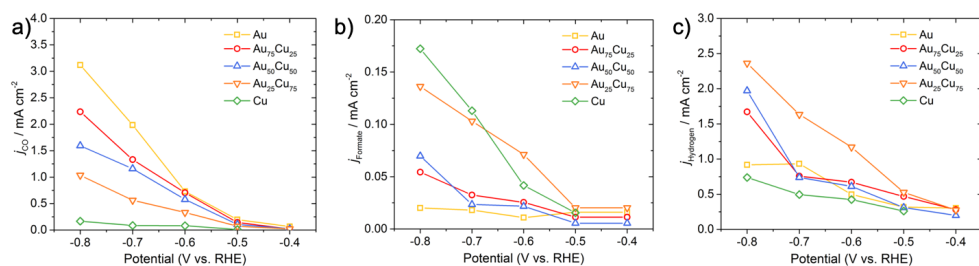


Figure 3.9: Activity of bimetallic catalysts for two-electron products. Partial current densities of (a) CO , (b) HCOO^- and (c) H_2 are shown as a function of applied potentials. Inset: zoom in the potential region of -0.4 V to -0.6 V vs RHE.

The total current density of all samples was found to increase steadily as the applied potential raised negatively (seen in Figure S3.14). The partial current density of CO was correspondingly enhanced with the increase of Au content, indicating that the activity for CO production is strongly influenced by the presence of Au, which can lower the activation energy of CO_2RR and reduce the desorption energy of $*\text{CO}$ accelerating the CO production. Based on the analysis of CO formation, it is clearly shown that the catalytic activity for CO formation is almost linear with the increase of Au content, which demonstrates that the CO generation rate follows the shift of the d -band center, such that the d -band theory seems to be the dominant factor affecting activity and selectivity for CO in this planar Au-Cu bimetallic system (seen in Figure 3.4).

The CO_2RR and the hydrogen evolution reaction not only compete but also interact with each other. The surface bound CO_2RR species may impede HER, and the $*\text{H}$ binding energy could be altered by surface adsorbed

species.^[44, 46] Notably, although Cu has an intermediate binding strength of CO, the activity of HER is not significantly affected by the introduction of Au to Cu across the investigated potential region (seen in Figure 3.9c), which is due to the fact that Au and Cu exhibit similar activity in the HER volcano plot with the presence of CO₂.^[46] It is important to note that the HER activity is not inhibited by alloying on Au-Cu bimetallic surfaces, revealing that the improved selectivity to CO is resulted from the enhanced activity for CO on Au-Cu alloys instead of the suppression of HER.

The Au₂₅Cu₇₅ film exhibits relatively higher HER activity than the other samples, which may be due to the surface atomic re-arrangement taking place when the applied potential is above -0.6 V vs RHE, resulting in the surface Au content increasing to 35% (seen in Table S3.2). This instability is consistent with simulation results.^[47] In Au-Fe nanoparticles, it was observed that the Fe atoms leach out, leaving more Au active sites on the surface that can prompt the production of CO.^[48] Notwithstanding, the surface re-arrangement introducing more surface Au atoms, the j_{CO} still falls in line with the shift of the *d*-band center derived from the variation of composition. The surface re-arrangement on Au₂₅Cu₇₅ shows no obvious contribution to the CO production, on the contrary, it suggests that the CO activity is governed by the bulk electronic structure. The H₂ current density on Au₂₅Cu₇₅ is strongly elevated as the applied potential was increased more negative, which implies the surface reconstruction exposes more active sites for HER. As presented in Figure 3.6, the surface coverage on Au₂₅Cu₇₅ declines rapidly with the negatively increasing potential, which can be attributed to the improved HER. Moreover, even though the bimetallic catalysts contain more microstrain (seen in Table 3.1), the performance of these Au-Cu alloy samples still follows the ascending trend in CO formation with the increase of Au content, which implies that the bulk electronic effect on Au-Cu for CO production is the governing effect over the additional Au active sites and microstrain.

It is reported that Au could increase the CO concentration near the surface and elevate the local pH by enhanced water splitting, and these conditions may facilitate the formation of C₂/C₂₊ products on Cu surfaces.^[26, 49]

Notwithstanding, there are no detectable C_2 products on the planar Au-Cu alloys, instead, the selectivity to formate is dramatically inhibited along with the prompted evolution of CO with the increasing Au content (seen in 0), suggesting that the formation of formate is unlikely to follow the reaction pathway through the *COOH intermediate on the binary Au-Cu metallic thin films.^[50] The current density of formate declines rapidly as the Au content increases (seen in 0), yet there is no obvious linear relationship between the composition and activity, especially in the potential region that the overpotential is relatively high and the CO_2 mass transport limitation is minimized, e.g. -0.7 V and -0.6 V vs RHE. These observations could be ascribed to: (1) the variation in *OCHO binding energy has a strong influence on $HCOO^-$ production, e.g. a much faster declining trend in $HCOO^-$ formation. In the volcano plots of CO and $HCOO^-$, the difference in j_{CO} between Cu and Au is around 1 order of magnitude, however, the difference in $j_{formate}$ is around 2 orders of magnitude^[3]; (2) the enhanced HER on $Au_{25}Cu_{75}$ could facilitate the formation of $HCOO^-$ by prompting the proton transfer to *OCHO . As observed in the CV scans, the positively shifted reduction peak of copper oxide/hydroxide species may suggest the lowered oxygen affinity on the surface, which also relates to the low oxophilicity of the alloy, possibly resulting in a weakened binding of oxygen-bonded *OCHO .^[3, 39] It has been confirmed that, on Au-Pt and Au-Pd, the activity of CO formation is consistent with the Au composition, which demonstrates that the *COOH binding strength is tuned by the electronic effect as the d -band center shifts along with the variation of Au content. On the other hand, these two kinds of Au-based alloys exhibit an enhanced activity for $HCOO^-$ formation.^[20, 21] However, on planar binary Au-Cu thin films, the varied electronic structure with increased Au content seems to be able to not only promotes CO formation by lowering the formation energy of *COOH and reducing the desorption energy of *CO , it also could suppress the production of $HCOO^-$ via decreasing the binding affinity of *OCHO to the low activity region. In addition, by comparing the relative position of Cu and Pt in the volcano plot of $HCOO^-$, it can be found that Pt has an even lower *OCHO binding energy than Cu, implying that the averaged *OCHO binding strength

of Au and Pt seems unlikely to play a dominant role to improve the selectivity to HCOO^- . Considering Pt and Pd both are strong $^*\text{CO}$ and optimum $^*\text{H}$ binding metals, the effect of surface adsorbates on HCOO^- formation and the proton transfer for HCOO^- production may be worth to be further explored.

3.3 Conclusions

In this work, uniformly deposited Au-Cu bimetallic films with controlled composition were explored as a platform to study the isolated electronic effect and remove effects of nano/mesostructuring for CO_2 electroreduction. The introduction of Au can significantly reshape the d -band electronic structure and notably weakens the binding strength of $^*\text{CO}$. Similar to the planar Au-Pt alloys, the d -band electronic structure of Au-Cu alloys can be tuned by varying the composition to adjust the $^*\text{CO}$ binding energy in these bimetallic systems. The activity and selectivity for the reduction of CO_2 to CO was gradually improved with increasing Au content, revealing that the electronic effect itself can not solely break the linear scaling relationship without nanostructure engineering. Nevertheless, the as-prepared Au-Cu alloy was imparted with a degree of nobility by gold, the copper oxide/hydroxide species on Au-Cu surfaces were less stable than those on pure copper, indicating that Au could also lower the binding strength between copper and oxygen on the alloy surface. As the surface oxophilicity could be critical to the formation of HCOO^- , alloying Cu with Au can decrease the adsorption energy of $^*\text{OCHO}$, thus inhibiting the formation of HCOO^- . The electronic effect/ d -band structure could strongly influence the formation of HCOO^- , however, the activity of HCOO^- does not scale with the compositional shift. Considering Cu has an intermediate $^*\text{CO}$ binding and relatively low $^*\text{H}$ binding energy compared to Pt and Pd, the non-linear correlation between j_{formate} and composition requires more theoretical effort to investigate the relationship between composition, structure and selectivity.

3.4 Experimental Section

3.4.1 Preparation of Au-Cu bimetallic thin films by magnetron sputtering

The bimetallic thin films were fabricated by a previously published co-deposition method.^[20] Briefly, the magnetron sputtering targets of Au (99.99%, MaTeck GmbH) and Cu (99.99%, MaTeck GmbH) are powered by radio frequency (RF) and direct current (DC) generators, respectively. The deposition power and duration were precisely controlled to obtain films with a desired thickness (80 nm) and composition ratios on Ti foil substrates.

3.4.2 Morphological Investigation

The large-scale morphology was investigated under scanning electron microscope (SEM, JEOL JSM-6010LA). The surface roughness was characterized by atomic force microscopy (AFM, Bruker).

3.4.3 Structural Characterization

The crystal structure of bimetallic thin films were characterized by X-ray diffraction (XRD) using a diffractometer (Bruker D8 Discover). The bulk composition was determined by Energy-dispersive X-ray spectroscopy (EDS, JEOL JSM-6010LA). X-ray photoelectron spectroscopy (XPS, Thermo ScientificTM K-AlphaTM) was conducted to confirm the composition on the surface.

3.4.4 Electrochemical measurements

Electrochemical measurements were carried out in a 2-compartment home-made cell. The cathode and anode components were separated by an anion exchange membrane (AEM, Fumasep FAB-PK-130). Electrochemical impedance spectroscopy (EIS) was carried out under the same conditions as CO₂ reduction. CO stripping was conducted in the same cell. Briefly, 0.1 M KHCO₃ electrolyte was bubbled with Ar for 15 min with vigorously stirring. All the samples were pre-reduced by holding a potential at -0.2 V vs RHE for 100 s to ensure the surface was metallic and no residual oxides were present on the surface. CO adsorption was performed at 0.1 V vs RHE with purging

CO for 15 min, meanwhile the absorbed H was released. Prior to CO stripping, the electrolyte was bubbled with Ar for 20 min to remove the excessive dissolved CO. The scan range of CO stripping was from 0 V to +1.5 V vs RHE at a scan rate of 50 mV/s.

3.4.5 Catalytic performance

The gaseous products were analyzed by gas chromatography (GC, Interscience). The cathodic compartment was sparged with CO₂ at a constant flow rate and the outlet was directly connected to a gas chromatograph. Liquid products of the CO₂RR were collected and quantified by ¹H nuclear magnetic resonance (NMR, Agilent) after the electrolysis.

References

- (1) Kuhl, K.P., Hatsukade, T., Cave, E.R., Abram, D.N., Kibsgaard, J., and Jaramillo, T.F., Electrocatalytic Conversion of Carbon Dioxide to Methane and Methanol on Transition Metal Surfaces. *J. Am. Chem. Soc.* **2014**, 136(40): p. 14107-14113.
- (2) Resasco, J., Chen, L.D., Clark, E., Tsai, C., Hahn, C., Jaramillo, T.F., Chan, K., and Bell, A.T., Promoter Effects of Alkali Metal Cations on the Electrochemical Reduction of Carbon Dioxide. *J. Am. Chem. Soc.* **2017**, 139(32): p. 11277-11287.
- (3) Feaster, J.T., Shi, C., Cave, E.R., Hatsukade, T., Abram, D.N., Kuhl, K.P., Hahn, C., Nørskov, J.K., and Jaramillo, T.F., Understanding Selectivity for the Electrochemical Reduction of Carbon Dioxide to Formic Acid and Carbon Monoxide on Metal Electrodes. *ACS Catal.* **2017**, 7(7): p. 4822-4827.
- (4) Singh, M.R., Kwon, Y., Lum, Y., Ager, J.W., and Bell, A.T., Hydrolysis of Electrolyte Cations Enhances the Electrochemical Reduction of CO₂ over Ag and Cu. *J. Am. Chem. Soc.* **2016**, 138(39): p. 13006-13012.
- (5) Hansen, H.A., Varley, J.B., Peterson, A.A., and Nørskov, J.K., Understanding Trends in the Electrocatalytic Activity of Metals and Enzymes for CO₂ Reduction to CO. *J. Phys. Chem. Lett.* **2013**, 4(3): p. 388-392.
- (6) Peterson, A.A. and Nørskov, J.K., Activity Descriptors for CO₂ Electroreduction to Methane on Transition-Metal Catalysts. *J. Phys. Chem. Lett.* **2012**, 3(2): p. 251-258.
- (7) Mistry, H., Reske, R., Strasser, P., and Roldan Cuenya, B., Size-dependent reactivity of gold-copper bimetallic nanoparticles during CO₂ electroreduction. *Catal. Today* **2016**, 288: p. 30-36.
- (8) Kim, D., Xie, C., Becknell, N., Yu, Y., Karamad, M., Chan, K., Crumlin, E.J., Nørskov, J.K., and Yang, P., Electrochemical Activation of CO₂ through Atomic Ordering Transformations of AuCu Nanoparticles. *J. Am. Chem. Soc.* **2017**, 139(24): p. 8329-8336.

- (9) Hong, X., Chan, K., Tsai, C., and Nørskov, J.K., How Doped MoS₂ Breaks Transition-Metal Scaling Relations for CO₂ Electrochemical Reduction. *ACS Catal.* **2016**, 6(7): p. 4428-4437.
- (10) Kuhl, K.P., Cave, E.R., Abram, D.N., and Jaramillo, T.F., New Insights into the Electrochemical Reduction of Carbon Dioxide on Metallic Copper Surfaces. *Energy Environ. Sci.* **2012**, 5(5): p. 7050-7059.
- (11) Chan, K., Tsai, C., Hansen, H.A., and Nørskov, J.K., Molybdenum Sulfides and Selenides as Possible Electrocatalysts for CO₂ Reduction. *ChemCatChem* **2014**, 6(7): p. 1899-1905.
- (12) Higgins, D., Landers, A.T., Ji, Y., Nitopi, S., Morales-Guio, C.G., Wang, L., Chan, K., Hahn, C., and Jaramillo, T.F., Guiding Electrochemical Carbon Dioxide Reduction toward Carbonyls Using Copper Silver Thin Films with Interphase Miscibility. *ACS Energy Lett.* **2018**: p. 2947-2955.
- (13) Back, S., Kim, J.-H., Kim, Y.-T., and Jung, Y., Bifunctional Interface of Au and Cu for Improved CO₂ Electroreduction. *ACS Appl. Mater. Interfaces* **2016**, 8(35): p. 23022-23027.
- (14) Kim, D., Resasco, J., Yu, Y., Asiri, A.M., and Yang, P., Synergistic Geometric and Electronic Effects for Electrochemical Reduction of Carbon Dioxide Using Gold–Copper Bimetallic Nanoparticles. *Nat. Commun.* **2014**, 5: p. 4948.
- (15) Ross, M.B., Dinh, C.T., Li, Y., Kim, D., De Luna, P., Sargent, E.H., and Yang, P., Tunable Cu Enrichment Enables Designer Syngas Electrosynthesis from CO₂. *J. Am. Chem. Soc.* **2017**, 139(27): p. 9359-9363.
- (16) Andrews, E., Fang, Y., and Flake, J., Electrochemical Reduction of CO₂ at CuAu Nanoparticles: Size and Alloy Effects. *J. Appl. Electrochem.* **2018**, 48(4): p. 435-441.
- (17) Chang, Z., Huo, S., Zhang, W., Fang, J., and Wang, H., The Tunable and Highly Selective Reduction Products on Ag@Cu Bimetallic Catalysts Toward CO₂ Electrochemical Reduction Reaction. *J. Phys. Chem. C* **2017**, 121(21): p. 11368-11379.
- (18) Ma, M., Trześniewski, B.J., Xie, J., and Smith, W.A., Selective and Efficient Reduction of Carbon Dioxide to Carbon Monoxide on Oxide-Derived Nanostructured Silver Electrocatalysts. *Angew. Chem. Int. Ed.* **2016**, 55(33): p. 9748-9752.

-
- (19) Yoon, Y., Hall, A.S., and Surendranath, Y., Tuning of Silver Catalyst Mesostructure Promotes Selective Carbon Dioxide Conversion into Fuels. *Angew. Chem. Int. Ed.* **2016**, 55(49): p. 15282-15286.
- (20) Ma, M., Hansen, H.A., Valenti, M., Wang, Z., Cao, A., Dong, M., and Smith, W.A., Electrochemical Reduction of CO₂ on Compositionally Variant Au-Pt Bimetallic Thin Films. *Nano Energy* **2017**, 42: p. 51-57.
- (21) Hahn, C., Abram, D.N., Hansen, H.A., Hatsukade, T., Jackson, A., Johnson, N.C., Hellstern, T.R., Kuhl, K.P., Cave, E.R., Feaster, J.T., and Jaramillo, T.F., Synthesis of Thin Film AuPd Alloys and Their Investigation for Electrocatalytic CO₂ Reduction. *J. Mater. Chem. A* **2015**, 3(40): p. 20185-20194.
- (22) Ma, M., Djanashvili, K., and Smith, W.A., Controllable Hydrocarbon Formation from the Electrochemical Reduction of CO₂ over Cu Nanowire Arrays. *Angew. Chem. Int. Ed.* **2016**, 55(23): p. 6680-6684.
- (23) Peters, T.A., Kaleta, T., Stange, M., and Bredeisen, R., Development of Thin Binary and Ternary Pd-Based Alloy Membranes for Use in Hydrogen Production. *Journal of Membrane Science* **2011**, 383(1): p. 124-134.
- (24) Smith, W., Fakhouri, H., Pulpytel, J., Mori, S., Grilli, R., Baker, M.A., and Arefi-Khonsari, F., Visible Light Water Splitting via Oxidized TiN Thin Films. *J. Phys. Chem. C* **2012**, 116(30): p. 15855-15866.
- (25) Thornton, J.A., Influence of Apparatus Geometry and Deposition Conditions on the Structure and Topography of Thick Sputtered Coatings. *J. Vac. Sci. Technol* **1974**, 11(4): p. 666-670.
- (26) Morales-Guio, C.G., Cave, E.R., Nitopi, S.A., Feaster, J.T., Wang, L., Kuhl, K.P., Jackson, A., Johnson, N.C., Abram, D.N., Hatsukade, T., Hahn, C., and Jaramillo, T.F., Improved CO₂ Reduction Activity towards C₂₊ Alcohols on a Tandem Gold on Copper Electrocatalyst. *Nat. Catal.* **2018**, 1(10): p. 764-771.
- (27) Chang, F., Shan, S., Petkov, V., Skeete, Z., Lu, A., Ravid, J., Wu, J., Luo, J., Yu, G., Ren, Y., and Zhong, C.-J., Composition Tunability and (111)-Dominant Facets of Ultrathin Platinum–Gold Alloy Nanowires toward Enhanced Electrocatalysis. *J. Am. Chem. Soc.* **2016**, 138(37): p. 12166-12175.

- (28) Feng, X., Jiang, K., Fan, S., and Kanan, M.W., Grain-Boundary-Dependent CO₂ Electroreduction Activity. *J. Am. Chem. Soc.* **2015**, 137(14): p. 4606-4609.
- (29) Mariano, R.G., McKelvey, K., White, H.S., and Kanan, M.W., Selective Increase in CO₂ Electroreduction Activity at Grain-Boundary Surface Terminations. *Science* **2017**, 358(6367): p. 1187-1192.
- (30) Feng, X., Jiang, K., Fan, S., and Kanan, M.W., A Direct Grain-Boundary-Activity Correlation for CO Electroreduction on Cu Nanoparticles. *ACS Cent. Sci.* **2016**, 2(3): p. 169-174.
- (31) Rosenberg, Y., Machavariani, V.S., Voronel, A., Garber, S., Rubshtein, A., Frenkel, A., and Stern, E., Strain Energy Density in the X-Ray Powder Diffraction from Mixed Crystals and Alloys. *J. Phys.: Condens. Matter* **2000**, 12(37): p. 8081-8088.
- (32) Hofmann, T., Yu, T.H., Folse, M., Weinhardt, L., Bär, M., Zhang, Y., Merinov, B.V., Myers, D.J., Goddard, W.A., and Heske, C., Using Photoelectron Spectroscopy and Quantum Mechanics to Determine d-Band Energies of Metals for Catalytic Applications. *J. Phys. Chem. C* **2012**, 116(45): p. 24016-24026.
- (33) Norskov, J.K., Bligaard, T., Rossmeisl, J., and Christensen, C.H., Towards the computational design of solid catalysts. *Nat. Chem.* **2009**, 1(1): p. 37-46.
- (34) Tominaga, M., Shimazoe, T., Nagashima, M., Kusuda, H., Kubo, A., Kuwahara, Y., and Taniguchi, I., Electrocatalytic Oxidation of Glucose at Gold-Silver Alloy, Silver and Gold Nanoparticles in an Alkaline Solution. *J. Electroanal. Chem.* **2006**, 590(1): p. 37-46.
- (35) Kunze, J., Maurice, V., Klein, L.H., Strehblow, H.-H., and Marcus, P., In Situ Scanning Tunneling Microscopy Study of the Anodic Oxidation of Cu(111) in 0.1 M NaOH. *J. Phys. Chem. B* **2001**, 105(19): p. 4263-4269.
- (36) Kunze, J., Maurice, V., Klein, L.H., Strehblow, H.-H., and Marcus, P., In situ STM study of the duplex passive films formed on Cu(111) and Cu(001) in 0.1 M NaOH. *Corros. Sci.* **2004**, 46(1): p. 245-264.
- (37) Maurice, V., Strehblow, H.H., and Marcus, P., In situ STM study of the initial stages of oxidation of Cu(111) in aqueous solution. *Surf. Sci.* **2000**, 458(1): p. 185-194.

- (38) Higgins, D., Wette, M., Gibbons, B.M., Siahrostami, S., Hahn, C., Escudero-Escribano, M.a., García-Melchor, M., Ulissi, Z., Davis, R.C., Mehta, A., Clemens, B.M., Nørskov, J.K., and Jaramillo, T.F., Copper Silver Thin Films with Metastable Miscibility for Oxygen Reduction Electrocatalysis in Alkaline Electrolytes. *ACS Appl. Energy Mater.* **2018**, 1(5): p. 1990-1999.
- (39) Okada, M., Tsuda, Y., Oka, K., Kojima, K., Diño, W.A., Yoshigoe, A., and Kasai, H., Experimental and Theoretical Studies on Oxidation of Cu-Au Alloy Surfaces: Effect of Bulk Au Concentration. *Sci. Rep.* **2016**, 6: p. 31101.
- (40) Shrikrishnan, S., Sankaran, K., and Lakshminarayanan, V., Electrochemical Impedance Analysis of Adsorption and Enzyme Kinetics of Calf Intestine Alkaline Phosphatase on SAM-Modified Gold Electrode. *J. Phys. Chem. C* **2012**, 116(30): p. 16030-16037.
- (41) Shah, A.H., Wang, Y., Woldu, A.R., Lin, L., Iqbal, M., Cahen, D., and He, T., Revisiting Electrochemical Reduction of CO₂ on Cu Electrode: Where Do We Stand about the Intermediates? *J. Phys. Chem. C* **2018**, 122(32): p. 18528-18536.
- (42) Monzo, J., Malewski, Y., Kortlever, R., Vidal-Iglesias, F.J., Solla-Gullon, J., Koper, M.T.M., and Rodriguez, P., Enhanced Electrocatalytic Activity of Au@Cu Core@Shell Nanoparticles towards CO₂ Reduction. *J. Mater. Chem. A* **2015**, 3(47): p. 23690-23698.
- (43) Martin, A.J., Larrazabal, G.O., and Perez-Ramirez, J., Towards Sustainable Fuels and Chemicals through the Electrochemical Reduction of CO₂: Lessons from Water Electrolysis. *Green Chem.* **2015**, 17(12): p. 5114-5130.
- (44) Ooka, H., Figueiredo, M.C., and Koper, M.T.M., Competition between Hydrogen Evolution and Carbon Dioxide Reduction on Copper Electrodes in Mildly Acidic Media. *Langmuir* **2017**, 33(37): p. 9307-9313.
- (45) Lee, S., Park, G., and Lee, J., Importance of Ag–Cu Biphasic Boundaries for Selective Electrochemical Reduction of CO₂ to Ethanol. *ACS Catal.* **2017**, 7(12): p. 8594-8604.
- (46) Cave, E.R., Shi, C., Kuhl, K.P., Hatsukade, T., Abram, D.N., Hahn, C., Chan, K., and Jaramillo, T.F., Trends in the Catalytic Activity of Hydrogen

- Evolution during CO₂ Electroreduction on Transition Metals. *ACS Catal.* **2018**, 8(4): p. 3035-3040.
- (47) Hansen, H.A., Shi, C., Lausche, A.C., Peterson, A.A., and Nørskov, J.K., Bifunctional alloys for the electroreduction of CO₂ and CO. *Phys. Chem. Chem. Phys.* **2016**, 18(13): p. 9194-9201.
- (48) Sun, K., Cheng, T., Wu, L., Hu, Y., Zhou, J., MacLennan, A., Jiang, Z., Gao, Y., Goddard, W.A., and Wang, Z., Ultrahigh Mass Activity for Carbon Dioxide Reduction Enabled by Gold–Iron Core–Shell Nanoparticles. *J. Am. Chem. Soc.* **2017**, 139(44): p. 15608-15611.
- (49) Dinh, C.-T., Burdyny, T., Kibria, M.G., Seifitokaldani, A., Gabardo, C.M., García de Arquer, F.P., Kiani, A., Edwards, J.P., De Luna, P., Bushuyev, O.S., Zou, C., Quintero-Bermudez, R., Pang, Y., Sinton, D., and Sargent, E.H., CO₂ Electroreduction to Ethylene via Hydroxide-Mediated Copper Catalysis at an Abrupt Interface. *Science* **2018**, 360(6390): p. 783-787.
- (50) Yoo, J.S., Christensen, R., Vegge, T., Nørskov, J.K., and Studt, F., Theoretical Insight into the Trends that Guide the Electrochemical Reduction of Carbon Dioxide to Formic Acid. *ChemSusChem* **2016**, 9(4): p. 358-363.

Supporting Information for Chapter 3

SEM images

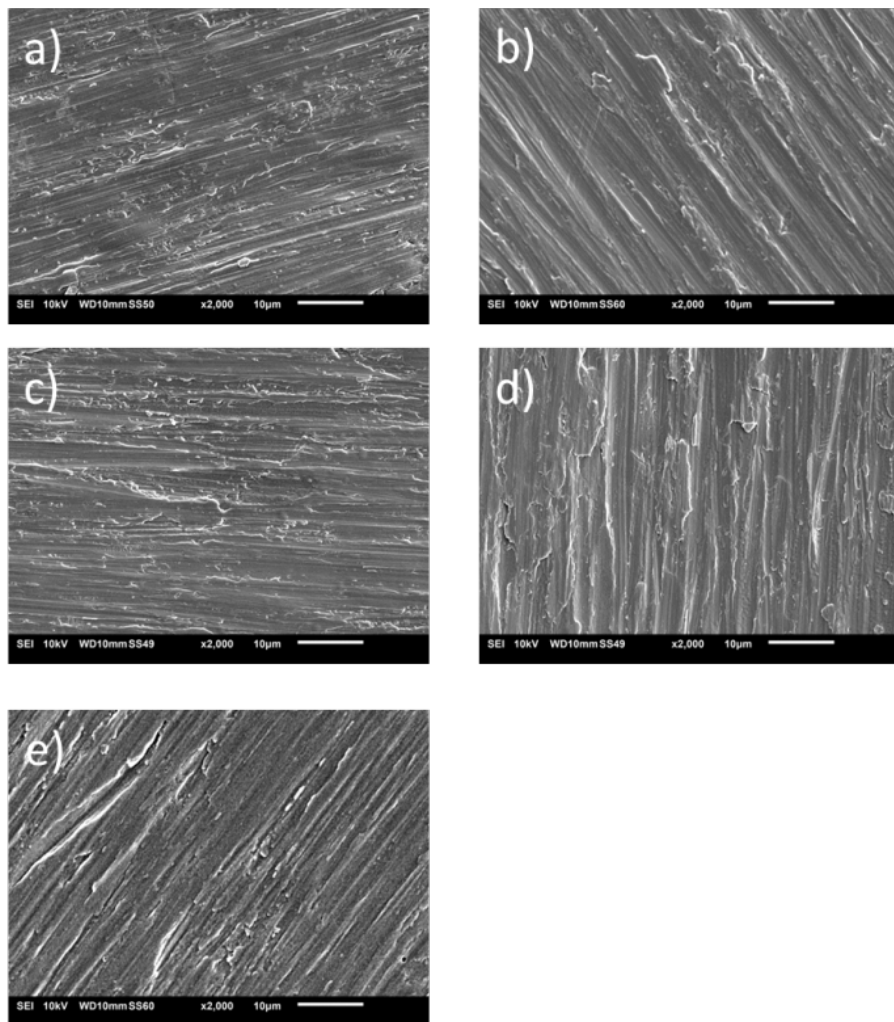


Figure S3.1: SEM images of as-prepared samples a) Au, b) $\text{Au}_{75}\text{Cu}_{25}$, c) $\text{Au}_{50}\text{Cu}_{50}$, d) $\text{Au}_{25}\text{Cu}_{75}$, e) Cu. The thin films follow the morphology of the Ti foil. The scale bar is 10 μm .

AFM images

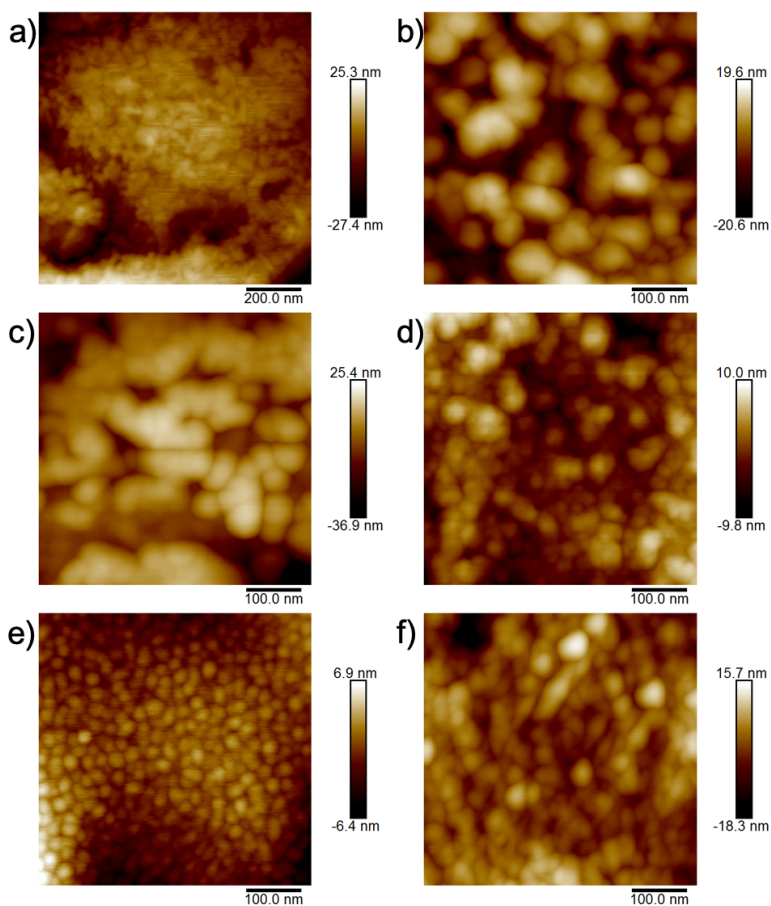


Figure S3.2: AFM images of as-prepared Au-Cu thin films (a) bare Ti foil and as-prepared catalyst films, (b) Au, (c) Au₇₅Cu₂₅, (d) Au₅₀Cu₅₀, (e) Au₂₅Cu₇₅, (f) Cu thin film before CO₂RR.

Surface roughness

Table S3.1: The surface roughness of the as-deposited films

Sample	Average R_{RMS} (nm)	St. deviation R_{RMS} (nm)
Bare Ti foil	2.1	2.6
Au	2.7	3.3
Au ₇₅ Cu ₂₅	4.1	4.8
Au ₅₀ Cu ₅₀	5.3	6.4
Au ₂₅ Cu ₇₅	4.5	5.4
Cu	4.4	5.4

Double layer capacitance

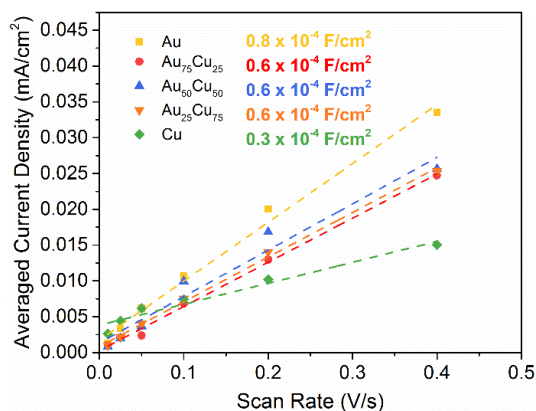


Figure S3.3: Double layer capacitances (C_{dl}) are extracted from the plot of averaged cathodic and anodic current densities in cyclic voltammetry versus scan rate. The C_{dl} is applied to determine the relative surface areas of the Au, Cu and Au-Cu alloys.

XRD data processing

The lattice spacing $d_{(111)}$ is determined by applying Bragg's law, which can be expressed as

$$n\lambda_{Co,K\alpha} = 2d_{(111)} \sin \theta$$

As both of Au and Cu are face-centered cubic (FCC) crystalline materials, the lattice parameter a is calculated from the lattice spacing $d_{(111)}$ as follows:

$$a = \sqrt{3}d_{(111)}$$

The Vegard's law is applied to predict the theoretical lattice parameters of the alloys and validate the characteristic of alloying^[27], which is given by:

$$a_{Au_nCu_{100-n}} = na_{Au} + (100 - n)a_{Cu}$$

Comparison of theoretical and actual composition in the bulk

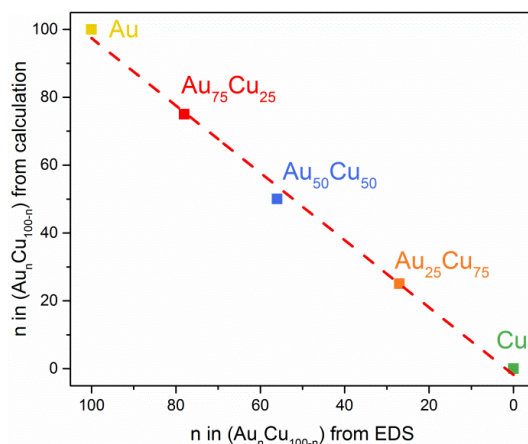


Figure S3.4: The comparison of EDS composition with the calculated composition ratio. (slope: 0.99, $R^2 = 0.9981$)

Auger XPS and depth profile XPS

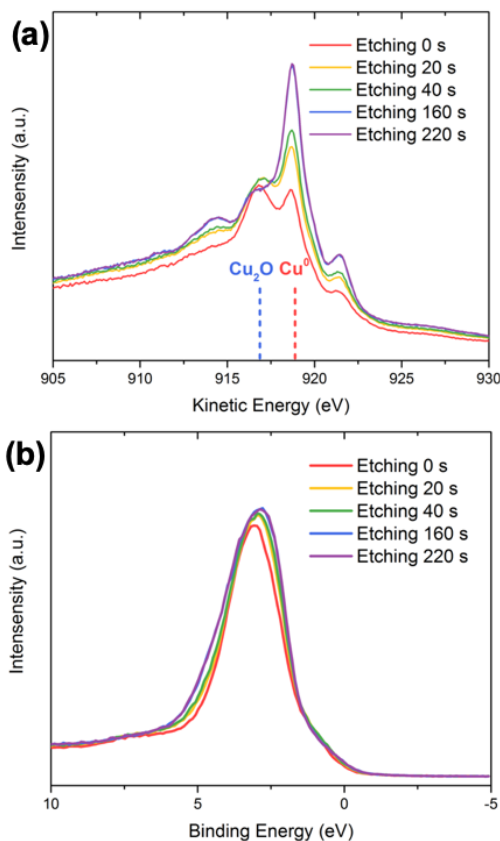


Figure S3.5: Auger XPS and depth profile XPS of sputtered Cu after exposed to air.

Table S3.2: The d-band center of the as-prepared samples analyzed with depth profile XPS.

Sample	d-band center before etching	d-band center after 160 s etching
Cu	3.23	3.27
Au ₂₅ Cu ₇₅	3.98	4.01
Au ₅₀ Cu ₅₀	4.14	4.12

XPS spectra of the copper 2p and gold 4f

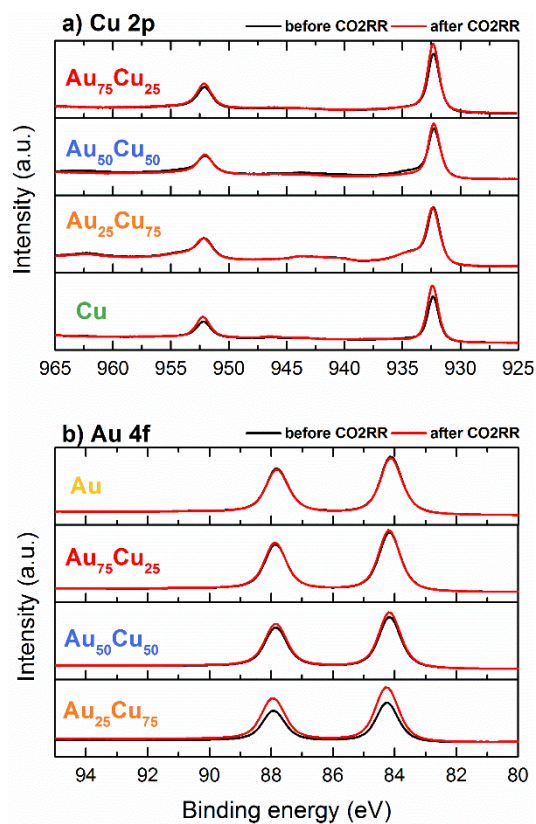


Figure S3.6: XPS spectra of the (a) copper 2p and (b) gold 4f of the as-prepared samples before and after CO₂ reduction testing.

Composition of Au₂₅Cu₇₅ before and after CO₂RR

Table S3.3: The surface composition of Au₂₅Cu₇₅ before and after CO₂RR determined by XPS

	As-prepared	@ -0.6V vs RHE	@ -0.7V vs RHE	@ -0.8V vs RHE
Au (%)	28.3	35.0	35.1	57.2
Cu (%)	71.7	65.0	64.9	42.8

Valence band XPS

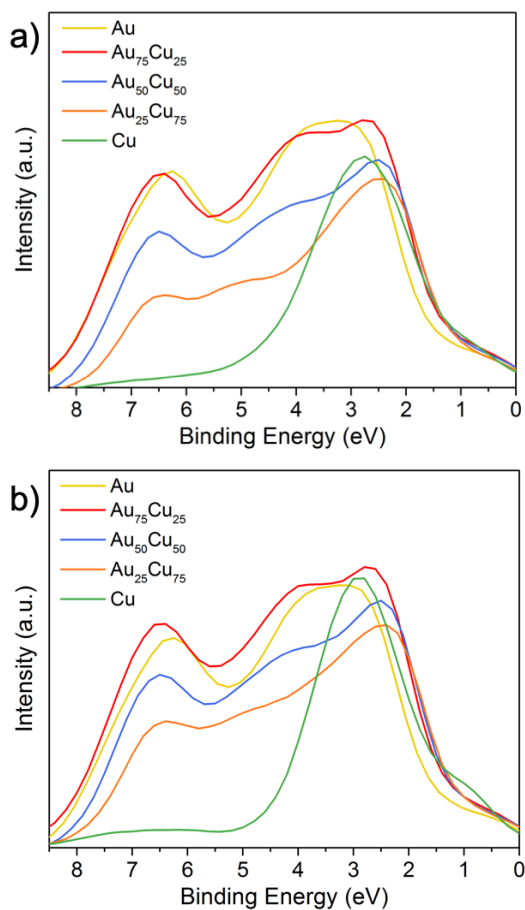


Figure S3.7: Valence band XPS of the thin films (a) before and (b) after CO₂RR at -0.8 V vs RHE.

d-band center

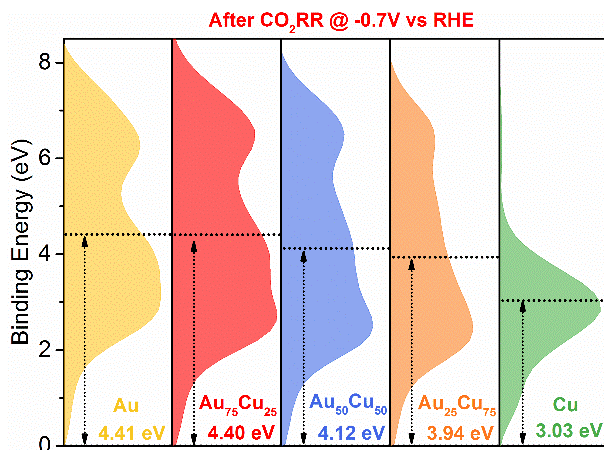


Figure S3.8: Surface valence band X-ray photoemission spectra of the as-prepared Au, Cu and alloys after CO₂RR @ -0.7 V vs RHE. The gravity center of the valence band center is shown in dotted line compared to 0 eV.

Cyclic voltammograms

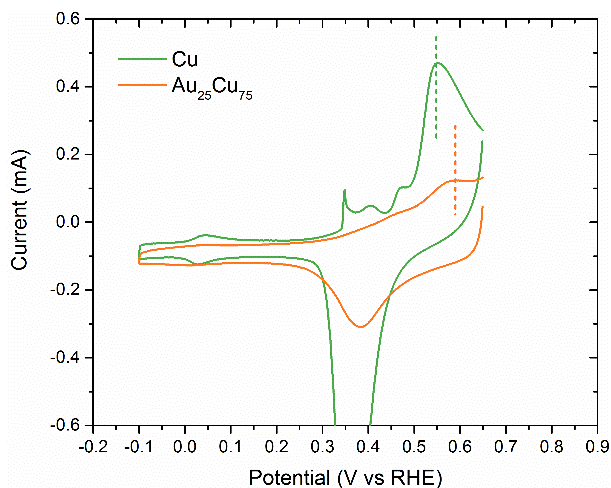


Figure S3.9: Cyclic voltammograms of Cu and Au₂₅Cu₇₅ electrodes in Ar-saturated 0.5 M KOH at a scan rate of 50 mV/s in the range from -0.1 V to 0.65 V vs RHE.

Cyclic voltammograms of CO stripping

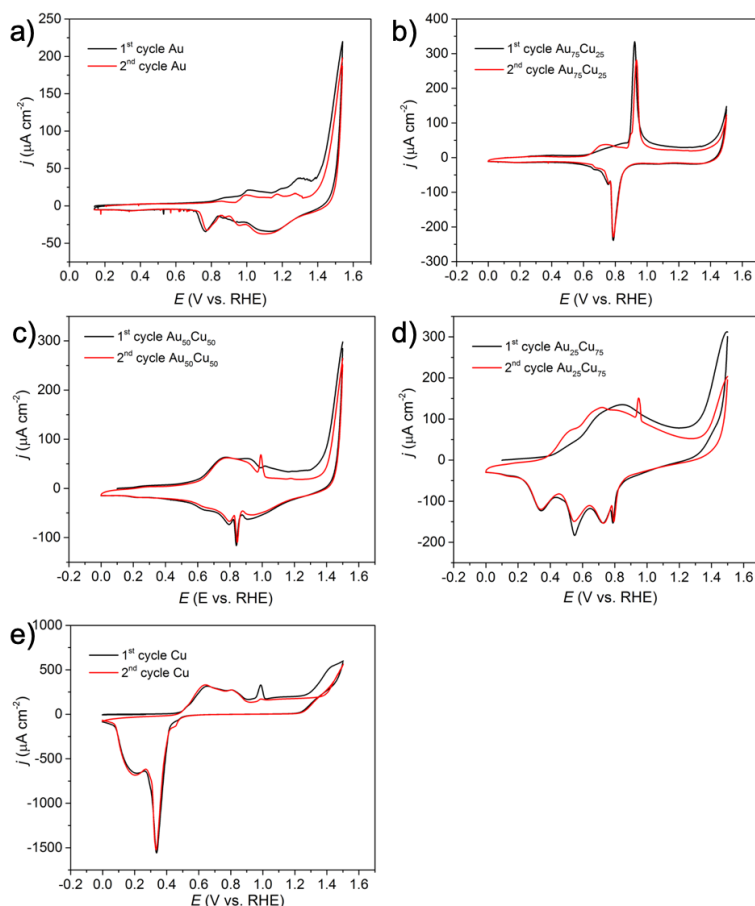


Figure S3.10: Cyclic voltammograms of CO stripping on the as-prepared thin films in 0.1 M KHCO₃ electrolyte (a) Au, (b) Au₇₅Cu₂₅, (c) Au₅₀Cu₅₀, (d) Au₂₅Cu₇₅, (e) Cu.

CO coverage

The CO coverage was calculated by the following equation,

$$CO\ coverage = \frac{CO\ oxidation\ charge}{n_{electron} * charge_{electron} * N_A * Area_{electrode}}$$

Electrochemical impedance spectroscopy

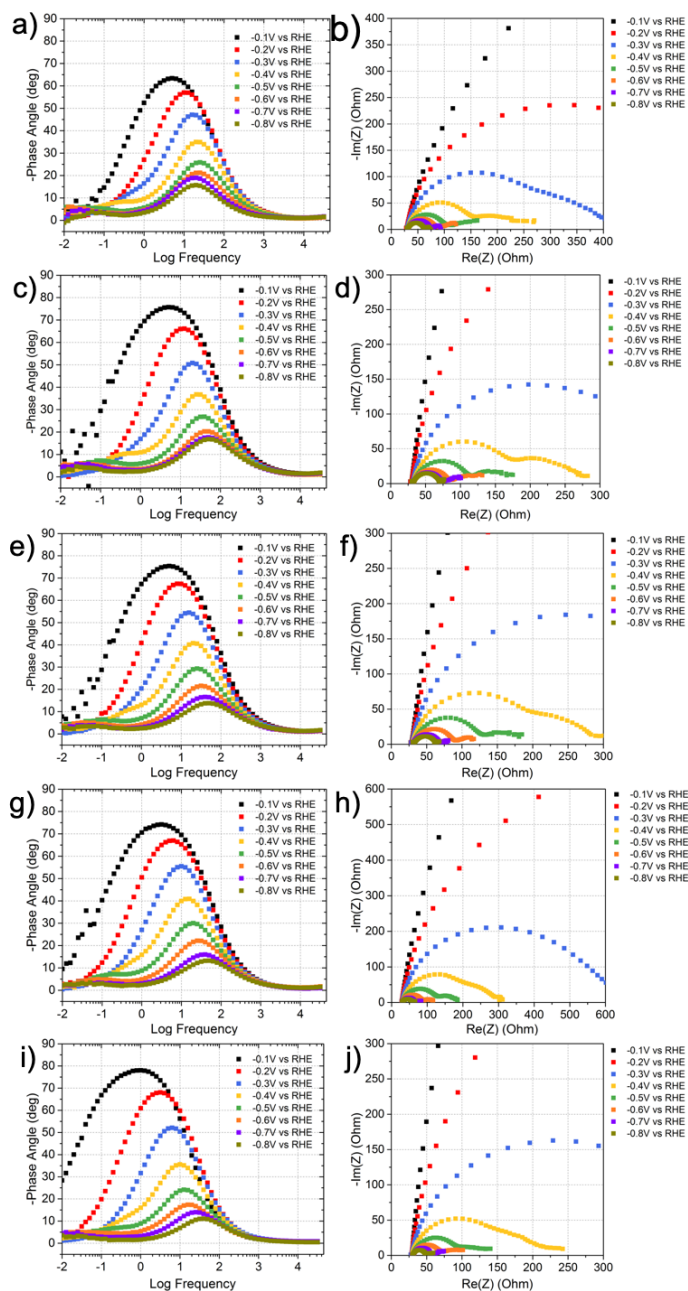


Figure S3.11: EIS Bode and Nyquist plots of the sputtered films, (a-b) Au, (c-d) Au₇₅Cu₂₅, (e-f) Au₅₀Cu₅₀, (g-h) Au₂₅Cu₇₅, (i-j) Cu in CO₂-saturated 0.1 M KHCO₃ electrolyte (pH 6.8) at various potentials.

Equivalent circuit

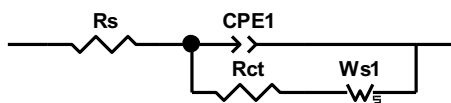


Figure S3.12: Equivalent circuit for the metal/solution interface (R_{ct} , R_s , CPE and W_s are charge transfer resistance, solution resistance, constant phase element, and Warburg-short circuit terminus, respectively).

Charger transfer resistance

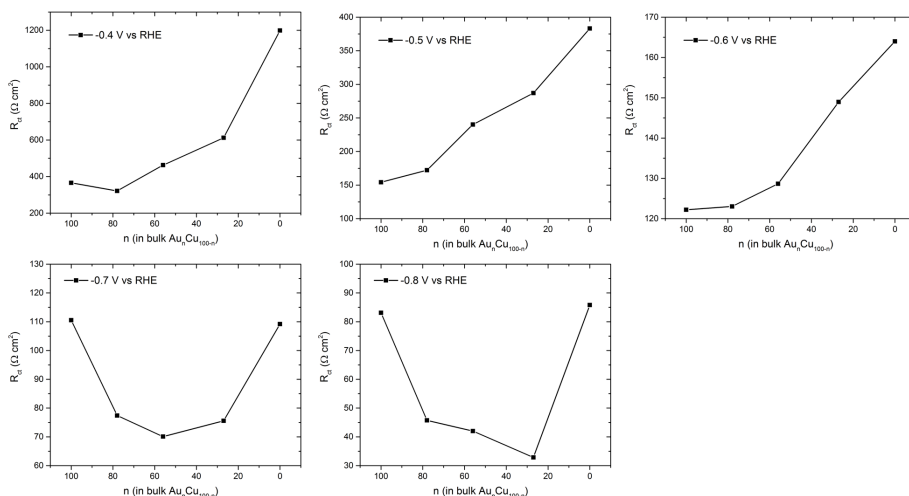


Figure S3.13: Charge transfer resistance extracted from EIS under CO_2 reduction conditions at various potentials.

Table S3.4: Capacitance extracted from EIS data under various potentials.

Applied Potentail	Capacitance of Au (mF/cm ²)	Capacitance of Au ₇₅ Cu ₂₅ (mF/cm ²)	Capacitance of Au ₅₀ Cu ₅₀ (mF/cm ²)	Capacitance of Au ₂₅ Cu ₇₅ (mF/cm ²)	Capacitance of Cu (mF/cm ²)
- 0.4 V	0.067305	0.07501	0.087745	0.10621	0.11694
- 0.5 V	0.07795	0.092285	0.13526	0.146225	0.15372
- 0.6 V	0.107905	0.145805	0.140665	0.1629	0.16214
- 0.7 V	0.119515	0.13239	0.136025	0.16078	0.162195
- 0.8 V	0.11383	0.13288	0.143885	0.16085	0.167275

Total current density under CO₂RR conditions

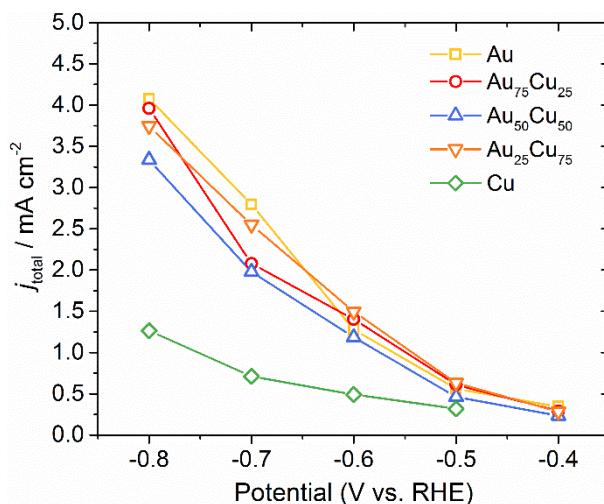


Figure S3.14: Total current density of Au-Cu bimetallic films under CO₂RR conditions.

Faradaic efficiency as a function of composition

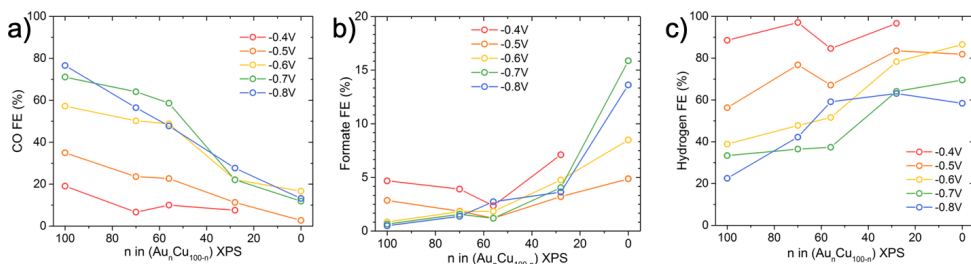


Figure S3.15: Faradaic efficiency of Au-Cu bimetallic films as a function of Au content.

Reference

- (1) Chang, F., et al., Composition Tunability and (111)-Dominant Facets of Ultrathin Platinum–Gold Alloy Nanowires toward Enhanced Electrocatalysis. *J. Am. Chem. Soc.*, 2016. **138**(37): p. 12166-12175.

Experimental Intricacies of Performing CO₂ Reduction at Higher Current Densities Using Gas- Diffusion Layers

4

This chapter is meant to describe some of these unique operational considerations that can impact catalytic activity and our ability to accurately collect data, while acting as a starting guide for researchers to transition to using gas-diffusion layers as a platform for benchmarking novel catalysts at commercially viable current densities.

4.1 Introduction

A global transition away from energy dense and cheap fossil fuels will require the commercial implementation of numerous new energy technologies, each of which must be scaled to large enough sizes to impact existing markets and substantially lower global CO₂ emissions. The electrochemical conversion of CO₂ to chemicals, fuels and feedstocks has shown enough promise in the past decade to justify both academic and industrial sectors to increase efforts to better assess the potential economic and technical feasibility of the technology. Intensifying the process towards an industrial scale can be achieved by higher production rates, either by simply increasing the total area of catalyst in a reactor, or by increasing the reaction rate (current density) for a given area of catalyst. Both approaches will be needed to economically produce an industrial quantity of product in a single plant (e.g. >100 tons product/day).

In electrochemical CO₂ reduction, however, increasing current densities to those needed for commercial operation (e.g. >200 mA/cm²) requires researchers to use cell designs that can supply enough CO₂ to the catalyst layer to fuel the reaction, as opposed to traditional H-cell reactors. For these reasons, more and more researchers have begun using catalysts deposited onto gas-diffusion layers, where high concentrations of CO₂ can be maintained in close proximity to the catalyst layer even at high reaction rates. Gas-diffusion layers can also reduce overall cell potentials by directly improving catalytic activity, while a more system-focussed testing platform can help reduce major system losses such as ohmic heating. Researchers operating these experimental devices at higher current densities, however, have discovered a number of operational intricacies that can make the direct switch away from lower current densities experiments in an H-cell challenging. This chapter is meant to describe some of these unique operational considerations which can impact catalytic activity and our ability to accurately collect data, while acting as a starting guide for researchers to transition to using gas-diffusion layers as a platform for benchmarking novel catalysts at commercially-viable current densities.

Specific discussion points here may apply broadly across all platforms for performing high current density CO₂ reduction, while others pertain specifically to our presented cell configuration consisting of three chambers and a catalyst layer deposited onto a gas-diffusion layer (GDL) (Figure 4.1). Membrane electrode assemblies, which show promise in the reduction of overall cell potentials in future systems, are a similar cell configuration with additional operational intricacies brought on by a stagnant or extremely small catholyte layer.^[1-5] For researchers new to high current density testing however, the three chamber configuration can provide an easy platform to rapidly test new catalysts and gas-diffusion layers.^[6-9] This chapter briefly discusses the intricacies of operating gas-diffusion layers for CO₂ electroreduction through three main subtopics: assembly, operation and post-analysis of data.

4.2 Results and Discussion

In electrochemical systems, a catalyst is typically deposited onto a substrate, with carbon paper, glassy carbon and metal foils being common supports. In high current density experiments, a gas-diffusion layer^[10-12] commonly acts as a support for the catalyst. A catalyst is typically deposited directly onto the microporous layer side of the GDL, which is hydrophobic and helps to form a gas-liquid interface between the microporous layer and the catalyst. The creation of new gas-diffusion layers specifically with mechanical and chemical properties suited for CO₂ reduction applications will be an important avenue for new research going forward,^[13, 14] but most current systems report using commercially-available GDL's such as Sigracet 39BC or variations from Freudenberg or Covestro. The hydrophobic nature of bare carbon-based GDL's and an as-prepared GDL with a 100 nm layer of sputtered silver is investigated. Here, it is found that after the surface has been briefly placed under reducing potentials, a separately prepared 150 nm thick Cu catalyst layer becomes fully-wetted when a droplet of water is pipetted on top. The bare GDL without a catalyst layer, however, maintains its hydrophobic surface even after being placed in reductive conditions. During operation, commonly-used metallic and porous catalyst layers (e.g. Ag, Au, Cu) are then

assumed to be fully-covered by the electrolyte, while CO_2 diffuses across a gas-liquid interface provided by the hydrophobic surface of the microporous layer inside the GDL. It is assumed that CO_2 travels a short distance and reacts in dissolved form rather than a gaseous form with a three-phase interface.^[15]

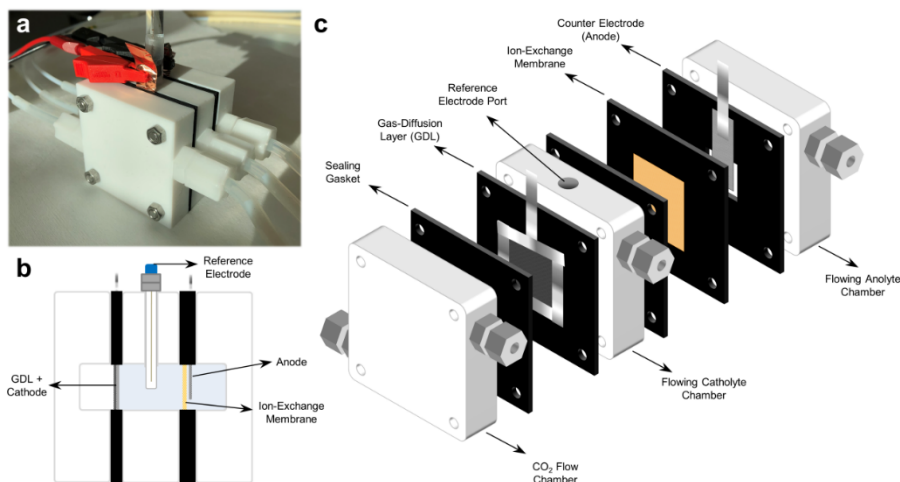


Figure 4.1: (a) A standard electrochemical for CO_2 electrolysis for testing catalysts in a 3-electrode configuration. (b) Side profile showing chambers for the CO_2 (left), catholyte (centre) and anolyte (right). (c) Isometric view of the exploded three-chamber cell showing individual components.

The diffusion of CO_2 from a nearby gas phase not only allows for much higher current densities than an H-cell, but has consequences for the morphology, activity and stability of the catalyst layer. In an H-cell, for example, even a nanostructured catalyst functions as a planar electrode, relying on CO_2 to diffuse 40-120 μm to reach the catalyst layer. In this configuration almost all CO_2 reduction measurements are then performed under some degree of mass transport limitations, resulting in concentration polarizations and making intrinsic activity difficult to accurately determine and potentially overestimated.^[16] For a rough nanostructured electrode with a surface porosity of several microns, only the outermost surfaces may have access to sufficient reagent, while the base can be depleted of CO_2 .^[17] In a GDL, however, the catalyst layer must allow for access to CO_2 on one side, and electrolyte on the other side, resulting in a porous electrode structure

compared to the planar system in an H-cell. In this configuration, a large electrochemically active surface area is then possible with all surfaces of the catalyst having comparatively greater access to CO_2 due to the short diffusion pathway compared to that in an H-cell. Thus, the greater surface area for CO_2 reduction can then result in greater geometric activity at lower overpotentials than H-cell experiments. Further, a GDL can allow for gaseous products to diffuse into the gas phase prior to nucleating at the surface and blocking active sites. A challenge that results from this orientation, however, is the potential for hydroxide and carbonates to build-up inside the structure before they can be transported to the bulk electrolyte. Crystallization of salts can then be a common occurrence within the porous catalyst layer, especially at higher current densities where substantial hydroxide is generated.^[18] These considerations should then be factored into the design of catalyst structures for CO_2 reduction, in addition to the design and composition of the material itself. Finally, in an H-cell configuration, impurities are easily deposited onto the outermost catalyst sites, which can cause fast deactivation of CO_2 reduction in favor of hydrogen evolution, as these sites possess the greatest access to CO_2 coming from the bulk electrolyte. Due to the opposite direction of CO_2 transport within a GDL system, however, impurities are likely to deposit onto the catalyst surfaces furthest from the source of CO_2 .^[15]

In the Supplementary Information, the electrical connection and sealing of a GDL within a cell is also important. Here, conductive tape is applied on the gas-side (non-catalyst side) of the GDL composed of carbon fibres to provide an electrical connection to the potentiostat, but also to physically fix it to the sealing gasket during cell assembly. More importantly, conductive tape is applied around the entire electrode instead of just at the top, in order to minimize the in-plane distance that electrons travel through the GDL to reach the CO_2 reduction catalyst. Sufficient current collection is extremely important for higher current density operation due to the relatively-high resistivity of commonly-used GDLs ($\sim 10^6\times$ more resistive than pure Cu), which can cause potential/voltage variations across the GDL and catalyst layer that scale with the applied current density (via Ohm's Law; $V_{\text{drop_GDL}} = IR_{\text{GDL}}$). These potential variations can then result in heterogeneous local

current distributions across the catalyst layer. In terms of CO₂ reduction and catalyst characterization, non-uniform potential and current density throughout the catalyst layer could then result in location-dependent product formation and differences in the local reaction environment (e.g. pH), irrespective of the catalyst used.

This intricacy of high-current density CO₂ electrolysis is particularly important for CO₂ reduction on copper electrodes, due to the sensitivity of pH and current density on H₂, CO and C₂ product formation.^[13, 19, 20] These implications can be illustrated in Figure 4.2a by assuming an ideal catalyst with an overall activity of 120 mV/dec (after iR and local pH correction). In this figure, we can see the differences in the sensitivity of overpotential and the local pH as a function of the geometric current density. An applied potential difference of only 36 mV induced by resistive losses on this electrode could then result in current density variations from 100 mA/cm² to 200 mA/cm², which could then result in large spatial differences in the local reaction environment across the electrode surface. The lower current density region (eg. 0.01-10 mA/cm²), however, is less sensitive to these effects due to the exponential relationship between overpotential and current density, and the dependency of the GDL's resistive losses on the current density. These considerations are then unique to only high current density catalyst-testing and applications. It is thus important to emphasize that catalytic activity at higher current densities can be strongly influenced by non-catalytic electrode variations, such as the resistivity of the GDL, how current is collected, and the overall electrode size.

Assembly of the entire cell for electrochemical testing can be seen step-by-step in the Supporting Information. Here and in Figure 4.1, it can be seen that the overall simplicity of the cell design, but also the typical ancillary equipment needed to run the device such as a pump to flow liquid through the electrolyte channels and a gas-chromatographer (GC) to measure the formed gaseous products. In high current density experiments, it is also important to note that the concentration of product gases entering the GC increases significantly as compared to H-cell testing, which can impact product

measurement. Multi-point calibration of a GC across the concentration range of all of the expected gas products (H_2 , CO , CH_4 , C_2H_4) is then necessary as the concentrations produced may no longer be within a linear range, known as the Limit of Linearity (illustrated using H_2 in Figure 4.2b). This can lead to overall Faradaic Efficiencies greater than 100% if the lower concentration calibrations typically used in H-cell testing are extrapolated. This can be particularly misleading if liquid products are not measured or reported in the total Faradaic Efficiency measurement, as the observed total FE of gas products may still be below 100%. While it is possible to increase the gas flow rate to reduce the GC's measured concentrations back to a linear calibration range, this may cause pressure imbalances between the gas/liquid phases within the GDL, while reducing the single-pass conversion efficiency of CO_2 . Similarly, since the GC peak areas are related to the total applied current, the overall geometric catalyst area can also be reduced. Either way, it is essential that the GC is properly calibrated within the range of concentrations that are produced, instead of extrapolating from lower concentration calibration data.

During operation of a GDL or membrane-electrode assembly, other operational factors may cause instability or complicate analysis of electrochemical behavior if not taken into consideration. At higher current densities, much higher ohmic drops between the working and reference electrode can be expected due to the larger charge passed through the electrolyte. Not only can this be a major contributing factor to the overall cell potential in a 2-electrode setup, but it must be taken into account when correcting for the potential of the working CO_2 reduction cathode in a 3-electrode system. While electrochemical impedance spectroscopy (EIS) is typically performed even in H-cells to determine a system's ohmic drop between the working and reference electrodes, the measured electrolyte resistance value between the reference and working electrodes can also be shown to vary as a function of the current density (Figure 4.2c). Here, using two different methods and several replicates, the solution resistance is found to decrease with the applied current density. This means that iR determination and correction may require resistance measurements at various conditions to

capture the real working potential of a cathode. In the case of the 1 M KHCO_3 electrolyte used to acquire this data, the change in electrolyte resistance is likely due to an overall increase in electrolyte conductivity due to the generation of hydroxide at the cathode surface. This will change the electrical properties of the electrolyte within the diffusion region, but can also change the overall pH and conductivity of the bulk catholyte over time, particularly if the buffer breaks down. Alternatively, if 1 M KOH is used as a catholyte, long exposure to gaseous CO_2 via the GDL may cause the pH to steadily decline due to the spontaneous formation of bicarbonate, along with a corresponding reduction in the conductivity of the electrolyte. Unless accounted for, these factors can cause the determined working potential of the cathode to differ from an iR correction performed at 0 mA/cm^2 .

Additionally, the large ohmic drop throughout the system driven by high current density operation can result in large temperature changes to the electrolyte, further affecting solution conductivity, electrode activity (via Arrhenius' Law) and the solubility of CO_2 diffusing across the gas-liquid interface. Without a sufficient electrolyte volume and passive cooling of the electrolyte chambers to mitigate the heating in the system, these temperature changes will affect the observed electrochemical results. Even worse, over a multi-hour stability test, the temperature can increase gradually, providing transient operating conditions. Additional strategies to avoid this include minimizing the electrolyte distance between the anode and cathode, and using a high conductivity electrolyte to facilitate charge transport.

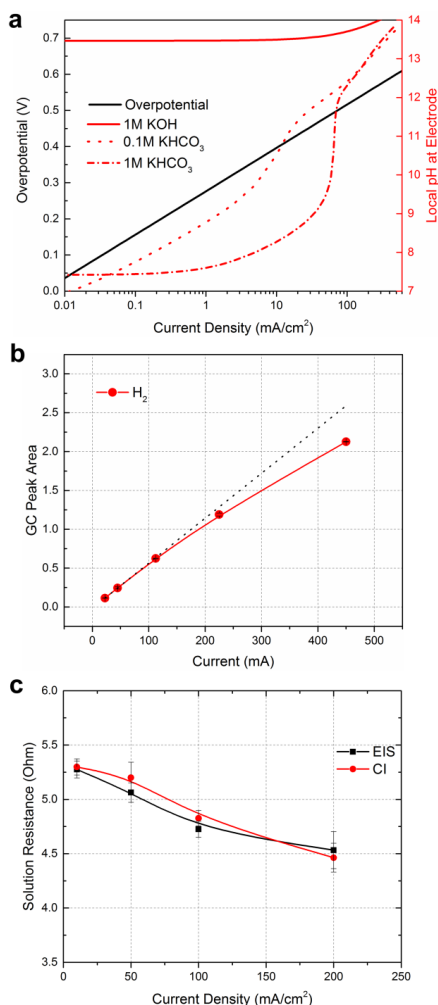


Figure 4.2: Examples of important considerations when benchmarking catalytic CO₂ reduction performance under high current density operation. (a) Comparative effect of current density on the ideal required overpotential and the local reaction environment, showing how the system behaves differently as a function of current density. (b) Effect of high current operation on the measured peak area of H₂ as recorded by a gas chromatographer, showing deviation from the limit of linearity (dashed) at high concentrations (2.25 cm² geometric area). (c) Measured solution resistance between the working and reference electrode as a function of applied current density using both current interrupt (CI) and electrochemical impedance spectroscopy (EIS) (1 M KHCO₃ is used as an electrolyte). This illustrates changes in the electrolyte conductivity as a function of operation and current density.

A final complexity of operating GDL's pertains to the delicate gas/liquid interface that provides gaseous CO₂ in close proximity to the catalyst. Even slight overpressures on either the gas or liquid side of the GDL can cause gas to bubble into the liquid phase, or result in flooding of the GDL. If possible, the pressure of both phases across the GDL should then be regulated to ensure that catalytic activity can be determined without additional uncertainties introduced by stability of the gas/liquid interface. One notable source of pressure imbalance can even come from in-line GC's connected to the cell. Here, a constant backpressure from the GC, as well as pressure increases during injections, can cause gas to enter the liquid phase if the pressure spike is too high. For GC's which use syringe injections, however, the CO₂ gas pressure is easier to maintain near atmospheric pressure.

4.3 Conclusions

In summary, this chapter discusses several operational intricacies of using gas-diffusion layers for electrochemical CO₂ reduction, which is becoming increasingly important as the number of reports at higher current densities grows. The differences in testing/optimizing catalyst performance between traditional aqueous H-cell's and gas diffusion electrodes is not trivial, and many new protocols must be used to ensure proper sample preparation, recording of data, and product identification. However, with proper care and attention, the large field of catalyst researchers working on CO₂ electroreduction can leverage existing infrastructures to expedite the scientific development of this technology. This chapter is designed to acts as a source of information for catalyst-focussed researchers looking to move to high current density catalyst testing, and reinforces the need for fundamental research performed under practical conditions.

4.4 Experimental Section

Materials. For the experiments, KHCO₃ ($\geq 97\%$) and KOH (45 wt. % in H₂O), were purchased from Sigma Aldrich. All chemicals were used without

further purification. Millipore Type 1 water (18.2 M Ω) was used throughout the study to form the electrolytes.

Preparation of Cu gas-diffusion electrode. A nominal thickness of 150 nm of copper metal was deposited on gas-diffusion layer by magnetron sputtering. The deposition parameters give a rate of $\sim 1.4 \text{ \AA s}^{-1}$ on flat glass substrate. The electrochemical experiments were performed in the cell described in the previous paper.

References

- (1) Salvatore, D.A., Weekes, D.M., He, J., Dettelbach, K.E., Li, Y.C., Mallouk, T.E., and Berlinguette, C.P., Electrolysis of Gaseous CO₂ to CO in a Flow Cell with a Bipolar Membrane. *ACS Energy Lett.* **2018**, 3(1): p. 149-154.
- (2) Li, Y.C., Zhou, D., Yan, Z., Gonçalves, R.H., Salvatore, D.A., Berlinguette, C.P., and Mallouk, T.E., Electrolysis of CO₂ to Syngas in Bipolar Membrane-Based Electrochemical Cells. *ACS Energy Lett.* **2016**, 1(6): p. 1149-1153.
- (3) Ripatti, D.S., Veltman, T.R., and Kanan, M.W., Carbon Monoxide Gas Diffusion Electrolysis that Produces Concentrated C₂ Products with High Single-Pass Conversion. *Joule* **2018**, 3(1): p. 240-256.
- (4) Kaczur, J.J., Yang, H., Liu, Z., Sajjad, S.D., and Masel, R.I., Carbon Dioxide and Water Electrolysis Using New Alkaline Stable Anion Membranes. *Frontiers in Chemistry* **2018**, 6(263): p. 263.
- (5) Vennekoetter, J.-B., Sengpiel, R., and Wessling, M., Beyond the catalyst: how electrode and reactor design determine the product spectrum during electrochemical CO₂ reduction. *Chem. Eng. J.* **2019**.
- (6) Dinh, C.-T., García de Arquer, F.P., Sinton, D., and Sargent, E.H., High Rate, Selective, and Stable Electroreduction of CO₂ to CO in Basic and Neutral Media. *ACS Energy Lett.* **2018**: p. 2835-2840.
- (7) Jhong, H.-R.M., Tornow, C.E., Kim, C., Verma, S., Oberst, J.L., Anderson, P.S., Gewirth, A.A., Fujigaya, T., Nakashima, N., and Kenis, P.J.A., Gold Nanoparticles on Polymer-Wrapped Carbon Nanotubes: An Efficient and Selective Catalyst for the Electroreduction of CO₂. *ChemPhysChem* **2017**, 18(22): p. 3274-3279.
- (8) Zhuang, T.-T., Liang, Z.-Q., Seifitokaldani, A., Li, Y., De Luna, P., Burdyny, T., Che, F., Meng, F., Min, Y., Quintero-Bermudez, R., Dinh, C.T., Pang, Y., Zhong, M., Zhang, B., Li, J., Chen, P.-N., Zheng, X.-L., Liang, H., Ge, W.-N., Ye, B.-J., Sinton, D., Yu, S.-H., and Sargent, E.H., Steering post-C–C coupling selectivity enables high efficiency electroreduction of carbon dioxide to multi-carbon alcohols. *Nat. Catal.* **2018**, 1(6): p. 421-428.
- (9) Kibria, M.G., Dinh, C.-T., Seifitokaldani, A., De Luna, P., Burdyny, T., Quintero-Bermudez, R., Ross, M.B., Bushuyev, O.S., García de Arquer,

- F.P., Yang, P., Sinton, D., and Sargent, E.H., A Surface Reconstruction Route to High Productivity and Selectivity in CO₂ Electroreduction toward C₂+ Hydrocarbons. *Adv. Mater.* **2018**, 30(49): p. 1804867.
- (10) Cook, R.L., MacDuff, R.C., and Sammells, A.F., High Rate Gas Phase CO₂ Reduction to Ethylene and Methane Using Gas Diffusion Electrodes. *J. Electrochem. Soc.* **1990**, 137(2): p. 607-608.
- (11) Park, S., Lee, J.-W., and Popov, B.N., A review of gas diffusion layer in PEM fuel cells: Materials and designs. *Int. J. Hydrogen Energy* **2012**, 37(7): p. 5850-5865.
- (12) Kim, B., Hillman, F., Ariyoshi, M., Fujikawa, S., and Kenis, P.J.A., Effects of composition of the micro porous layer and the substrate on performance in the electrochemical reduction of CO₂ to CO. *J. Power Sources* **2016**, 312: p. 192-198.
- (13) Dinh, C.-T., Burdyny, T., Kibria, M.G., Seifitokaldani, A., Gabardo, C.M., García de Arquer, F.P., Kiani, A., Edwards, J.P., De Luna, P., Bushuyev, O.S., Zou, C., Quintero-Bermudez, R., Pang, Y., Sinton, D., and Sargent, E.H., CO₂ Electroreduction to Ethylene via Hydroxide-Mediated Copper Catalysis at an Abrupt Interface. *Science* **2018**, 360(6390): p. 783-787.
- (14) Jeanty, P., Scherer, C., Magori, E., Wiesner-Fleischer, K., Hinrichsen, O., and Fleischer, M., Upscaling and continuous operation of electrochemical CO₂ to CO conversion in aqueous solutions on silver gas diffusion electrodes. *Journal of CO₂ Utilization* **2018**, 24: p. 454-462.
- (15) Burdyny, T. and Smith, W.A., CO₂ Reduction on Gas-Diffusion Electrodes and Why Catalytic Performance Must be Assessed at Commercially-Relevant Conditions. *Energy Environ. Sci.* **2019**, 12(5): p. 1442-1453.
- (16) Clark, E.L., Resasco, J., Landers, A., Lin, J., Chung, L.-T., Walton, A., Hahn, C., Jaramillo, T.F., and Bell, A.T., Data Acquisition Protocols and Reporting Standards for Studies of the Electrochemical Reduction of Carbon Dioxide. *ACS Catal.* **2018**, 8(7): p. 6560-6570.
- (17) Raciti, D., Mao, M., Park, J.H., and Wang, C., Mass transfer effects in CO₂ reduction on Cu nanowire electrocatalysts. *Catalysis Science & Technology* **2018**, 8(9): p. 2364-2369.

- (18) Lv, J.-J., Jouny, M., Luc, W., Zhu, W., Zhu, J.-J., and Jiao, F., A Highly Porous Copper Electrocatalyst for Carbon Dioxide Reduction. *Adv. Mater.* **2018**, 30(49): p. 1803111.
- (19) Ma, S., Sadakiyo, M., Luo, R., Heima, M., Yamauchi, M., and Kenis, P.J.A., One-Step Electrosynthesis of Ethylene and Ethanol from CO₂ in an Alkaline Electrolyzer. *J. Power Sources* **2016**, 301: p. 219-228.
- (20) Jouny, M., Luc, W., and Jiao, F., General Techno-Economic Analysis of CO₂ Electrolysis Systems. *Industrial & Engineering Chemistry Research* **2018**, 57(6): p. 2165-2177.

Supporting Information for Chapter 4

Modelling of the local reaction environment in Figure 4.2(a)

The local reaction environment was modelled similar to previous works and is included in this chapter to highlight operational differences between low and high current density cell operation. For the simulation, a catalyst thickness of 100 nm and porosity of 60% was assumed. The reaction selectivity was assumed to be 90% CO₂ to CO and 10% H₂ evolution, each two-electron processes. A boundary layer thickness to the bulk electrolyte of 200 μm was assumed.

Step-by-step assembly of a gas-diffusion cell for electrochemical CO₂ reduction

The assembly of a standard gas-diffusion cell for rapidly testing catalysts is shown in this section. First, the entire cell assembly is shown in Figure S4.1 followed by a step-by-step cell assembly with descriptions in Figure S4.2.

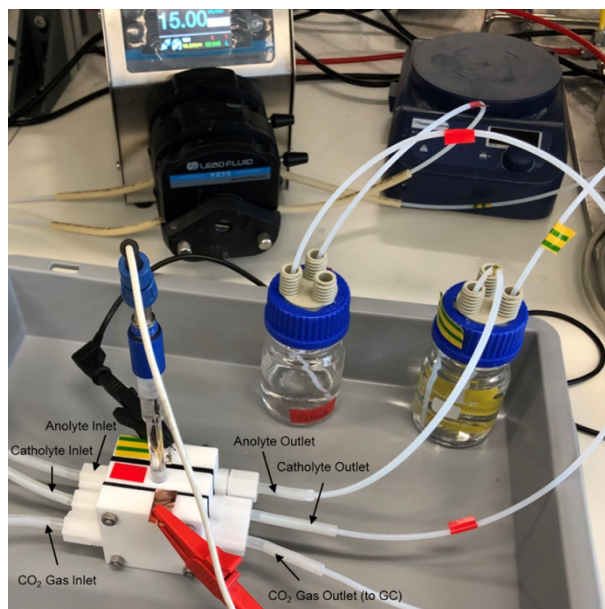


Figure S4.1: Assembled cell and labelled inlet and outlets for the electrolyte and CO₂. The catholyte and anolyte are pumped through the cell from separate reservoirs.

Starting with the anode and anolyte chamber flat on the table (a), Figures S4.2(a-j) shows assembly of the Polytetrafluoroethylene (PTFE) cell and components used for electrochemical CO₂ reduction. Figure S4.2a highlights the anolyte inlet and outlet fittings and the four bolts used to hold all components in place after assembly. Here, the cavity measures 1.5 cm by 1.5 cm with a depth of 0.8 cm. A gasket with the same hole and cavity cut-out is then placed on top of the PTFE anode chamber (Figure S4.2b), followed by a nickel or platinum mesh which functions as the anode for the oxygen evolution reaction in alkaline and neutral pH anolyte, respectively. A piece of copper or aluminium tape holds the anode in place while acting as a contact lead for the potentiostat cable external to the cell. A second gasket is then placed over top, sandwiching the anode in place and, once compressed by bolt tightening, prevents electrolyte from leaking outside the cell (Figure S4.2c). An ion-exchange membrane, here an anion exchange membrane, is then placed on top (Figure S4.2d), followed by another sealing gasket (Figure S4.2e). The PTFE catholyte compartment is then placed over top, with a port in the top for the reference electrode, enabling 3-electrode measurements of the cathode (Figure S4.2f). The gas-diffusion layer attached to a sealing gasket as described in Supplementary Video 2 is then placed on top of the catholyte chamber with the catalyst side facing down. The exposed carbon fibers from the back of the gas-diffusion layer are now visible, in addition to the copper conducting tape sealing the electrode in place (Figure S4.2g). A final gasket then seals the cathode in place (Figure S4.2h). An overhead view of the cell up to this point shows the full assembly prior to the addition of the PTFE CO₂ gas chamber (Figure S4.2i). Once the third PTFE chamber is placed on top, nuts can be applied and tightened onto the bolts, giving the complete CO₂ reduction cell in (Figure S4.2j).

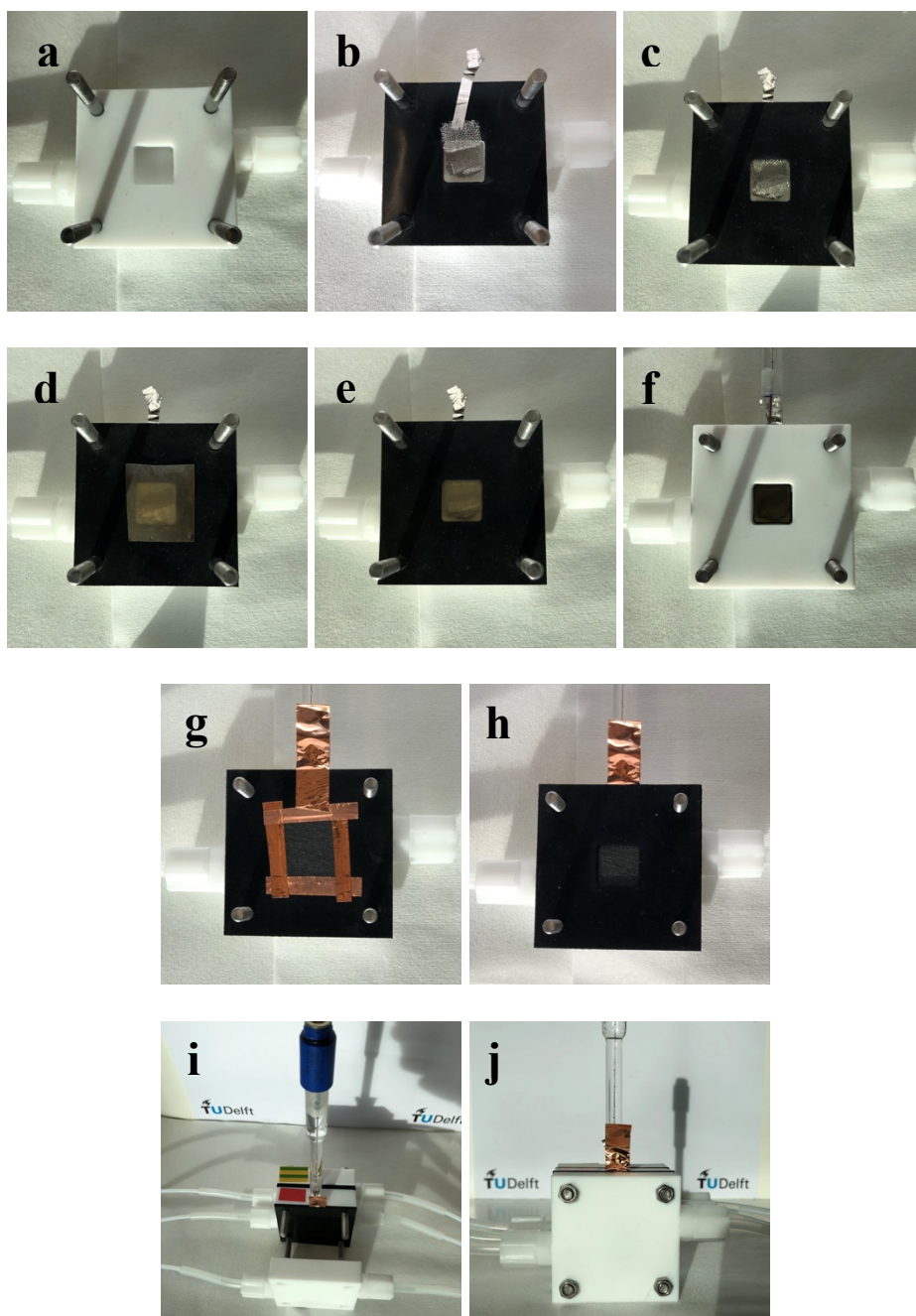


Figure S4.2: Step-by-step cell assembly as described within the supporting text.

Securing of the gas-diffusion layer to the sealing gasket

Figure S4.3 shows two methods to seal the gas-diffusion layer. On the left, conducting tape is applied around the entire sample, while on the right tape is applied only at the top of the sample. Given the relatively high resistivity of gas-diffusion layers, and the sensitivity of the CO₂ reduction reaction to both current density and potential, applying conducting tape around the entire sample is important for ensuring uniformity of the reaction on the gas-diffusion layer. Further, sample size should either be limited or the current collector should have maximum contact with the gas-diffusion electrode (e.g. copper mesh pressed against the back while still allowing gas flow).

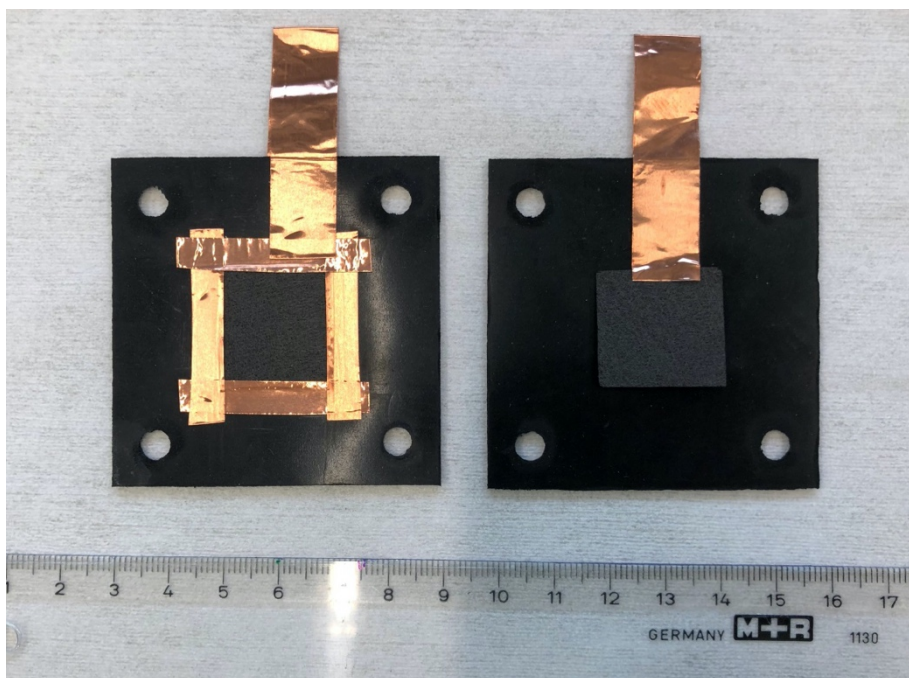


Figure S4.3: Sealing of the conducting tape to the gas-diffusion layer.

How Local Reaction and Process Conditions Influence CO₂ Reduction to Multicarbon Products on Copper Gas-Diffusion Electrodes

5

Understanding electrochemical CO₂ reduction in gas-diffusion systems is complicated by the large number of interconnected factors affecting performance. Here we show that despite observed differences in CO₂ reduction activity, selectivity and working electrode potential on copper catalysts at low current densities, experimental performance is nearly identical in 1 M KOH, KHCO₃ and KCl at 300 mA/cm². We demonstrate ethylene selectivities between 50-55% in all three electrolytes at similar corrected working potentials. By modelling both gas-phase and liquid-phase transport of reagents and products in a gas-diffusion electrode, we further find that the local reaction environment for all electrolytes converges, explaining the relative trends in performance. Using experimental selectivity and gas-channel concentrations as an input, we determine that the local CO concentration near the catalyst's surface approaches that of CO₂ due to accumulation of CO in the gas-channel and transport limitations from the immersed catalyst layer. At high enough current densities, copper electrodes performing CO₂ reduction then co-feed themselves with substantial CO, similar to the central hypotheses for developing bimetallic tandem catalysts. Unlike bimetallic systems, however, monometallic Cu is found to self-regulate CO formation as observed through plateauing partial currents. We further find that operational performance metrics, such as CO₂ single-pass conversion efficiencies, will have an impact on the activity of copper-based catalysts by changing the ratio of aqueous CO₂/CO near a catalyst's surface. These findings suggest any developed CO₂ reduction catalysts must also be adept at direct CO electrolysis at elevated current densities.

5.1 Introduction

The electrochemical reduction of carbon dioxide (CO_2) has the potential to provide a sustainable and economically attractive way to utilize the most abundant greenhouse gas to produce high-value chemicals and fuels. As a result of the intense research on this topic in the past decade, the CO_2 reduction reaction (CO_2RR) has been well studied in conventional H-type cell architectures, where researchers have examined the role of grain boundaries^[1, 2], nanostructuring^[3, 4], particle size^[5, 6], cations^[7-9], anions^[10-12] and alloying^[13-15]. However, the maximum attainable current density from CO_2RR in H-cells is approximately 20-30 mA/cm^2 for two-electron products, which is due to the low solubility of CO_2 in aqueous electrolytes^[16, 17]. Recently, the application of gas-diffusion electrodes (GDEs) for CO_2RR has rapidly increased, which has increased the maximum reaction rate of CO_2RR over ten-fold^[18, 19]. Such a configuration further allows for a high degree of nanostructuring due to the porous nature of the catalyst layer and GDE, which increases catalyst surface area and decreases overpotentials, further helping to maintain a low partial current density to the hydrogen evolution reaction (HER).

As the field has evolved, the impact of process conditions and the local reaction environment has been shown to be influential on the observed catalytic performance, particularly for CO_2 reduction on copper electrodes. The use of high pH alkaline electrolytes, for example, takes advantage of the pH-dependence of the HER, promoting CO_2 to CO conversion and carbon-carbon coupling mechanisms at low applied potentials^[20-23]. These potential and selectivity gains for CO_2RR have thus motivated the continued use of alkaline electrolytes for catalyst testing, independent of the implications for system stability as the KOH electrolyte is converted into carbonate over time.^[24] A number of researchers have then tested catalysts in pH-neutral catholytes, in membrane-electrode assemblies using only an anolyte,^[25] and in devices that utilize a fluid channel in between an anion and cation exchange membrane.^[26] In studies comparing the CO_2RR activity of catalysts in different potassium-based electrolytes for CO_2 reduction (KOH, KHCO_3 ,

KCl),^[11, 27-29] the product selectivity and working potential of the electrode were shown to be vastly different, emphasizing that the choice of electrolyte plays a large role in overall measured performance.

As the current densities reported in literature continue to increase to hundreds of mA/cm², however, we have predicted using mass transport models that most species in the reaction environment (pH, CO₂ and ion concentrations) should in fact converge.^[24, 30] We would then expect that catalytic performance should either also converge, or the remaining differences in the local environment (eg. anions) are still substantial enough to alter catalytic activity. While performance differences on copper-based catalysts for CO₂ reduction have been observed at lower current densities, it is important to see if these oft-studied differences are maintained as the local reaction environment using different electrolytes converges to be the same at elevated current densities.

Similarly, as reported current densities increase and operational parameters such as single-pass conversion efficiencies become more relevant,^[30, 31] it is becoming increasingly necessary to better understand the local concentrations of products formed in the catalyst layer, as these may impact the reactions taking place. During CO₂ reduction on copper, for example, the formation of CO as a product/intermediate has been shown to influence product selectivity in a Au-Cu tandem catalysis system, causing the ratio of oxygenates to ethylene to change.^[32] Recent efforts have also indicated that the co-feeding of CO with CO₂ also plays an extremely important role in increasing ethylene formation, with substantial C-C coupling arising between surface-adsorbed CO and dissolved CO.^[33] Given that copper electrodes produce roughly 5% CO at current densities of >200 mA/cm², it is necessary to understand how this self-production of CO impacts the observed products formed. To date, however, the discussion of local CO concentrations during CO₂ reduction has been restricted to low current density H-cell studies where transport of species (e.g. bubble nucleation/diffusion) is largely different from that of a gas-diffusion system.^[24, 34] Given the complexity of CO₂ reduction on gas-diffusion electrodes that prohibits direct product measurement in the catalyst,

mass transport modelling must then play an important role in predicting product concentrations near the catalyst's surface.

In this work, we use both experimental CO₂RR on nanostructured copper gas diffusion electrodes and reaction-diffusion modelling to determine the impact of local reaction conditions on material properties and CO₂RR selectivity in KOH, KHCO₃ and KCl electrolytes. Through current-controlled CO₂RR operation, we show that under high current densities (300 mA/cm²) the selectivity can be tuned towards similar C₂₊ products in all electrolytes regardless of the bulk pH or anions, with all electrolytes providing ethylene selectivities between 50–55%. To offer additional insights into the influence of mass transport on multicarbon product formation, we further use the experimental results to model product formation at the catalyst surface, and transport through the gas-diffusion layer to the CO₂ flow channel. We find that during CO₂ reduction on a gas-diffusion electrode at high current densities, the concentration of dissolved CO in the catalyst layer exceeds that possible in direct CO reduction. A copper catalyst then by itself provides a similar functionality proposed by tandem CO₂-to-CO and CO-to-C₂ bimetallic catalysts, despite the low CO flowrate measured in the gas channel. As we further examine these implications with our mass transport model, we find that future large-scale devices that try to maximize CO₂ utilization will cause the aqueous concentrations of produced CO to exceed that of CO₂.

5.2 Results and Discussion

5.2.1 Formulation of a simplified multi-phase reaction-diffusion model for CO₂ reduction on GDE's

As described in a number of works^[24, 34, 35], the local reaction environment surrounding the catalyst deposited onto a gas-diffusion layer can be predicted using simple reaction-diffusion models, including important values such as the local dissolved CO₂ concentration and pH. These models vary in complexity as they continue to improve. The implications of product formation in the aqueous phase and its subsequent physical transport into the porous gas-diffusion layer and into the bulk electrolyte (see Figure 5.1) are

infrequently modelled, however, despite works taking this into account in H-cell configurations.^[36] Due to the wide range of product selectivities available for CO₂RR on copper, and the potential for local CO concentrations to drive different product distributions,^[33, 37, 38] such an analysis is essential to both understand experimental results and the reactions occurring on a catalyst's surface. Without considering the transport of products throughout the system the development of new catalysts to serve a specific purpose (e.g. increasing CO production to promote carbon-carbon coupling) may be operating on an ill-formed hypothesis.

Furthermore, as higher current densities for CO₂RR are reached, and higher single-pass conversion efficiencies for CO₂ or CO reduction are achieved^[22, 27, 31, 39], the partial pressure of CO₂ in the gas-feed channel will be greatly reduced just as product concentrations will increase. As the diffusion of CO₂ through the carbon fibers and micro-porous layer of a gas diffusion layer (GDL) itself is not instantaneous and imposes transport restrictions, the reduced partial pressure of CO₂ in the gas channel will be realized as even lower partial pressures at the gas-liquid interface as shown in Figure 5.1b. The opposite will be true for potentially interesting reaction intermediates such as CO and C₂H₄, which must diffuse back to the gas channel. A product concentration gradient will then form from the liquid-immersed catalyst layer to the gas channel, causing a steady-state concentration of products to reside in the electrolyte pores of the catalyst layer. To assess the entire local reaction environment for our experimental CO₂RR results in different electrolytes, we first need to develop a transport model capable of tracking all reactive species and products in the gas phase and liquid phases of an operating gas-diffusion electrode. This will be essential to provide more accurate local concentrations of important species (CO₂, CO, C₂H₄, OH⁻) at the catalyst layer as well as all gaseous species throughout the gas-diffusion electrode.

The different regions which are modelled to achieve a 1D reaction-diffusion model are shown in Figure 5.1. These regions from left to right are the carbon fibre region of a gas-diffusion layer (Region I), the microporous layer of the gas-diffusion layer (Region II), the porous catalyst layer (Region III) and the

diffusion region of the electrolyte (Region IV). The catalyst layer is assumed to be completely immersed based upon the hydrophilicity of bare metal Cu under reduction potentials and Wenzel effects of the porous catalyst layer (Figure S5.5).^[40-42] The leftmost boundary represents the CO₂ gas channel while the rightmost boundary represents the bulk electrolyte where the compositions are assumed to remain stable as described in the Supplementary Information (SI). Here, we model the transport and reactions of CO₂, CO, C₂H₄, CH₄ and H₂ in the gas-phase, and CO₂, CO, C₂H₄, H₂, HCO₃⁻, CO₃²⁻, OH⁻, CH₄ and ethanol in the liquid-phase. The associated partial differential equations and boundary conditions describing the behaviour and transport within these regions is shown in the SI.

While this model presents gas transport in the GDE and product concentrations in the electrolyte, the mathematical construction is an extension and combination of our previous models and those of other researchers.^[24, 34, 35, 43] Thus, emphasis will be placed on the modelling results, rather than its derivation, which is described in detail in the SI. Some formulations (e.g. time-varying ‘salting out’ effects at the gas/liquid interface) that we find to be influential to system behaviour are, however, emphasized in our descriptions. Given the overall complexity of GDE systems, catalyst restructuring and progressive flooding, it is important to emphasize that mass transport models cannot realistically replicate all experimental conditions. The models are however valuable for observing trends in behaviour that can have substantial implications on local species concentrations. Changing catalyst thickness, catalyst porosity, pore sizes or using different gas-diffusion layers, for example, can drastically change maximum current densities and product selectivities on copper due primarily to changes in system mass transport, rather than catalytic properties. Further adoption of transport modelling when evaluating experimental performance is then encouraged.

Here, the system parameters used to formulate the model such as GDE thicknesses, porosity, diffusivity, multi-component gas transport are also described in detail within the SI. Importantly, the experimental CO₂RR data described in the following section were used as inputs in the simulation. Gas-chromatograph (GC) measurements were used to calculate the average composition of each gas in the gas-flow channel (see Figure 5.1a) as a function of current density and electrolyte composition. This average composition was then used for the left-hand boundary condition for the gaseous components. Similarly, measured product selectivities were used as inputs for the reactions occurring within the catalyst layer (Region III). Together, using these experimental results as model inputs provides a more accurate description of the CO₂ and CO concentrations near the surface of the catalyst. As such, conclusions from the transport model are discussed in greater detail after presentation of the electrochemical results.

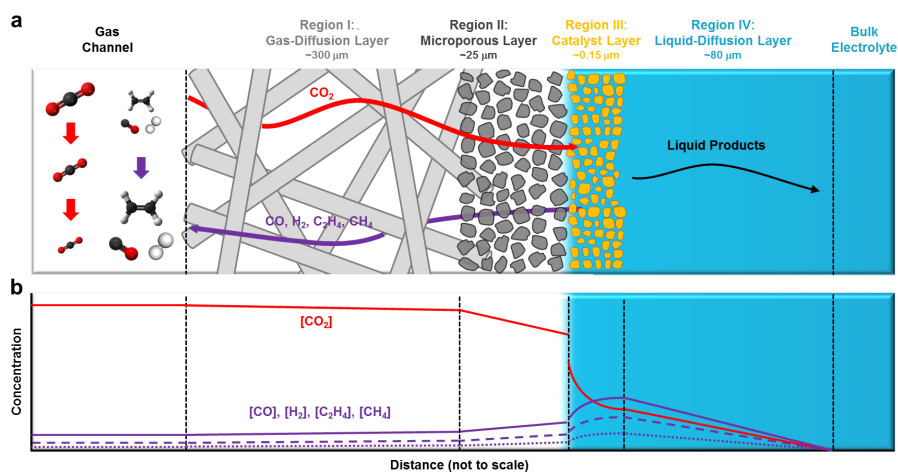


Figure 5.1: (a) Schematic of the different sections of a gas-diffusion electrode including the CO₂ gas channel, carbon fibre gas-diffusion layer, microporous layer, catalyst layer, diffusion layer and bulk electrolyte. (b) Relative concentrations of both CO₂ and gas products at various locations in the gas-diffusion electrode highlighting the deviations between gas channel concentrations and concentrations within the catalyst layer itself.

5.2.2 CO₂ reduction on copper GDE's in various electrolytes

Copper is commonly-used as a catalyst for CO₂RR due to its moderate activity and intermediate CO binding strength which allows for the production of both C₂ and C₃ hydrocarbons and alcohols. Copper is also an ideal material to examine the in-depth effects of different electrolytes, local reaction conditions and current densities due to its wide product distribution which can be significantly tuned by changing reaction conditions.^[44-46] Multicarbon product formation in particular has been experimentally shown to be heavily influenced by local CO and OH⁻ concentrations.^[36, 47] To create copper catalysts for evaluating the effects of electrolyte, current density and local environments, copper was deposited on commercial GDL's by magnetron sputtering. Deposition via sputtering provides a uniform catalyst loading with high reproducibility, while the choice of a commercial gas-diffusion layer substrate with known physical properties.

The surface analysis was performed on the as-prepared Cu-GDE catalyst and catalysts that have undergone constant current electrochemical CO₂ reduction for 1 hour at 300 mA/cm² in 1 M KOH (pH 14), 1 M CO₂-saturated KCl (pH 4) and 1 M CO₂-saturated KHCO₃ (pH 7.8) electrolytes, respectively. The CO₂RR experiments were conducted in a three-compartment flow cell which has been described previously (see Figures S5.1-S5.4).^[48] To avoid significant changes in bulk pH during operation, the reservoirs of KCl and KHCO₃ electrolytes were continuously bubbled with CO₂ and rigorously stirred. The pH of the KOH electrolyte was monitored constantly, and a large electrolyte volume was used to minimize pH and compositional changes to the bulk electrolyte.

The morphology of the samples was investigated by high resolution scanning electron microscopy (HR-SEM), shown in Figure 5.2. All samples exhibit a particulate morphology (Figure S5.4). The surface roughness of the catalyst is seen to vary between the as-prepared sample and the samples after 1 hr of electrocatalysis, likely in part to the reduction of the oxide layer during CO₂RR and restructuring of the catalyst. The electrodes demonstrate different morphologies under various electrolytes as well, however. As copper can be

oxidized to Cu-hydroxide in an alkaline solution under open circuit potential (OCP)^[19], the surface morphology in Figure 5.2b may have changed as a result of immersion in KOH. The Cu-based oxides (CuO, Cu₂O, Cu(OH)₂) are all expected to be fully reduced to metallic Cu under any CO₂ reduction potentials.^[19, 49] On the other hand, the CO₂-saturated 1 M KCl solution is mildly acidic (pH 4), which could cause Cu dissolution once the applied potential is removed, resulting in a smoother surface under OCP (Figure 5.2c). Independent of the surface nanomorphology visible in the SEM images, all samples contain similar overall copper particle sizes over the length of the 1 h experiments performed here.

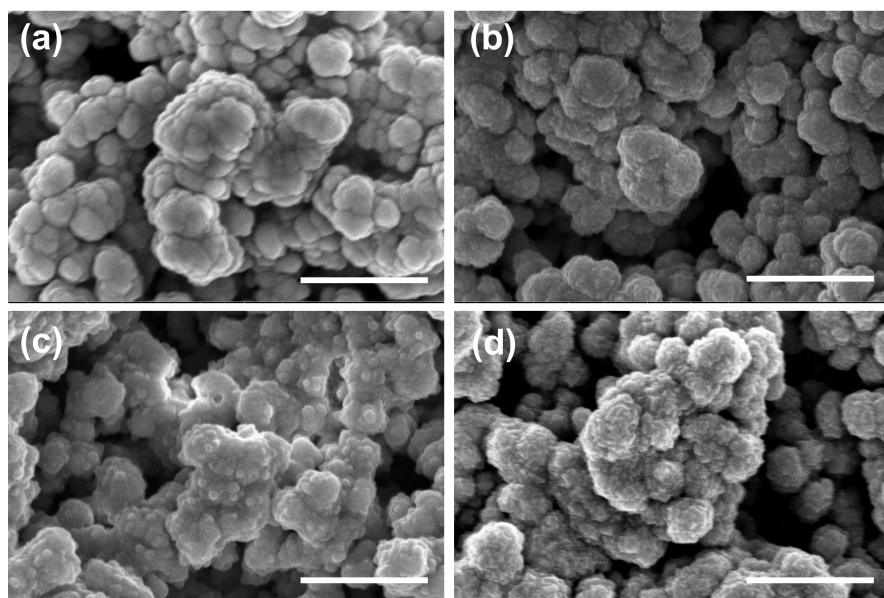


Figure 5.2: HR-SEM of the as-deposited samples before and after CO₂RR. (a) as-prepared GDE with 150 nm Cu coating layer, (b) Cu-GDE after CO₂RR in 1 M KOH for 1h, (c) Cu-GDE after CO₂RR in 1 M CO₂-saturated KCl for 1h, (d) Cu-GDE after CO₂RR in 1 M CO₂-saturated KHCO₃ for 1h. The scale bar is 400 nm.

Each of the electrodes was also examined via X-ray photoelectron spectroscopy (XPS) to determine surface composition. An XPS analysis of the as-prepared sample shows the presence of Cu₂O, which is due to the

exposure to air forming a thin oxide layer (Figure S5.7). In Figure S5.6, the dominant $2p_{3/2}$ peak at 932.7 eV indicates metallic Cu, showing that the composition of the Cu catalyst is a mixture of pure Cu and Cu-oxide. XPS performed on the electrodes post-electrolysis shows no evidence of contamination on the catalyst surface, but also supports the complete reduction of Cu oxides during CO_2RR as the Cu_2O signal was no longer present (Figure S5.7).^[49] Similarly, X-ray diffraction (XRD) of the as-prepared samples (shown in Figure S5.8) demonstrates the dominant facet of Cu is the (111) plane.

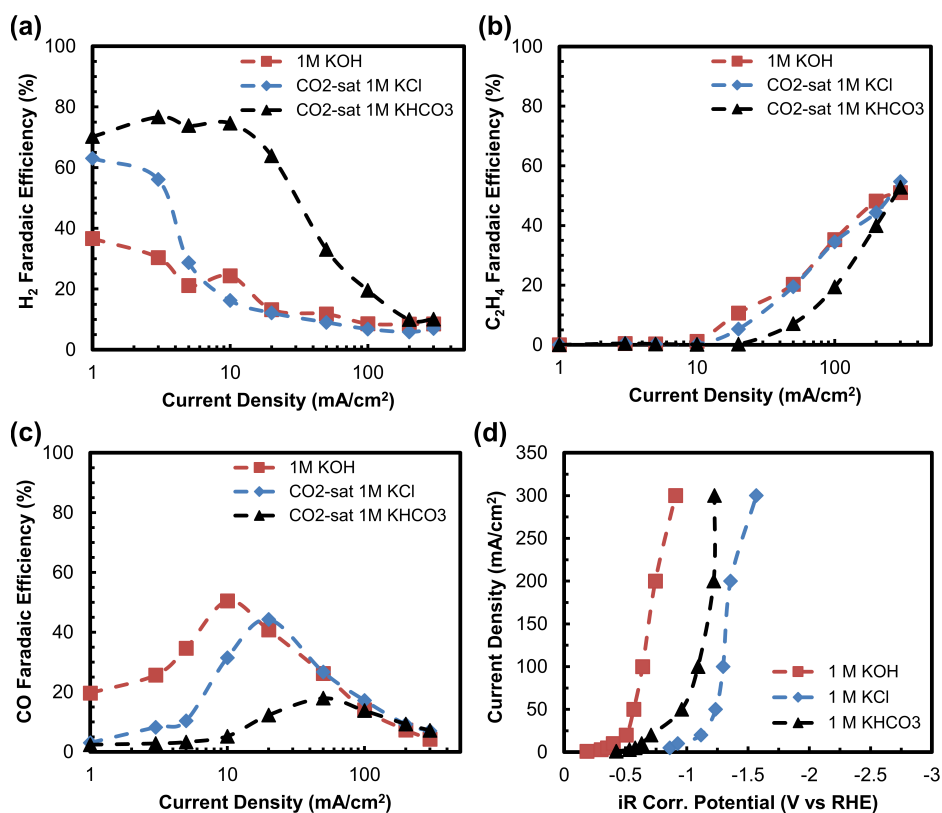


Figure 5.3: Electrochemical CO_2 reduction Faradaic efficiencies (FE) for the as-deposited Cu catalysts as a function of applied current density in 1 M KOH, KCl and KHCO_3 electrolytes. FE for (a) H_2 , (b) C_2H_4 and (c) CO. (d) Plot of the total current density versus the iR-corrected cathode potential for all electrolytes.

Electrochemical CO₂ reduction in each of the three electrolytes (KOH, KCl and KHCO₃) was then performed in the GDE cell configuration described previously^[48] using chronopotentiometry at several current densities. The gaseous (CO, H₂, C₂H₄, CH₄) and liquid (C₂H₅OH, C₃H₈O, HCOO⁻) products were analyzed by gas chromatography and nuclear magnetic resonance (NMR), respectively. Figure 5.3 and Figure S5.9 show the Faradaic efficiency (FE) for all products under several prescribed current densities. We can then observe the general trends in product selectivity as a function of the applied current density and electrolyte composition.

As the applied current density increases, the earliest onset potential for CO was observed in 1 M KOH, which has been seen in other works.^[23] In 1 M KOH, the FE for CO rises and the FE for H₂ decreases as the current density increases. The maximum achieved FE for CO is ~50% at 10 mA/cm², with no obvious formation of ethylene detected below 10 mA/cm². Once ethylene is produced at higher current densities, however, selectivity to CO starts to decrease simultaneously. It is important to note the absolute amount of CO, as determined by the partial current density (shown in Figure S5.11), plateaus instead of declining with total current density. These partial current density curves for each product are shown in Figures S5.15, while the partial current densities versus potential are plotted in Figures S5.19.

In the non-alkaline electrolytes, the peak Faradaic efficiency for CO occurs at higher current densities. In 1 M KCl a FE_{CO} peak of ~45% is obtained at 20 mA/cm², while a peak of ~17% at 50 mA/cm² is attained in 1 M KHCO₃ (Figure 5.3c). In all cases, the selectivity for CO declines in favour of C₂+ products, primarily ethylene. Similar to KOH, once a CO partial current density between 10 - 20 mA/cm² is reached, the partial current density for CO remains relatively steady even as the total current densities are increased to 300 mA/cm², as shown in Figure S5.11a.

Most importantly, despite the different onset potentials (Figure 5.3d) and current densities where the peak FE for both CO and C₂H₄ occur, the FE for both CO and C₂H₄ converges to ~5% and >50%, respectively, in all electrolytes at 300 mA/cm². For all electrolytes the selectivity towards CH₄

stays lower than 5% over the investigated current range (Figure S5.11). The convergence of product selectivities in different electrolytes at higher current densities can be further examined through the partial current densities found in Figure S5.11. While the Faradaic efficiencies rise and decrease with current density for most reaction products, the partial current densities of each product either plateaus or continues to rise as current density is increased. No product current densities are then seen to decrease as the overall current density increases, even as CO leads into multi-carbon product formation. These curves imply that over a broad examined range of current densities a steady-state amount of $\text{H}_2(\text{g})$ and $\text{CO}(\text{g})$ are produced at the catalyst's surface as the applied potential increases, despite the large observed decrease in their Faradaic efficiency. These partial current densities can be used to qualitatively discuss local species concentrations and their potential influences on reaction kinetics, in such a way, the experimental data is combined with the aforementioned transport model to quantitatively determine these values.

5.2.3 Combining experimental CO_2RR data with a reaction-diffusion model

On copper electrodes it has been well-studied experimentally that pH, CO_2 concentration and CO partial pressure^[22, 47] can impact the selectivity of CO_2RR . To better understand the relationship between the current density and the experimental FE's for C_2H_4 (>50%) from a mass transport perspective, as well as the convergence of product selectivities in different potassium based electrolytes, the above described reaction-diffusion model was utilized to calculate the local reaction environment (pH, $[\text{CO}_2]$, $[\text{CO}]$) in the catalyst layer as a function of current density and potential.^[50] To more accurately depict the phenomena occurring, two experimental results were adopted as inputs to our model: (i) the measured Faradaic efficiencies, and (ii) the measured concentrations of gases in the CO_2 flow channel from gas chromatography. These parameters then allow for CO_2 availability and physical transport of species through the gas-diffusion electrode to be factored into the calculation (Figure 5.1). The majority of previous efforts,

including our previous works^[19, 24], have generally assumed that the CO₂ concentration at the gas/liquid interface is maintained at 100% CO₂, an assumption which becomes more inaccurate as current densities and single-pass conversion efficiencies increase. Furthermore, the back diffusion of products from the liquid-immersed catalyst layer to the gas channel are usually ignored.

Using the reaction-diffusion model, the pH of the electrolyte in the catalyst layer was first predicted as a function of current density in Figure 5.4a and Figure S5.1 and shows that all three electrolytes have a predicted pH of >13 at >200 mA/cm².^[20] At lower current densities, however, the different initial pH of the three electrolytes and the buffering capacity of the 1 M KHCO₃ causes the three electrolytes to only converge at higher current densities. While the plot of pH versus current density, as shown in Figure 5.4a, highlights the local effects of buffers, Figures S5.16 and S5.17 highlight the convergence of C₂H₄ current density and Faradaic efficiency with the local pH in different electrolytes. Then we see a stronger dependence of C₂H₄ formation on the predicted pH, rather than the absolute current density or the type of electrolyte.

Another important parameter in CO₂ reduction is the working potential of the electrode. As was shown in Figure 5.3d, the iR-corrected electrode potentials required to reach 300 mA/cm² appear different for each electrolyte. When placed on an SHE scale (Figure 5.4b and Figure S5.14 and S5.15), the data from the three electrolytes align for current densities >50 mA/cm². The deviation in the measured potential at elevated current densities coincides with the predicted pH jump and an increase in multicarbon product formation (Figure S5.14). Specifically, at 300 mA/cm² where the local pH values are similar, the local-pH-corrected working potential differs by only 120 mV as compared to the 660 mV when using the bulk pH value.

Using the above information, we can use the upgraded transport model to predict the local CO₂ and CO concentrations inside the catalyst layer. The predicted molar concentrations of CO₂ and CO as a function of current density for 1 M KOH, KCl and KHCO₃ are shown in Figure 5.4c and 5.4d,

respectively. As expected, the local CO_2 concentration decreases with current density as $\text{CO}_2(\text{aq})$ is consumed in the CO_2RR and an higher concentration of hydroxide is produced by CO_2RR and HER, which can then react with the dissolved CO_2 . With these factors taken into account, the local CO_2 concentrations in all three electrolytes are within 3 mM of one another at 300 mA/cm^2 . The trend of CO concentration with total current density mimics that of the experimental partial current densities (Figure S5.11a). Interestingly, steady-state CO concentrations between 1 and 1.5 mM are reached which are higher than the saturated-CO concentration ($\sim 1 \text{ mM}$ in pure water) and similar to that of a tandem/sequential catalysts in an H-cell configuration at lower current densities.^[36-38] Unlike an H-cell, a gas-diffusion layer allows for the produced species to diffuse to the gas-liquid interface and through the GDL instead of nucleating and leaving into the bulk electrolyte.^[20] From these results, we show that a higher local concentration of dissolved CO is possible to achieve during CO_2 reduction than during direct CO reduction under environmental conditions (298 K, 1 bar) at elevated current densities. Even at CO selectivities of $<5\%$, direct CO_2 reduction then produces its own ample supply of dissolved CO, which can then undergo subsequent electrochemical reduction.

Combined, the experimental and modelling results presented here state that in all three electrolytes at 300 mA/cm^2 the reaction selectivity, local pH, CO_2 concentration, CO concentration and working electrode potential of a copper catalyst are almost identical, independent of the measured performance at lower current densities. We can then assert that current density and modelling the local reaction environment is a vitally important factor in assessing the performance of CO_2 reduction catalysts, specifically using copper catalysts for the production of multicarbon products.

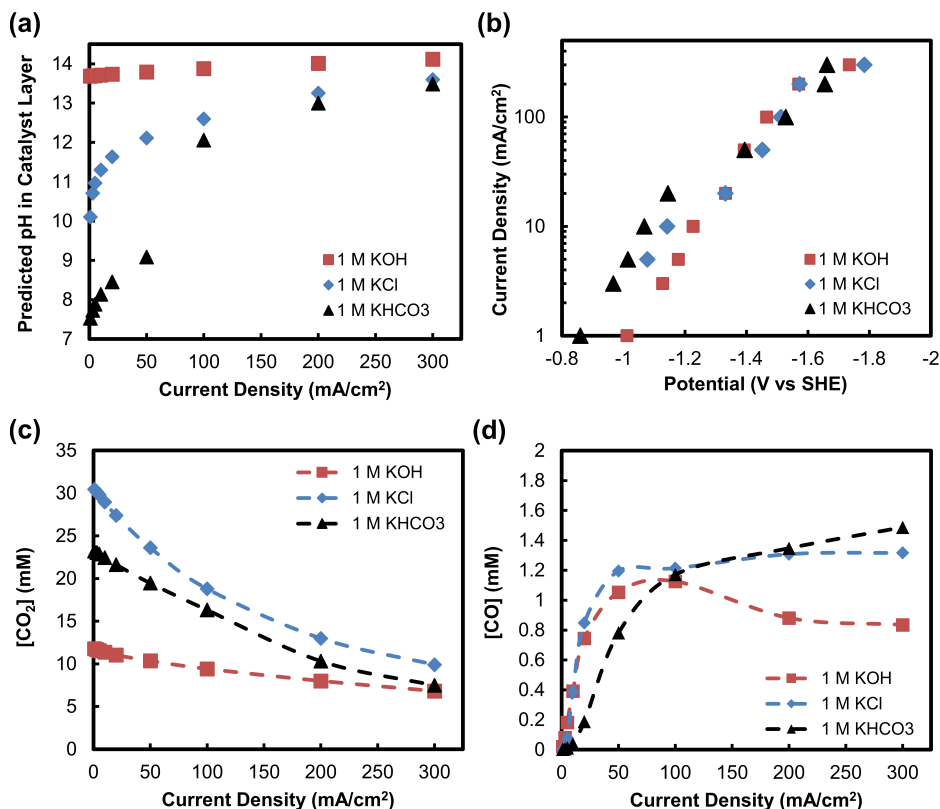


Figure 5.4: Combining the experimentally measured performance data of a copper CO_2 reduction electrode with reaction-diffusion modelling of the gas-diffusion electrode. (a) Plot of the predicted local pH as a function of the experimentally measured ethylene Faradaic efficiency for 1 M KOH, KCl and KHCO_3 electrolytes. (b) Plot of the experimental potential data that has been iR-corrected and converted to an RHE scale using the bulk pH, compared against the same data that is converted to an RHE scale using the model-predicted pH. The predicted dissolved concentrations of (c) CO_2 and (d) CO in the liquid-immersed catalyst layer. Experimental selectivities and current densities were used as model inputs. Lines are guides for the eye.

5.2.4 Mechanistic discussion of how the CO concentration influences catalytic selectivity

Using the results presented above, as well as recent literature, the impact of dissolved CO ($\text{CO}(\text{aq})$) on the catalytic activity and selectivity of CO_2

reduction on copper electrodes can be briefly discuss. In particular, an aqueous concentration of CO in the electrolyte near a catalytic surface can impact the surface coverage of protons^[51], the surface coverage of *CO and the mechanics and kinetics of C-C coupling occurring on the surface of copper electrodes during CO₂ reduction. To aid in the discussion, the partial current densities of major products obtained from the above experiments are plotted in Figure S5.11. As the impact of pH on kinetics has been discussed above and in a number of other works,^[19, 52] the discussion will focus purely on CO(aq) for brevity.

In the experimental results described above, the partial current density towards CO (Figure S5.11a) was shown to increase with the total applied current density, until plateauing between 10 - 20 mA/cm². Using our mass transport model, these experimental data translated to a relatively constant CO(aq) for all total current densities between 50 – 300 mA/cm² (Figure 5.4d). When comparing the partial current density of hydrogen and the CO₂ consumption rate within this current density range, however, we see that these two parameters increase linearly with current density as shown in Figures S5.15 and S5.20, respectively. Combined, these results imply that above current densities of ~50 mA/cm², an overall equilibrium is reached between the generation, consumption and desorption of *CO species. While an increase in C-C coupling may eventually deplete *CO and CO (aq) at high enough reaction rates, under the conditions we observed there is sufficient replenishment of CO generated from CO₂ such that we do not measure a substantial increase or decrease in the concentration of CO in the gas channel at higher current densities (Figure 5.4b). These findings on monometallic Cu are counter to those of a bimetallic Cu-Ag or Cu-Au systems where partial CO current densities on the Ag or Au particles would expect to increase with overpotential, independent of the activity on Cu.^[36, 38] An overproduction of CO is then likely as compared to a self-regulated system.

The most important kinetic implication of a mixture of dissolved CO₂ and CO is the increased mechanisms available for C-C coupling. While the primary coupling mechanism discussed for CO₂ reduction involves the combining of

two surface-bound species through a Langmuir-Hinshelwood model ($\text{*CO} + \text{*CO}$), CO reduction reports have discussed the coupling of a surface-bound species directly with CO(aq) through an Eley-Rideal mechanism ($\text{*CO} + \text{CO(aq)}$).^[33, 51, 53] The adsorbed CO in either case can be a product of CO_2 reduction, or chemisorption of CO(aq) . Importantly, recent experimental work has shown through co-feeding of isotope-labelled CO with CO_2 that the cross-coupling pathway between CO_2 -CO reagents through an Eley-Rideal mechanism resulted in almost half of all ethylene produced during reduction.^[33] Density-functional theory from the same work also indicated that under high surface coverages of *CO and high partial pressures of CO, a further *CHOO-*CO/CO(g) mechanism towards multi-carbon products may be energetically favourable as well. Combined, these studies indicate the impact that dissolved product concentrations can have on reaction pathways and emphasizes a need to model them to better understand catalytic behaviour.

5.3 Conclusions

In summary, through experiments and transport modelling we have demonstrated that CO_2RR operated on a Cu-deposited GDL under high current density exhibits similar selectivity, regardless of the initial surface state, bulk pH of electrolyte and buffer ability of anions, with three common electrolytes providing C_2H_4 selectivities between 50 - 55% at 300 mA/cm^2 . By deriving a mass transport model that encompasses the transport of both CO_2 and products through the gas-diffusion electrode, we have further created an additional tool to help assess the observed performance differences of copper catalysts. In this work we also specifically focused our attention on the concentration of aqueous CO in the catalyst layer at higher current densities, which was found to be greater than that of saturated CO even at small Faradaic efficiencies. Given that CO is persistently produced in small quantities in all cases of CO_2 reduction on copper electrodes, and CO is able to react at the electrode's surface, modelling of the local reaction environment is necessary to fully describe the observed catalytic activity. These results may also provide an additional explanation for the higher observed C_2H_4 selectivities on copper electrodes in many reported gas-diffusion layer

configurations. Finally, by extending our results to look forward to more industrial performance metrics, we conclude that optimizing CO₂ utilization of a device will have further repercussions on optimizing catalytic activity for the same reason. It is our goal that these results and the developed model stimulate further discussions on these important topics in the field moving forward.

5.4 Experimental Section

Materials. For the experiments, KHCO₃ ($\geq 97\%$), KOH (45 wt. % in H₂O), and KCl ($\geq 99.5\%$), were purchased from Sigma Aldrich. All chemicals were used without further purification. Millipore Type 1 water (18.2 M Ω) was used throughout the study to form the electrolytes.

Preparation of Cu gas-diffusion electrode. A nominal thickness of 150 nm of copper metal was deposited on gas-diffusion layer by magnetron sputtering. The deposition parameters give a rate of $\sim 1.4 \text{ \AA s}^{-1}$ on flat glass substrate. The electrochemical experiments were performed in the cell described in the previous paper.

References

- (1) Feng, X., Jiang, K., Fan, S., and Kanan, M.W., Grain-Boundary-Dependent CO₂ Electroreduction Activity. *J. Am. Chem. Soc.* **2015**, 137(14): p. 4606-4609.
- (2) Mariano, R.G., McKelvey, K., White, H.S., and Kanan, M.W., Selective Increase in CO₂ Electroreduction Activity at Grain-Boundary Surface Terminations. *Science* **2017**, 358(6367): p. 1187-1192.
- (3) Yoon, Y., Hall, A.S., and Surendranath, Y., Tuning of Silver Catalyst Mesostructure Promotes Selective Carbon Dioxide Conversion into Fuels. *Angew. Chem. Int. Ed.* **2016**, 55(49): p. 15282-15286.
- (4) Ma, M., Liu, K., Shen, J., Kas, R., and Smith, W.A., In Situ Fabrication and Reactivation of Highly Selective and Stable Ag Catalysts for Electrochemical CO₂ Conversion. *ACS Energy Lett.* **2018**, 3(6): p. 1301-1306.
- (5) Reske, R., Mistry, H., Behafarid, F., Roldan Cuenya, B., and Strasser, P., Particle Size Effects in the Catalytic Electroreduction of CO₂ on Cu Nanoparticles. *J. Am. Chem. Soc.* **2014**, 136(19): p. 6978-6986.
- (6) Zhu, W., Michalsky, R., Metin, Ö., Lv, H., Guo, S., Wright, C.J., Sun, X., Peterson, A.A., and Sun, S., Monodisperse Au Nanoparticles for Selective Electrocatalytic Reduction of CO₂ to CO. *J. Am. Chem. Soc.* **2013**, 135(45): p. 16833-16836.
- (7) Singh, M.R., Kwon, Y., Lum, Y., Ager, J.W., and Bell, A.T., Hydrolysis of Electrolyte Cations Enhances the Electrochemical Reduction of CO₂ over Ag and Cu. *J. Am. Chem. Soc.* **2016**, 138(39): p. 13006-13012.
- (8) Resasco, J., Chen, L.D., Clark, E., Tsai, C., Hahn, C., Jaramillo, T.F., Chan, K., and Bell, A.T., Promoter Effects of Alkali Metal Cations on the Electrochemical Reduction of Carbon Dioxide. *J. Am. Chem. Soc.* **2017**, 139(32): p. 11277-11287.
- (9) Akira, M. and Yoshio, H., Product Selectivity Affected by Cationic Species in Electrochemical Reduction of CO₂ and CO at a Cu Electrode. *Bull. Chem. Soc. Jpn.* **1991**, 64(1): p. 123-127.

- (10) Yun, H., Wai, O.C., and Siang, Y.B., Effects of Electrolyte Anions on the Reduction of Carbon Dioxide to Ethylene and Ethanol on Copper (100) and (111) Surfaces. *ChemSusChem* **2018**, 11(18): p. 3299-3306.
- (11) Verma, S., Lu, X., Ma, S., Masel, R.I., and Kenis, P.J.A., The Effect of Electrolyte Composition on the Electroreduction of CO₂ to CO on Ag Based Gas Diffusion Electrodes. *Phys. Chem. Chem. Phys* **2016**, 18(10): p. 7075-7084.
- (12) Ringe, S., Clark, E.L., Resasco, J., Walton, A., Seger, B., Bell, A.T., and Chan, K., Understanding cation effects in electrochemical CO₂ reduction. *Energy Environ. Sci.* **2019**, 12(10): p. 3001-3014.
- (13) Kim, D., Resasco, J., Yu, Y., Asiri, A.M., and Yang, P., Synergistic Geometric and Electronic Effects for Electrochemical Reduction of Carbon Dioxide Using Gold–Copper Bimetallic Nanoparticles. *Nat. Commun.* **2014**, 5: p. 4948.
- (14) Liu, K., Ma, M., Wu, L., Valenti, M., Cardenas-Morcoso, D., Hofmann, J.P., Bisquert, J., Gimenez, S., and Smith, W.A., Electronic Effects Determine the Selectivity of Planar Au–Cu Bimetallic Thin Films for Electrochemical CO₂ Reduction. *ACS Appl. Mater. Interfaces* **2019**, 11(18): p. 16546-16555.
- (15) Kim, D., Xie, C., Becknell, N., Yu, Y., Karamad, M., Chan, K., Crumlin, E.J., Nørskov, J.K., and Yang, P., Electrochemical Activation of CO₂ through Atomic Ordering Transformations of AuCu Nanoparticles. *J. Am. Chem. Soc.* **2017**, 139(24): p. 8329-8336.
- (16) Martin, A.J., Larrazabal, G.O., and Perez-Ramirez, J., Towards Sustainable Fuels and Chemicals through the Electrochemical Reduction of CO₂: Lessons from Water Electrolysis. *Green Chem.* **2015**, 17(12): p. 5114-5130.
- (17) Clark, E.L., Resasco, J., Landers, A., Lin, J., Chung, L.-T., Walton, A., Hahn, C., Jaramillo, T.F., and Bell, A.T., Data Acquisition Protocols and Reporting Standards for Studies of the Electrochemical Reduction of Carbon Dioxide. *ACS Catal.* **2018**, 8(7): p. 6560-6570.
- (18) Cook, R.L., MacDuff, R.C., and Sammells, A.F., High Rate Gas Phase CO₂ Reduction to Ethylene and Methane Using Gas Diffusion Electrodes. *J. Electrochem. Soc.* **1990**, 137(2): p. 607-608.

- (19) Dinh, C.-T., Burdyny, T., Kibria, M.G., Seifitokaldani, A., Gabardo, C.M., García de Arquer, F.P., Kiani, A., Edwards, J.P., De Luna, P., Bushuyev, O.S., Zou, C., Quintero-Bermudez, R., Pang, Y., Sinton, D., and Sargent, E.H., CO₂ Electroreduction to Ethylene via Hydroxide-Mediated Copper Catalysis at an Abrupt Interface. *Science* **2018**, 360(6390): p. 783-787.
- (20) Liu, X., Schlexer, P., Xiao, J., Ji, Y., Wang, L., Sandberg, R.B., Tang, M., Brown, K.S., Peng, H., Ringe, S., Hahn, C., Jaramillo, T.F., Nørskov, J.K., and Chan, K., pH effects on the electrochemical reduction of CO(2) towards C₂ products on stepped copper. *Nat. Commun.* **2019**, 10(1): p. 32.
- (21) Hoang, T.T.H., Verma, S., Ma, S., Fister, T.T., Timoshenko, J., Frenkel, A.I., Kenis, P.J.A., and Gewirth, A.A., Nano Porous Copper-Silver Alloys by Additive-Controlled Electrodeposition for the Selective Electroreduction of CO₂ to Ethylene and Ethanol. *J. Am. Chem. Soc.* **2018**, 140(17): p. 5791-5797.
- (22) Jouny, M., Luc, W., and Jiao, F., High-Rate Electroreduction of Carbon Monoxide to Multi-Carbon Products. *Nat. Catal.* **2018**, 1(10): p. 748-755.
- (23) Verma, S., Hamasaki, Y., Kim, C., Huang, W., Lu, S., Jhong, H.-R.M., Gewirth, A.A., Fujigaya, T., Nakashima, N., and Kenis, P.J.A., Insights into the Low Overpotential Electroreduction of CO₂ to CO on a Supported Gold Catalyst in an Alkaline Flow Electrolyzer. *ACS Energy Lett.* **2018**, 3(1): p. 193-198.
- (24) Burdyny, T. and Smith, W.A., CO₂ Reduction on Gas-Diffusion Electrodes and Why Catalytic Performance Must be Assessed at Commercially-Relevant Conditions. *Energy Environ. Sci.* **2019**, 12(5): p. 1442-1453.
- (25) Salvatore, D.A., Weekes, D.M., He, J., Dettelbach, K.E., Li, Y.C., Mallouk, T.E., and Berlinguette, C.P., Electrolysis of Gaseous CO₂ to CO in a Flow Cell with a Bipolar Membrane. *ACS Energy Lett.* **2018**, 3(1): p. 149-154.
- (26) Xia, C., Zhu, P., Jiang, Q., Pan, Y., Liang, W., Stavitsk, E., Alshareef, H.N., and Wang, H., Continuous production of pure liquid fuel solutions via electrocatalytic CO₂ reduction using solid-electrolyte devices. *Nat. Energy* **2019**, 4(9): p. 776-785.
- (27) Lv, J.-J., Jouny, M., Luc, W., Zhu, W., Zhu, J.-J., and Jiao, F., A Highly Porous Copper Electrocatalyst for Carbon Dioxide Reduction. *Adv. Mater.* **2018**, 30(49): p. 1803111.

- (28) Kim, B., Ma, S., Molly Jhong, H.-R., and Kenis, P.J.A., Influence of Dilute Feed and pH on Electrochemical Reduction of CO₂ to CO on Ag in a Continuous Flow Electrolyzer. *Electrochim. Acta* **2015**, 166: p. 271-276.
- (29) Ma, S., Sadakiyo, M., Luo, R., Heima, M., Yamauchi, M., and Kenis, P.J.A., One-Step Electrosynthesis of Ethylene and Ethanol from CO₂ in an Alkaline Electrolyzer. *J. Power Sources* **2016**, 301: p. 219-228.
- (30) Ringe, S., Morales-Guio, C.G., Chen, L.D., Fields, M., Jaramillo, T.F., Hahn, C., and Chan, K., Double layer charging driven carbon dioxide adsorption limits the rate of electrochemical carbon dioxide reduction on Gold. *Nat. Commun.* **2020**, 11(1): p. 33.
- (31) Zheng, T., Jiang, K., Ta, N., Hu, Y., Zeng, J., Liu, J., and Wang, H., Large-Scale and Highly Selective CO₂ Electrocatalytic Reduction on Nickel Single-Atom Catalyst. *Joule* **2018**, 3(1): p. 265-278.
- (32) Li, C.W., Ciston, J., and Kanan, M.W., Electroreduction of carbon monoxide to liquid fuel on oxide-derived nanocrystalline copper. *Nature* **2014**, 508(7497): p. 504-507.
- (33) Wang, X., de Araújo, J.F., Ju, W., Bagger, A., Schmies, H., Kühl, S., Rossmeisl, J., and Strasser, P., Mechanistic reaction pathways of enhanced ethylene yields during electroreduction of CO₂-CO co-feeds on Cu and Cu-tandem electrocatalysts. *Nat Nanotech* **2019**.
- (34) Weng, L.-C., Bell, A.T., and Weber, A.Z., Modeling Gas-Diffusion Electrodes for CO₂ Reduction. *Phys. Chem. Chem. Phys* **2018**, 20(25): p. 16973-16984.
- (35) Gupta, N., Gattrell, M., and MacDougall, B., Calculation for the Cathode Surface Concentrations in the Electrochemical Reduction of CO₂ in KHCO₃ Solutions. *J. Appl. Electrochem.* **2006**, 36(2): p. 161-172.
- (36) Morales-Guio, C.G., Cave, E.R., Nitopi, S.A., Feaster, J.T., Wang, L., Kuhl, K.P., Jackson, A., Johnson, N.C., Abram, D.N., Hatsukade, T., Hahn, C., and Jaramillo, T.F., Improved CO₂ Reduction Activity towards C₂₊ Alcohols on a Tandem Gold on Copper Electrocatalyst. *Nat. Catal.* **2018**, 1(10): p. 764-771.
- (37) Lum, Y. and Ager Iii, J.W., Sequential catalysis controls selectivity in electrochemical CO₂ reduction on Cu. *Energy Environ. Sci.* **2018**, 11(10): p. 2935-2944.

- (38) Gurudayal, Perone, D., Malani, S., Lum, Y., Haussener, S., and Ager, J.W., Sequential Cascade Electrocatalytic Conversion of Carbon Dioxide to C–C Coupled Products. *ACS Appl. Energy Mater.* **2019**, 2(6): p. 4551-4559.
- (39) Ripatti, D.S., Veltman, T.R., and Kanan, M.W., Carbon Monoxide Gas Diffusion Electrolysis that Produces Concentrated C₂ Products with High Single-Pass Conversion. *Joule* **2018**, 3(1): p. 240-256.
- (40) Gim, S., Cho, K.J., Lim, H.-K., and Kim, H., Structure, Dynamics, and Wettability of Water at Metal Interfaces. *Sci. Rep.* **2019**, 9(1): p. 14805.
- (41) Zahiri, B., Sow, P.K., Kung, C.H., and Mérida, W., Active Control over the Wettability from Superhydrophobic to Superhydrophilic by Electrochemically Altering the Oxidation State in a Low Voltage Range. *Advanced Materials Interfaces* **2017**, 4(12): p. 1700121.
- (42) Nesbitt, N.T., Burdyny, T., Simonson, H., Salvatore, D., Bohra, D., Kas, R., and Smith, W.A., Liquid–Solid Boundaries Dominate Activity of CO₂ Reduction on Gas-Diffusion Electrodes. *ACS Catal.* **2020**, 10(23): p. 14093-14106.
- (43) Wu, K., Birgersson, E., Kim, B., Kenis, P.J.A., and Karimi, I.A., Modeling and Experimental Validation of Electrochemical Reduction of CO₂ to CO in a Microfluidic Cell. *J. Electrochem. Soc.* **2015**, 162(1): p. F23-F32.
- (44) Hansen, H.A., Varley, J.B., Peterson, A.A., and Nørskov, J.K., Understanding Trends in the Electrocatalytic Activity of Metals and Enzymes for CO₂ Reduction to CO. *J. Phys. Chem. Lett.* **2013**, 4(3): p. 388-392.
- (45) Hori, Y., *Electrochemical CO₂ Reduction on Metal Electrodes*, in *Modern Aspects of Electrochemistry*, C.G. Vayenas, R.E. White, and M.E. Gamboa-Aldeco, Editors. 2008, Springer New York: New York, NY. p. 89-189.
- (46) Kuhl, K.P., Cave, E.R., Abram, D.N., and Jaramillo, T.F., New Insights into the Electrochemical Reduction of Carbon Dioxide on Metallic Copper Surfaces. *Energy Environ. Sci.* **2012**, 5(5): p. 7050-7059.
- (47) Zhuang, T.-T., Pang, Y., Liang, Z.-Q., Wang, Z., Li, Y., Tan, C.-S., Li, J., Dinh, C.T., De Luna, P., Hsieh, P.-L., Burdyny, T., Li, H.-H., Liu, M., Wang, Y., Li, F., Proppe, A., Johnston, A., Nam, D.-H., Wu, Z.-Y., Zheng, Y.-R., Ip, A.H., Tan, H., Chen, L.-J., Yu, S.-H., Kelley, S.O., Sinton, D., and Sargent, E.H., Copper Nanocavities Confine Intermediates for Efficient

- Electrosynthesis of C₃ Alcohol Fuels from Carbon Monoxide. *Nat. Catal.* **2018**, 1(12): p. 946-951.
- (48) Liu, K., Smith, W.A., and Burdyny, T., Introductory Guide to Assembling and Operating Gas Diffusion Electrodes for Electrochemical CO₂ Reduction. *ACS Energy Lett.* **2019**, 4(3): p. 639-643.
- (49) Scott, S.B., Hogg, T.V., Landers, A.T., Maagaard, T., Bertheussen, E., Lin, J.C., Davis, R.C., Beeman, J.W., Higgins, D., Drisdell, W.S., Hahn, C., Mehta, A., Seger, B., Jaramillo, T.F., and Chorkendorff, I., Absence of Oxidized Phases in Cu under CO Reduction Conditions. *ACS Energy Lett.* **2019**, 4(3): p. 803-804.
- (50) Bohra, D., Chaudhry, J.H., Burdyny, T., Pidko, E.A., and Smith, W.A., Modeling the electrical double layer to understand the reaction environment in a CO₂ electrocatalytic system. *Energy Environ. Sci.* **2019**, 12(11): p. 3380-3389.
- (51) Marcel, S., Youngmin, Y., N, J.M., and Yogesh, S., Competition between H and CO for Active Sites Governs Cu Mediated Electrosynthesis of Hydrocarbon Fuels. *Angew. Chem. Int. Ed.* **2018**, 57(32): p. 10221-10225.
- (52) Wang, L., Nitopi, S.A., Bertheussen, E., Orazov, M., Morales-Guio, C.G., Liu, X., Higgins, D.C., Chan, K., Nørskov, J.K., Hahn, C., and Jaramillo, T.F., Electrochemical Carbon Monoxide Reduction on Polycrystalline Copper: Effects of Potential, Pressure, and pH on Selectivity toward Multicarbon and Oxygenated Products. *ACS Catal.* **2018**, 8(8): p. 7445-7454.
- (53) Schouten, K.J.P., Kwon, Y., van der Ham, C.J.M., Qin, Z., and Koper, M.T.M., A new mechanism for the selectivity to C1 and C2 species in the electrochemical reduction of carbon dioxide on copper electrodes. *Chem Sci* **2011**, 2(10): p. 1902.

Supporting Information for Chapter 5

Modeling of gas and liquid compositions within the gas-diffusion layer

As described in the main text, the four regions of the gas-diffusion electrode for CO₂ reduction were modeled in one-dimension using reaction-diffusion equations. These four regions are defined by the carbon fiber region of a gas-diffusion layer (Region I), the microporous layer of the gas-diffusion layer (Region II), the porous catalyst layer (Region III) and the diffusion region of the electrolyte (Region IV) as shown in Figure 5.1a. Here we describe the physical construction of the modelled system, the equations solved and their boundary conditions, relevant phenomena, and the limitations of the model.

Physical construction of the modeled system

Sigracet® 39BC gas-diffusion layers were used in all experiments, and the properties of these layers assumed based upon a mixture of the manufacturers specifications (see SGL Carbon White Papers) and literature reporting similar structures.^[1] Region I is assumed to have a thickness of 300 μm, porosity of 80% and average pore radii (for calculation of Knudsen diffusion) of 25 μm. Region II is assumed to have a thickness of 25 μm, porosity of 30% and average pore radii (for calculation of Knudsen diffusion) of 50 nm. The catalyst layer in Region III has a thickness of roughly 150 nm as determined by controlled magnetron sputtering and an assumed porosity of 60% which is similar to a bed of packed spheres. And Region IV has an assumed boundary layer thickness of 80 μm which falls within the reported range for most electrochemical CO₂ reduction experiments.

Effective diffusion coefficients

The effective diffusion coefficients of each species in the modelled system were determined by Region. In the gas-phase regions (I and II) multicomponent gas diffusion of a mixture was used to determine the effective diffusion coefficient. Included in this effective coefficient is the mass-averaged Stefan-Maxwell diffusivity (D_i^m) and Knudsen diffusivity (D_i^K) as similarly used elsewhere.^[1]

$$D_i^{avg} = \left(\frac{1}{D_i^m} + \frac{1}{D_i^K} \right)^{-1} \quad (S1)$$

$$D_i^m = \frac{1-y_i}{\sum_{n \neq i} \frac{y_n}{D_{i,n}}} \quad (S2)$$

$$D_i^K = \frac{2}{3} r_{p,m} \sqrt{\frac{8RT}{\pi M_i}} \quad (S3)$$

where y_i is the molar fraction and M_i is the molar mass of each species, R is the universal gas constant, T is the temperature. The binary diffusion coefficients ($D_{i,n}$) were determined using the kinetic theory of gases using results from the Chapman–Enskog theory based on the Lennard–Jones potential^[2] and calculated using a Wolfram Demonstrator Project.^[3] It is important to note that these are assumed to be approximate based upon the gas mixture and a much more rigorous molecular study would be needed for higher accuracies. From the above theory the below binary diffusion coefficients used at 1.1 bar where the experiments took place, and the coefficients at 1 bar for completeness:

Table S5.1: Binary diffusion coefficients in the gas-phase in ($\text{m}^2 \text{s}^{-1}$) at $P = 1.1$ bar and $T = 298.15$ K.

$D_{\text{CO}_2, \text{CO}}$	$D_{\text{CO}_2, \text{H}_2}$	$D_{\text{CO}_2, \text{C}_2\text{H}_4}$	$D_{\text{CO}, \text{H}_2}$	$D_{\text{CO}, \text{C}_2\text{H}_4}$	$D_{\text{H}_2, \text{C}_2\text{H}_4}$	$D_{\text{H}_2, \text{CH}_4}$	$D_{\text{CO}_2, \text{CH}_4}$	$D_{\text{C}_2\text{H}_4, \text{CH}_4}$	$D_{\text{CO}, \text{CH}_4}$
1.373e-5	5.749e-5	1.028e-5	6.994e-5	1.471e-5	5.361e-5	6.563e-5	1.501e-5	1.483e-5	1.969e-5

Table S5.2: Binary diffusion coefficients in the gas-phase in ($\text{m}^2 \text{s}^{-1}$) at $P = 1$ bar and $T = 298.15$ K.

$D_{\text{CO}_2, \text{CO}}$	$D_{\text{CO}_2, \text{H}_2}$	$D_{\text{CO}_2, \text{C}_2\text{H}_4}$	$D_{\text{CO}, \text{H}_2}$	$D_{\text{CO}, \text{C}_2\text{H}_4}$	$D_{\text{H}_2, \text{C}_2\text{H}_4}$	$D_{\text{H}_2, \text{CH}_4}$	$D_{\text{CO}_2, \text{CH}_4}$	$D_{\text{C}_2\text{H}_4, \text{CH}_4}$	$D_{\text{CO}, \text{CH}_4}$
1.151e-5	6.324e-5	1.131e-5	7.694e-5	1.618e-5	5.897e-5	7.219e-5	1.651e-5	1.632e-5	2.166e-5

In the liquid phase (Regions III and IV), the diffusion coefficients of each species in water were assumed at infinite dilution as in Table S5.3.

Table S5.3: List of liquid diffusion coefficients in ($\text{m}^2 \text{s}^{-1}$).

D_{CO_2}	$D_{HCO_3^-}$	$D_{CO_3^{2-}}$	D_{OH^-}	D_{CO}	D_{H_2}	$D_{C_2H_4}$	D_{CH_4}	D_{EtOH}
1.91e-9	1.19e-9	9.23e-10	5.273e-9	2.03e-9	4.5e-9	1.87e-9	1.84e-9	0.84e-9

All diffusion coefficients were then further corrected by the porosity and tortuosity in each of the four Regions as similarly described elsewhere and shown below.

$$D_i^{eff} = \varepsilon_{Region}^{1.5} D_i^{avg} \quad (S4)$$

where described the species being transported are $i = \{CO, CH_4, C_2H_4, H_2, HCOOH, EtOH, HCO_3^-, CO_3^{2-}, OH^-\}$. These effective diffusion coefficients were then used in the differential equations to determine the concentration of each species as a function of x .

System of partial differential equations

The partial differential equations governing the transport of species within each region is described below:

Region I – Gas-Diffusion Layer ($0 < x < 300 \mu m$):

$$\frac{\partial c_i}{\partial t} = D_{i,GDL}^{eff} \frac{\partial^2 c_i}{\partial x^2} \quad ; \text{ for } i = \{CO_2, CO, CH_4, C_2H_4, H_2\} \quad (S5)$$

where $D_{i,GDL}^{eff}$ is determined using Eqs. S1-S3, Table S5.1 and the properties of the gas-diffusion layer.

Region II – Microporous Layer ($300 \mu m < x < 325 \mu m$):

$$\frac{\partial c_i}{\partial t} = D_{i,MPL}^{eff} \frac{\partial^2 c_i}{\partial x^2} \quad ; \text{ for } i = \{CO_2, CO, CH_4, C_2H_4, H_2\} \quad (S6)$$

where $D_{i,MPL}^{eff}$ is determined using Eqs. S1-S3, Table S5.1 and the properties of the microporous layer.

Region III – Catalyst Layer ($325 \mu m < x < 325.15 \mu m$):

The equations used to describe the consumption of CO_2 , generation of OH^- and buffering reactions are similar to that of previous works.^[4, 5] Here, the product formation and diffusion are additionally included.

$$\frac{\partial[CO_2]}{\partial t} = D_{CO_2,liq} \frac{\partial^2[CO_2]}{\partial x^2} - [CO_2][OH^-]k_{1f} + [HCO_3^-]k_{1r} + R_{CO_2} \quad (S7)$$

$$\frac{\partial[HCO_3^-]}{\partial t} = D_{HCO_3^-,liq} \frac{\partial^2[HCO_3^-]}{\partial x^2} + [CO_2][OH^-]k_{1f} - [HCO_3^-]k_{1r} - [HCO_3^-][OH^-]k_{2f} + [CO_3^{2-}]k_{2r} \quad (S8)$$

$$\frac{\partial[CO_3^{2-}]}{\partial t} = D_{CO_3^{2-},liq} \frac{\partial^2[CO_3^{2-}]}{\partial x^2} + [HCO_3^-][OH^-]k_{2f} - [CO_3^{2-}]k_{2r} \quad (S9)$$

$$\frac{\partial[OH^-]}{\partial t} = D_{OH^-,liq} \frac{\partial^2[OH^-]}{\partial x^2} - [CO_2][OH^-]k_{1f} + [HCO_3^-]k_{1r} - [HCO_3^-][OH^-]k_{2f} + [CO_3^{2-}]k_{2r} - k_{w2}[OH^-][OH^+] + k_{w1} + R_{OH} \quad (S10)$$

$$\frac{\partial[H^+]}{\partial t} = D_{H^+,liq} \frac{\partial^2[H^+]}{\partial x^2} - k_{w2}[OH^-][OH^+] + k_{w1} \quad (S11)$$

$$\frac{\partial c_i}{\partial t} = D_{i,liq} \frac{\partial^2 c_i}{\partial x^2} + R_i \quad ; \text{ for } i = \{CO, CH_4, C_2H_4, H_2, HCOOH, EtOH\} \quad (S12)$$

The source and sink terms in the above equations (denoted by R) vary with current density and product selectivity. The product selectivity for $\{CO, CH_4, C_2H_4, H_2, HCOOH, EtOH\}$ were measured from the experimental results and used in the model. Here the reaction is assumed to happen volumetrically and evenly across the simulated porous catalyst layer. To account for the reduced electrolyte volume inside the catalyst layer (due to the presence of the catalyst itself), the concentrations of CO_2 and the formed products accounts for the porosity of the system. In this way a highly porous catalyst layer can have a larger concentration of CO_2 and lower concentration of products.

$$R_{CO_2} = \frac{-j}{F} \left(\frac{FE_{CO}}{n_{e,CO}} + \frac{FE_{CH_4}}{n_{e,CH_4}} + \frac{FE_{C_2H_4}}{n_{e,C_2H_4}} + \frac{FE_{HCOOH}}{n_{e,HCOOH}} + \frac{FE_{EtOH}}{n_{e,EtOH}} \right) \frac{1}{\varepsilon L_{catalyst}} \quad (S13)$$

$$R_{OH^-} = \frac{j}{F} \frac{1}{\varepsilon L_{catalyst}} \quad (S14)$$

$$R_m = \frac{-j}{F} \left(\frac{FE_i}{n_{e,i}} \right) \frac{1}{\varepsilon L_{catalyst}} \quad \text{for } i = \{CO, H_2, CH_4, C_2H_4, HCOOH\} \quad (S15)$$

Region IV – Liquid Diffusion Layer ($325.15 \mu m < x < 405.15 \mu m$):

Outside of the catalyst layer the same equations are used but without the source and sink terms applied. The homogenous buffering reactions still occur however.

$$\frac{\partial[CO_2]}{\partial t} = D_{CO_2,liq} \frac{\partial^2[CO_2]}{\partial x^2} - [CO_2][OH^-]k_{1f} + [HCO_3^-]k_{1r} \quad (S16)$$

$$\begin{aligned} \frac{\partial[HCO_3^-]}{\partial t} = & D_{HCO_3^-,liq} \frac{\partial^2[HCO_3^-]}{\partial x^2} + [CO_2][OH^-]k_{1f} - [HCO_3^-]k_{1r} - \\ & [HCO_3^-][OH^-]k_{2f} + [CO_3^{2-}]k_{2r} \end{aligned} \quad (S17)$$

$$\frac{\partial[CO_3^{2-}]}{\partial t} = D_{CO_3^{2-},liq} \frac{\partial^2[CO_3^{2-}]}{\partial x^2} + [HCO_3^-][OH^-]k_{2f} - [CO_3^{2-}]k_{2r} \quad (S18)$$

$$\begin{aligned} \frac{\partial[OH^-]}{\partial t} = & D_{OH^-,liq} \frac{\partial^2[OH^-]}{\partial x^2} - [CO_2][OH^-]k_{1f} + [HCO_3^-]k_{1r} - \\ & [HCO_3^-][OH^-]k_{2f} + [CO_3^{2-}]k_{2r} - k_{w2}[OH^-][OH^+] + k_{w1} \end{aligned} \quad (S19)$$

$$\frac{\partial[H^+]}{\partial t} = D_{H^+,liq} \frac{\partial^2[H^+]}{\partial x^2} - k_{w2}[OH^-][OH^+] + k_{w1} \quad (S20)$$

$$\frac{\partial c_i}{\partial t} = D_{i,liq} \frac{\partial^2 c_i}{\partial x^2}, \quad \text{for } i = \{CO, CH_4, C_2H_4, H_2, HCOOH, EtOH\} \quad (S21)$$

Boundary Conditions

As described in the Model Inputs and Experimental Section, the gas concentrations of CO, H₂, C₂H₄ and CH₄ in the gas channel were measured using a gas-chromatograph. The left-hand boundary condition (x = 0) then used the steady-state concentration of each component in the gas channel. The CO₂ partial pressure was then assumed to account for the remaining balance. At the right-hand boundary all species were assumed to be equal to their bulk concentrations within the electrolyte. For 1 M KHCO₃ and 1 M KCl the saturated concentrations of CO₂ were set as their saturated values after taking ‘salting out’ effects into account through Sechenov’s equation (see Equations S22-24). This matches the experiments where CO₂ was constantly purged through the electrolyte reservoirs. The concentrations of products (CO, C₂H₄, etc.) were all assumed to be equal to zero at the right-hand boundary condition at all times.

Solution of the modeled equations

The above described system of coupled parabolic partial differential equations was solved in 1-D in MATLAB using the built-in pdepe solver using the experimental data as inputs. Each parameter which depends on the

changing species concentrations over time was also adjusted accordingly to account for differences from the initial conditions. These include the solubility of CO₂ at the gas-liquid interface (which is impacted by ion concentration through Sechenov's equation) and the diffusion coefficients of each component in the gas-phase (whose binary diffusion coefficients depends on gas composition). As the simulated reaction takes place the ion concentration in the catalyst layer increases in the initial moments of the reaction, which lowers the solubility of CO₂ due to salting out effects and additional interactions between CO₂ and the formed hydroxide ions. Similarly, as product gases are formed on the electrode and diffuse into the gas-diffusion layer, the partial pressure of CO₂ is reduced over time, which reduces the partial pressure of CO₂ in the electrolyte. The changing gas composition in the electrolyte then changes the effective diffusion coefficients as described by Equation S2.

Salting out effects in the electrolyte were determined by Sechenov's equation with the following coefficients for the present ions. Here C_s is the concentration of the electrolyte present. As described above, as the reaction occurs and salt concentrates the maximum solubility of CO₂ is also adjusted:

$$\log \left(\frac{[\text{CO}_2]_{\text{aq},0}}{[\text{CO}_2]_{\text{aq}}} \right) = K_s C_s \quad (\text{S22})$$

$$K_s = \sum (h_{\text{ion}} + h_G) \quad (\text{S23})$$

$$h_G = h_{G,0} + h_T(T - 298.15) \quad (\text{S24})$$

Effects of Ions in Solution	
Ion	h_{ion}
K ⁺	0.0922
HCO ₃ ⁻	0.0967

CO_3^{2-}	0.1423
OH^-	0.0839
Cl^-	0.0318
Dissolved CO_2 Parameters	
$h_{\text{G},0}$	-0.0172
h_{T}	-0.000338

Model Inputs

The variable parameters inputted into the model include: the Faradaic efficiency of different products (FE_i) on the cathode as determined from gas-chromatography and high performance liquid chromatography (HPLC) and the current density applied (j). Since the pressure of the gas and liquid phases were also set to 1.1 bar during experiments, this pressure is used in all of the simulations. Finally the modeled system was assumed to operate steadily at 298.15 K.

For determining the predicted CO_2 and CO concentrations in the catalyst layer (see Figure 5.4c and 5.4d), the experimental selectivities of the measured products were also normalized to 100% from their experimental values. While this implies that variations in product measurement are distributed equally between the formed products and different measurement devices, we considered this assumption to be the most conservative way to compare the simulated results when experimental results deviated from 100% overall Faradaic Efficiency (e.g. 90% measured products). The consumption of CO_2 by the electrolyte, and the evaporation of water into the gas channel was not estimated in the flow rate, though this is a consideration for future work.

For the results shown in Figure 5.5, a constant current density and selectivity were assumed for all gas flow rates. This selectivity was taken from the experimental results in 1 M KOH at 300 mA/cm^2 . Furthermore, multidimensional transport effects occurring in the gas channel are excluded, meaning we assume the gases are well-mixed. This approach leads to a more conservative estimate of the CO_2/CO concentrations but assumes that mass transport within future devices is well-designed. The flow rate is also shown

as the single-pass conversion efficiency to provide a more tangible value for discussion.

Plots of the predicted pH and CO₂ concentrations within Regions III and IV

For the modelled diffusion region thickness of 80 μm , we can plot the predicted concentration profiles for a number of different experimental conditions. Here, for simplicity in comparing the results, the selectivity was fixed in all cases as equal to the experimental data from 1 M KOH at 300 mA/cm^2 . These are plotted in the supplementary figures below:

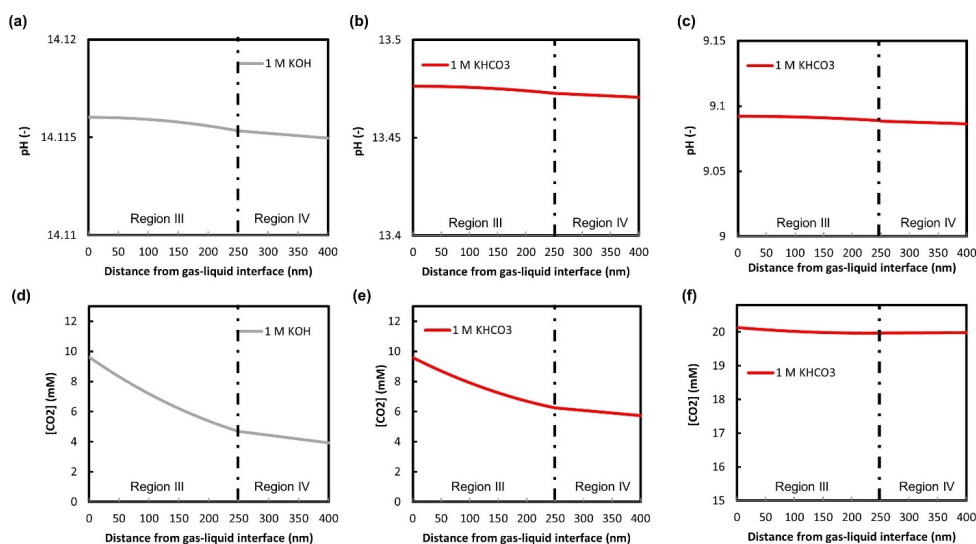


Figure S5.1: (a-c) pH profiles within the catalyst layer (Region III) and the beginning of the diffusion layer (Region IV) for a) 1 M KOH at 300 mA/cm^2 , b) 1 M KHCO₃ at 300 mA/cm^2 and c) 1 M KHCO₃ at 50 mA/cm^2 . (d-f) CO₂ concentration profiles within the catalyst layer (Region III) and the beginning of the diffusion layer (Region IV) for d) 1 M KOH at 300 mA/cm^2 , e) 1 M KHCO₃ at 300 mA/cm^2 and f) 1 M KHCO₃ at 50 mA/cm^2 .

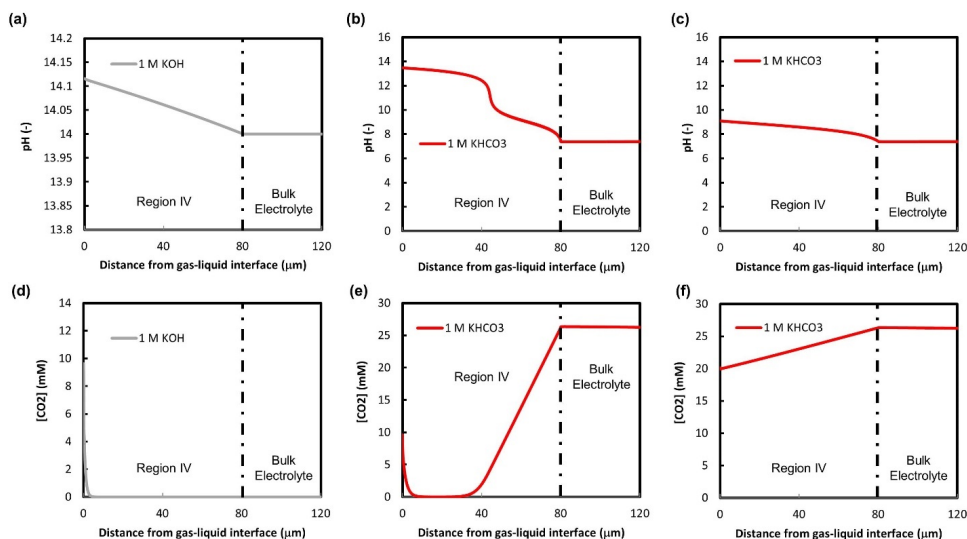


Figure S5.2: (a-c) pH profiles from the gas-liquid interface to the bulk electrolyte for a) 1 M KOH at 300 mA/cm², b) 1 M KHCO₃ at 300 mA/cm² and c) 1 M KHCO₃ at 50 mA/cm². (d-f) CO₂ concentration profiles from the gas-liquid interface to the bulk electrolyte for d) 1 M KOH at 300 mA/cm², e) 1 M KHCO₃ at 300 mA/cm² and f) 1 M KHCO₃ at 50 mA/cm².

Broader Discussion of the Modeled System and Extensions to other Experimental Devices

The modeled system here relies on experimental inputs and operating conditions, as well as the cell geometry. Here we briefly discuss the universality of our modeled CO₂ and CO concentration results based upon the construction of our system.

The most important physical parameter that can be controlled, and the one that is expected to vary the most between cell architectures and real flow electrolyzers, is the thickness of Region IV. This is the diffusion region which regulates diffusion of species into a ‘bulk electrolyte,’ which is ideally constant over thousands of hours of operation in a commercial system. As the thickness of Region IV and the bulk electrolyte shrinks to very small thicknesses we approach the classical membrane electrode assembly scenario. Within this scenario catalyst, support, ionomer and membrane interactions become very important and require 2D and 3D modeling to properly account

for. Thus while hypothesis and extension of our results to this domain are possible, it is outside the scope of the work here.

In the case where a membrane electrode assembly setup is not employed, and the catholyte dimensions are greater than the thickness of the diffusion layer, we do not expect any major variation from the results discussed here. This is because the dimensions and flow profile of the liquid catholyte channel will only influence the thickness of the diffusion region (Region IV), which will always be on the order of microns. The nanoscale transport occurring in Regions II and III will then dominate the observed behaviour and our simulated results. As the liquid diffusion pathway (Region IV) approaches the length scales of Regions II and III then its effects on the predicted CO_2 , CO , and pH are more impactful. This can be seen in Figure S5.3 below for the modelling data for 1 M KOH and KHCO_3 at different diffusion region thicknesses.

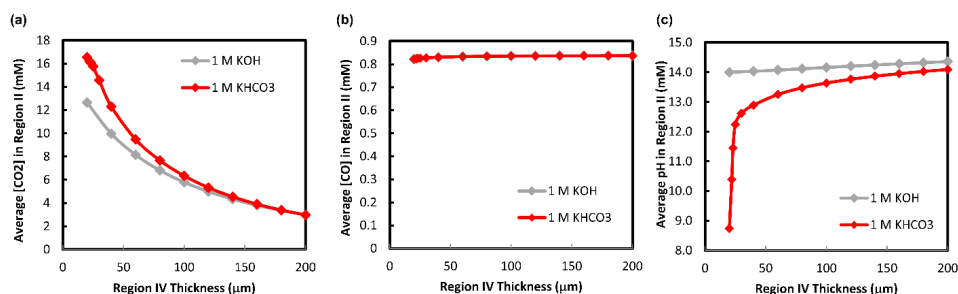


Figure S5.3: Variation of (a) CO_2 concentration, (b) CO concentration and (c) pH as a function of varying diffusion layer thickness for 1 M KOH and 1 M KHCO_3 . In all simulations the experimental selectivities were taken from 1 M KOH at 300 mA/cm^2 for simplicity.

In this case, decreasing the diffusion layer thickness allows for the OH^- and CO_3^{2-} produced in the catalyst layer to reach the bulk catholyte in a shorter time period, lowering the steady state concentration. This in turn increases the local concentration of CO_2 by diminishing the homogenous reactions. In practice, however, diffusion lengths of $< 50 \mu\text{m}$ are difficult to achieve in an electrolyzer due to the flow regime being laminar and high fluid velocities being limited by pressure drop in the channel. Interestingly, at low enough

diffusion thicknesses the local pH of the 1 M KHCO_3 electrolyte is possible to be maintained. The rapid pH rise and breaking of the buffer is then a combined effect between the current density and diffusion thickness, which can vary between devices depending on fluid flow in the catholyte region.

From the produced results we would not expect the absence of a membrane, or using different membranes, to make a substantial change in the conclusions of this work. This is because the transport of ions at the membrane's surface would not influence the phenomena occurring within the diffusion region as long as the bulk electrolyte composition is maintained, which is the case for the experiments performed here. For large electrolyzers, or devices where the bulk electrolyte concentration is permitted to change from its original composition, the lack of a membrane could influence the results by impacting the bulk electrolyte properties (buffering capacity, pH, bulk CO_2 concentration).

As an extension of our hypotheses for membrane electrode assemblies, the diffusion length mentioned above may become less than 1 μm , making the transport of CO_2 , H_2O , and ions increasingly complicated due to evaporation, membrane material, ionomer material, and process conditions (e.g. humidity). While these systems are thus outside the scope of this work, we can expect that mass transport from Regions II and III would become less dominant, and that of Region IV more so, although this is an extreme extension of the results in Figure S5.3. However, we believe that by understanding less complex systems with combined experiments and modeling, we can start to understand and model MEA's for CO_2 and CO reduction better in the future.

Discussion of the Modeling Approach and Outlook

Modelling of the transport and reactions of CO_2 and products during CO_2 reduction on gas-diffusion electrodes and membrane electrode assemblies is extremely important to fully-understand the experimentally observed performance. To date relatively little emphasis has been placed in experimental studies to determine how the composition of the gas stream varies with flow rate and current density, and how this may affect the reaction taking place within the catalyst layer. Similarly, the deposition of catalytic

materials onto gas-diffusion layers including loading, size, ionomer content, and distribution throughout the support can substantially impact performance^[6] but are rarely viewed through the lens of the transport and reaction of reagents and products. Here we briefly discuss the approach we have taken in the context of other modelling works.

In this study we aimed to use a simplified modelling approach to resolve the entire gas-diffusion electrode and the diffusion layer of the catholyte channel. We were then able to use experimental inputs such as the gas channel concentrations to model the distribution of CO₂ and reaction products throughout the system, particularly for CO, which itself can be further reduced. To improve the accuracy of the simplified model we tried to remove complexity in the experimental system. The catalyst was deposited onto the top of a gas-diffusion layer in a known quantity from Magnetron Sputtering and no binder was placed onto the system. We also used a flowing catholyte channel to remove the transport complexities that arise in membrane electrode assemblies where pore wetting is less certain. As described in our previous perspective article ^[4], it is then assumed in our model that the catalyst layer, which contains no binder, PTFE or carbon, is fully immersed in electrolyte. This is due to the experimentally observed wettability of the deposited catalyst layer after a potential has been applied ^[7], as well as for the high capillary pressure that would exist once electrolyte enters the catalyst layer (Region III). The combined modelling and experimental approach taken has then aimed for a simplified model to be applied to this system.

Such a reaction-diffusion model can be easily solved for large spatial and temporal domains, which provides more flexibility and allows for it to be used by experimental researchers with little expertise in transport modelling. Thus, such models are helpful to estimate the impacts of varying system conditions (catalyst layer porosity and thickness, electrolyte concentration and type, flow rate conditions, current density, etc.) and interpret selectivity and efficiency data. A reaction-diffusion model, however, does miss the effects of ion migration and ion size. Migration has been shown to be important in the electrolyte layer near the catalyst's surface (<5 nm) by forcing negatively

charged ion's away from the catalyst's surface. Within the charged pores of a porous electrode like that of the catalyst layer on a GDE, the effects of migration may be important for estimating certain parameters of the local reaction environment, particularly CO_2 concentration due to its interaction with OH^- and CO_3^{2-} . From our experience developing these more advanced models, we anticipate that as a catalyst layer pore size approaches the thickness of the double-layer, the effects of migration would become more important. Further research is then needed in this area to determine the exact implications of using a reaction-diffusion model versus more encompassing generalized modified Poisson-Nernst-Planck (GMPNP) models which further take ion size into consideration [8, 9].

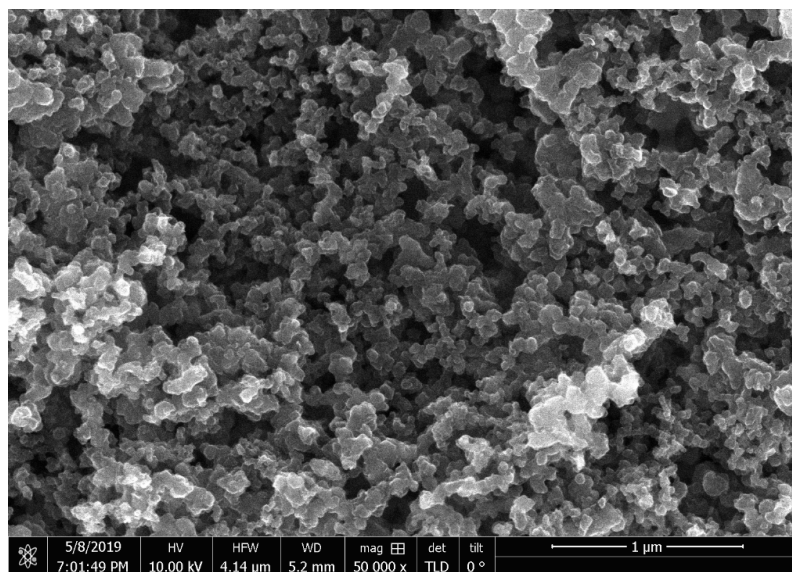
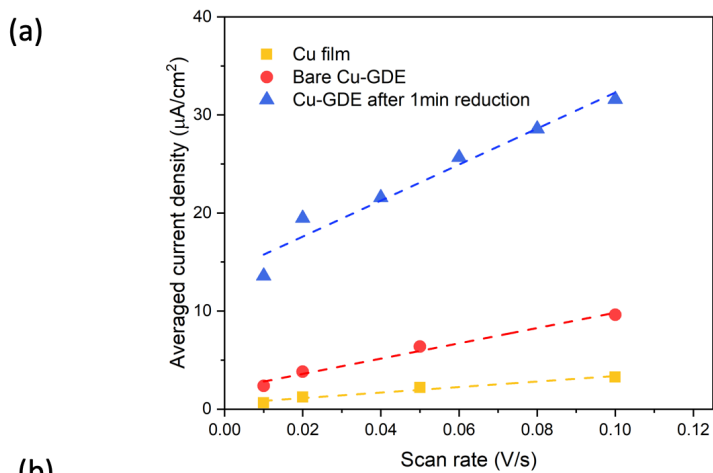


Figure S5.4: HR-SEM images of the bare GDL.



(b)

Sample	$C_{\text{double layer}} (\mu\text{F}/\text{cm}^2)$	Roughness Factor Normalized
Cu film	28.13	1.0
Pristine Cu-GDE	77.92	2.77
Cu-GDE after 1min reduction	183.52	6.52

Figure S5.5: (a) Measured double layer charging current vs. scan rate for sputtered Cu film, pristine Cu-GDE and Cu-GDE under cathodic current ($2 \text{ mA}/\text{cm}^2$) for 1 min in 0.1 M NaClO_4 in H-cell, and (b) extracted specific double layer capacitance for copper samples and corresponding roughness factors, showing significantly increased wetted surface under reduction condition.

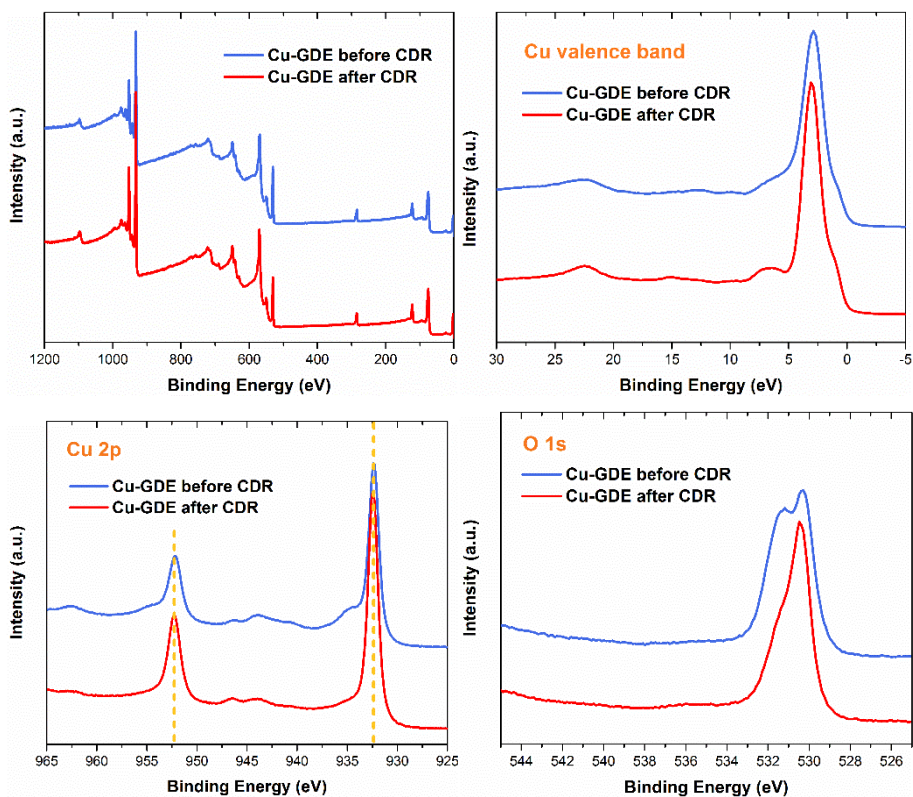


Figure S5.6: X-ray photoelectron spectroscopy of Cu-GDE before and after CO₂RR.

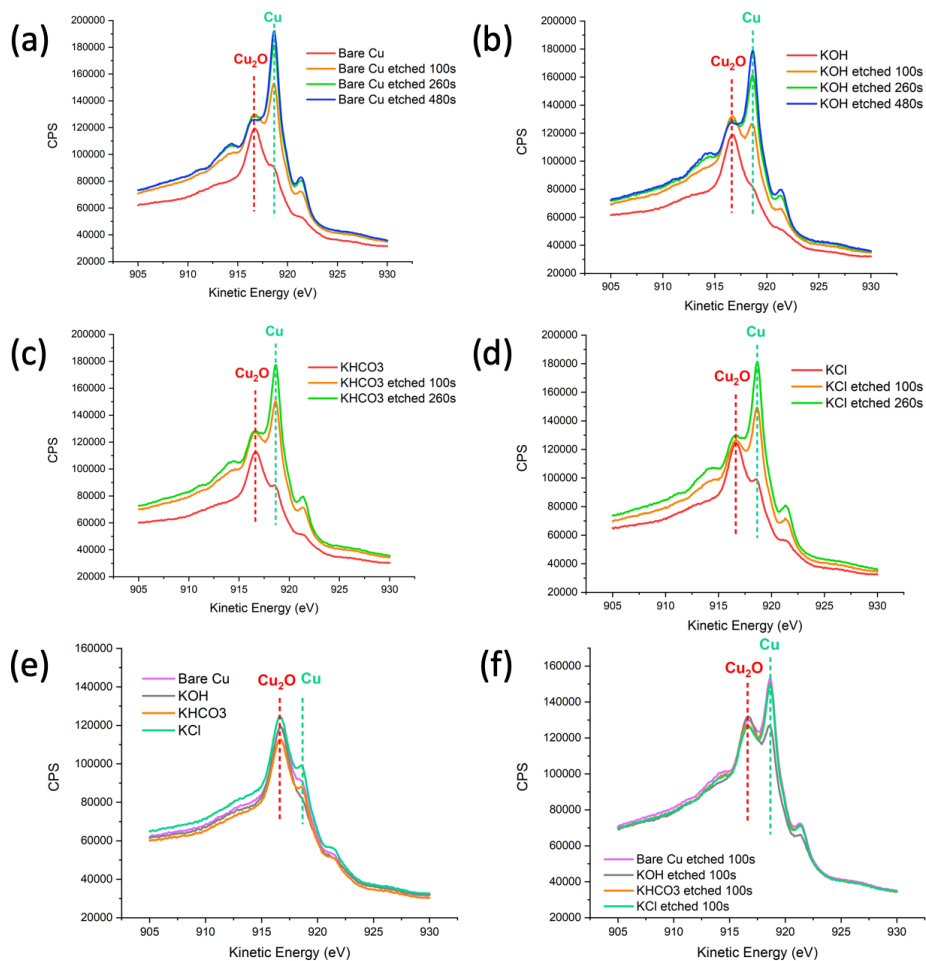


Figure S5.7: Auger XPS and depth profile XPS of copper samples, indicating ~1 nm-thick oxidation layer after exposed to air.

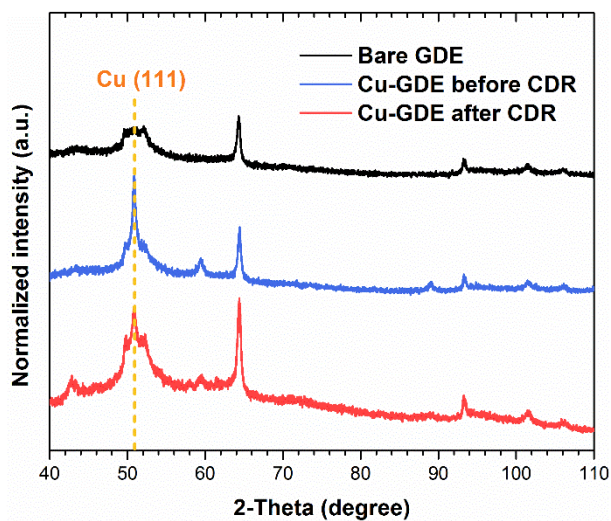


Figure S5.8: XRD pattern of Cu-GDE before and after CO₂RR.

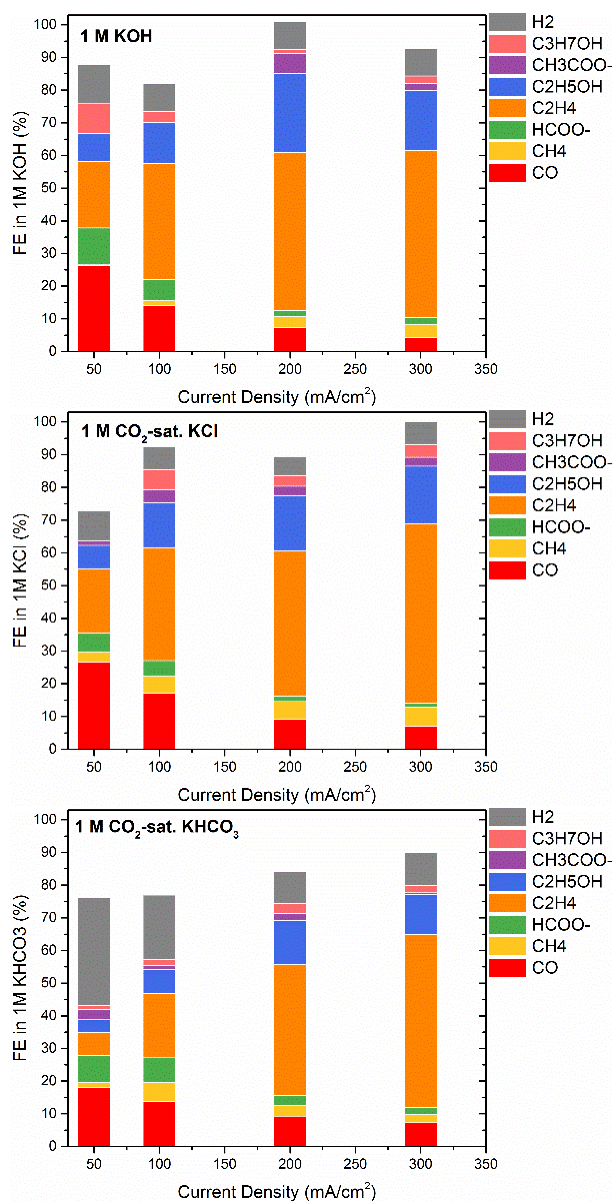


Figure S5.9: Faradaic efficiency in various electrolyte under different current density.

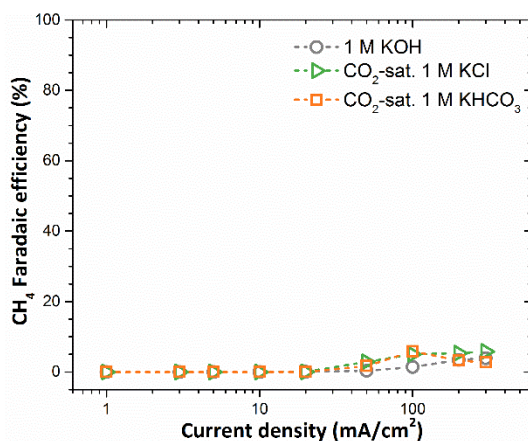


Figure S5.10: Selectivity to CH_4 in various electrolyte under different current density.

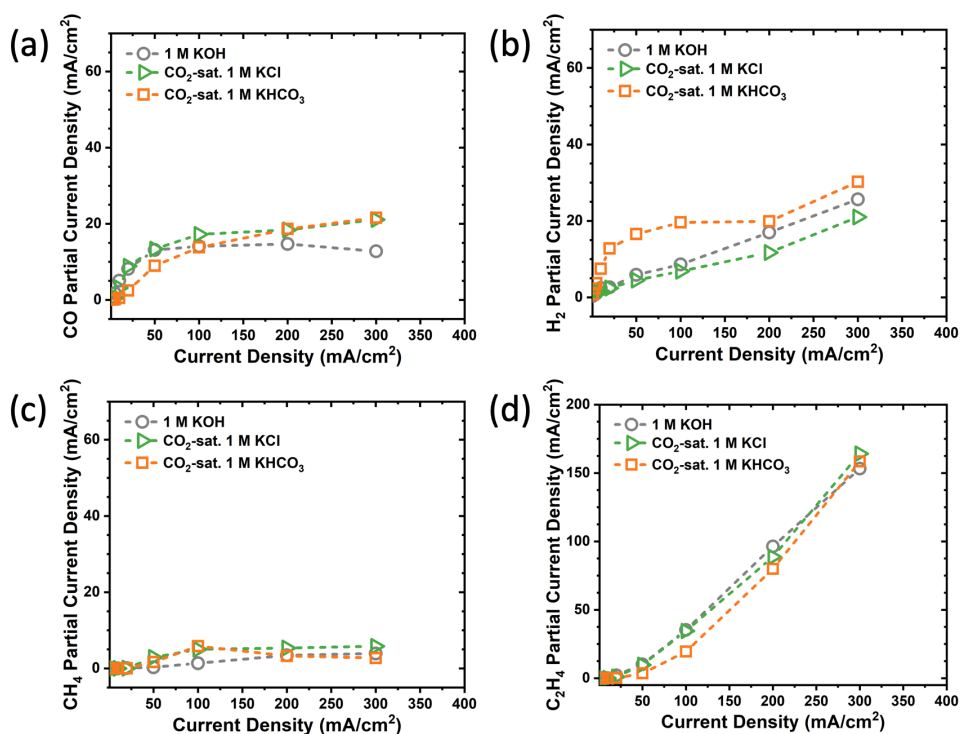


Figure S5.11: Partial current density of (a) CO , (b) H_2 , (c) CH_4 and (d) C_2H_4 in various electrolyte under different current densities.

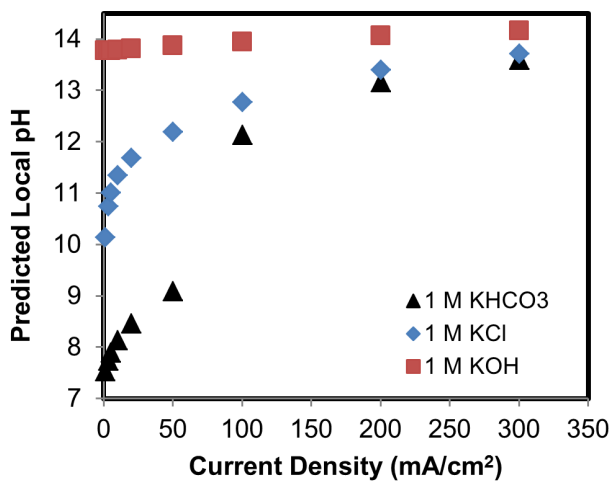


Figure S5.12: Predicted electrolyte pH in the catalyst layer as a function of current density for three electrolytes.

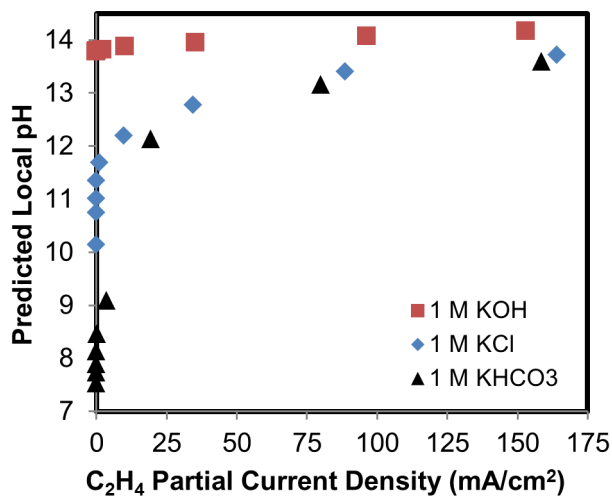


Figure S5.13: Predicted electrolyte pH in the catalyst layer as a function of the partial ethylene current density for three electrolytes.

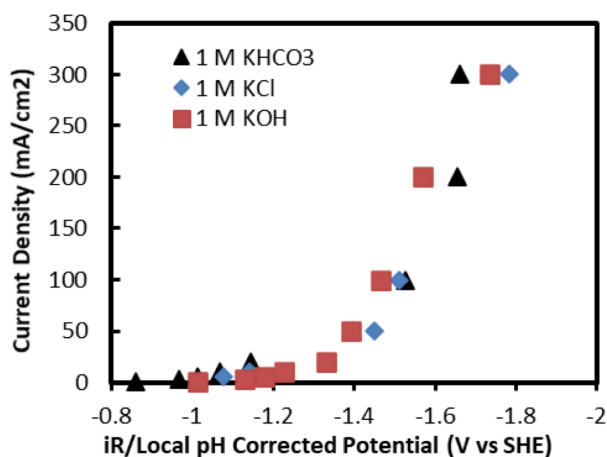


Figure S5.14: Plot of the experimental potential data on an SHE scale vs current density with a linear y-axis.

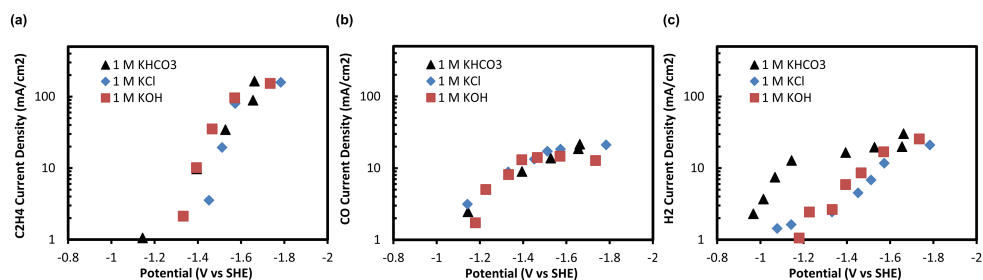


Figure S5.15: Plot of the experimental potential data on an SHE scale vs the logarithmic partial current densities of (a) ethylene, (b) carbon-monoxide, and (c) hydrogen.

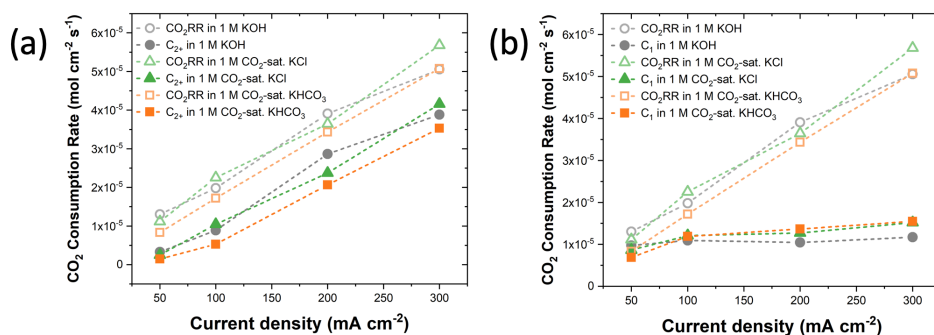


Figure S5.16: CO₂ consumption rate of overall CO₂ reduction, and (a) CO and (b) C₂₊ production rate under various current density in different electrolytes.

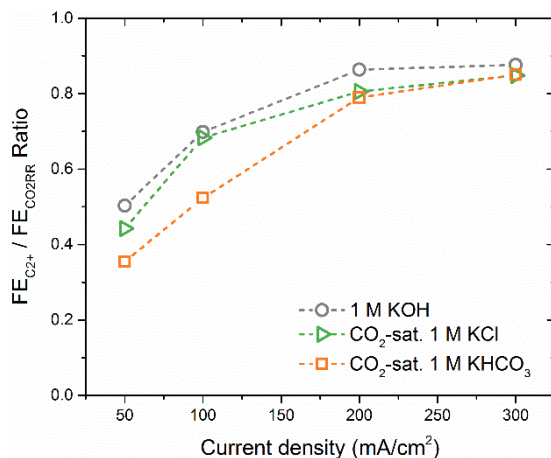


Figure S5.17: Comparison of Faradaic efficiency between total CO₂RR and the production of C₂₊ compounds.

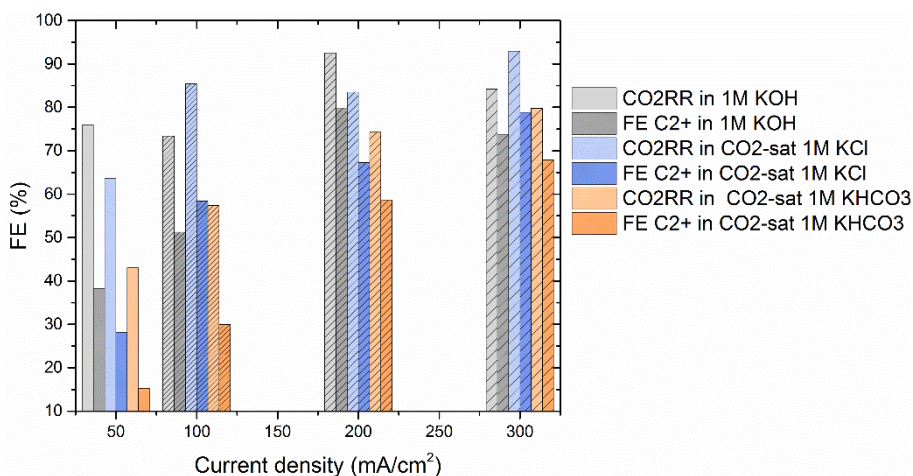


Figure S5.18: Faradaic efficiency in various electrolyte under different current density.

References

- (1) Weng, L.-C., Bell, A.T., and Weber, A.Z., Modeling Gas-Diffusion Electrodes for CO₂ Reduction. *Phys. Chem. Chem. Phys.* **2018**, 20(25): p. 16973-16984.
- (2) Bird, R., Stewart, W., and Lightfoot, E.J.N.Y., Transport Phenomena, 2nd edition John Wiley and Sons. **2002**.
- (3) Higgins, B. and Binous, H.J.W.D.P., Binary Diffusion Coefficients for Gases. **2013**.
- (4) Burdyny, T. and Smith, W.A., CO₂ Reduction on Gas-Diffusion Electrodes and Why Catalytic Performance Must be Assessed at Commercially-Relevant Conditions. *Energy Environ. Sci.* **2019**, 12(5): p. 1442-1453.
- (5) Dinh, C.T., Burdyny, T., Kibria, M.G., Seifitokaldani, A., Gabardo, C.M., García de Arquer, F.P., Kiani, A., Edwards, J.P., De Luna, P., Bushuyev, O.S., Zou, C., Quintero-Bermudez, R., Pang, Y., Sinton, D., and Sargent, E.H., CO₂ Electroreduction to Ethylene via Hydroxide-Mediated Copper Catalysis at an Abrupt Interface. *Science* **2018**, 360(6390): p. 783-787.
- (6) García de Arquer, F.P., Dinh, C.T., Ozden, A., Wicks, J., McCallum, C., Kirmani, A.R., Nam, D.-H., Gabardo, C., Seifitokaldani, A., Wang, X., Li, Y.C., Li, F., Edwards, J., Richter, L.J., Thorper, S.J., Sinton, D., and Sargent, E.H., CO₂ Electrolysis to Multicarbon Products at Activities Greater than 1 A cm⁻². *Science* **2020**, 367(6478): p. 661-666.
- (7) Liu, K., Smith, W.A., and Burdyny, T., Introductory Guide to Assembling and Operating Gas Diffusion Electrodes for Electrochemical CO₂ Reduction. *ACS Energy Lett.* **2019**, 4(3): p. 639-643.
- (8) Bohra, D., Chaudhry, J.H., Burdyny, T., Pidko, E.A., and Smith, W.A., Modeling the Electrical Double Layer to Understand the Reaction Environment in a CO₂ Electrocatalytic System. *Energy Environ. Sci.*, **2019**, 12(11): p. 3380-3389.
- (9) Ringe, S., Clark, E.L., Resasco, J., Walton, A., Seger, B., Bell, A.T., and Chan, K., Understanding Cation Effects in Electrochemical CO₂ Reduction. *Energy Environ. Sci.*, **2019**, 12(10): p. 3001-3014.

Summary and Outlook

The urgent threat of global warming and the demand for sustainable fuels have made the electroreduction of CO₂ a priority, due to its possibility in closed-loop cycle of carbon. The energy conversion and strategy can diminish the content of CO₂ in the atmosphere, convert renewable electricity into chemical energy and store it in chemical bonds, and gain high-value fuels or chemicals formed from CO₂ conversion. However, there is much room for the improvement of the efficiency of electrocatalytic reduction of CO₂. The inertness of CO₂ determines a large negative potential needed for sufficient electron and proton transfer. Hence, this thesis focuses on research how the catalysts and operating conditions electrochemical influence the electrochemical CO₂ reduction.

Among a wide variety of metallic catalysts for CO₂RR, Au and Cu are very attractive, as Au has shown the highest activity for the selective production of CO, and Cu has the largest range of product selectivities with the ability to form up to 16 different products. Concerning to the limitations of CO₂ reduction activity and selectivity on monometallic catalysts, alloying is considered to be one of the effective approaches to improve the catalytic performance by varying the binding strength of intermediates. In Chapter 3, to study the isolated electronic effect and remove geometric effects for CO₂ electroreduction, uniformly deposited Au-Cu bimetallic films with controlled composition were prepared. The incorporation of Au can significantly reshape the *d*-band electronic structure and notably weakens the binding strength of *CO. Similar to the planar Au-Pt alloys, the *d*-band electronic structure of Au-Cu alloys can be tuned by varying the composition to adjust the *CO binding energy in these bimetallic systems. The activity and selectivity for the reduction of CO₂ to CO was gradually improved with increasing Au content, revealing that the electronic effect itself can not solely break the linear scaling relationship without nanostructure engineering. This encourages us to explore the integrated strategies, including the system design

and operating conditions, and the unknown potentials of the well-studied catalysts thereafter.

In order to understand the unique operational considerations that can impact catalytic activity and our ability to accurately collect data, Chapter 4 discusses the intricacies of operating gas-diffusion layers for CO₂ electroreduction through three main subtopics: assembly, operation and post-analysis of data. It was found that the differences in testing/optimizing catalyst performance between traditional aqueous H-cell's and gas diffusion electrodes is not trivial, and many new protocols must be used to ensure proper sample preparation, recording of data, and product identification. However, with proper care and attention, the large field of catalyst researchers working on CO₂ electroreduction can leverage existing infrastructures to expedite the scientific development of this technology. This chapter is designed to acts as a source of information for catalyst-focused researchers looking to move to high current density catalyst testing, and reinforces the need for fundamental research performed under practical conditions.

As shown in Chapters 3 and 4, understanding electrochemical CO₂ reduction in gas-diffusion systems is complicated by the large number of interconnected factors affecting performance. Therefore, in Chapter 5 we tried to combine perform experiments and transport modelling to dig up the gas-diffusion system further. It was found that CO₂RR operated on a Cu-deposited GDL under high current density exhibits similar selectivity, regardless of the initial surface state, bulk pH of electrolyte and buffer ability of anions, with three common electrolytes providing C₂H₄ selectivities between 50 - 55% at 300 mA/cm². By deriving a mass transport model that encompasses the transport of both CO₂ and products through the gas-diffusion electrode, we have further created an additional tool to help assess the observed performance differences of copper catalysts. In Chapter 5 we also specifically focused our attention on the concentration of aqueous CO in the catalyst layer at higher current densities, which was found to be greater than that of saturated CO even at small Faradaic efficiencies. Given that CO is persistently produced in small quantities in all cases of CO₂ reduction on copper electrodes, and CO is able

to react at the electrode's surface, modelling of the local reaction environment is necessary to fully describe the observed catalytic activity. These results may also provide an additional explanation for the higher observed C_2H_4 selectivity on copper electrodes in many reported gas-diffusion layer configurations.

Finally, I would like to point out my personal outlook towards future efforts on the electrochemical conversion of CO_2 . As aiming to operate CO_2 electrolysis under high current densities (ampere grade), the electrochemical cells possessing the structures that allow direct gaseous CO_2 feed and flowing electrolyte attract more and more researchers' attention. Within these cells, the surrounding reaction environment of catalysts are dramatically changing during the high-rate electrolysis. The exploitation of in-situ/operando experimental methods, coupling with multi-scale modelling, would greatly contribute to comprehensively analyze the reaction mechanisms and local reaction environment (especially in the electrolyte/micro-porous layer region of GDE). To achieve higher efficiency and more economic outputs, the exploration would also need to be extended to the design of whole electrolysis process. Currently, the major reactants are CO_2 and H_2O , leading to very limited products. With a better understanding of the local reaction environment, the study of cathodic and anodic products with complex bonding, such as C-N bonds, will further broaden the reaction path of CO_2 , potentially and simultaneously achieving a lower whole cell voltage, higher energy efficiency and more economic benefits.

Samenvatting en Vooruitzicht

De dringende dreiging van de opwarming van de aarde en de vraag naar duurzame brandstoffen hebben de elektroreductie van CO_2 tot een prioriteit gemaakt, vanwege de mogelijkheden in een gesloten koolstofkringloop. De energieconversie en -strategie kunnen het CO_2 -gehalte in de atmosfeer verminderen, hernieuwbare elektriciteit omzetten in chemische energie en deze opslaan in chemische bindingen, waarmee hoogwaardige brandstoffen en chemicaliën kunnen worden verkregen vanuit CO_2 -conversie. Er is echter veel ruimte voor verbetering van de efficiëntie van elektrokatalytische reductie van CO_2 . De inertie van CO_2 zorgt voor een grote negatieve potentiaal die nodig is om voldoende elektronen- en protonenoverdracht te bewerkstelligen. Dit proefschrift richt zich daarom op het onderzoek van hoe de katalysatoren en operationele condities de elektrochemische CO_2 reductie beïnvloeden.

Onder de grote verscheidenheid aan metallische katalysatoren voor CO_2RR zijn Au en Cu zeer aantrekkelijk. Au heeft namelijk de hoogste activiteit laten zien voor de selectieve productie van CO, en Cu toont het grootste scala aan productselectiviteiten, met de mogelijkheid om 16 verschillende producten te vormen. Gezien de beperkingen die komen met het gebruik van monometaal katalysatoren op het gebied van activiteit en selectiviteit, worden legeringen beschouwd als een van de effectieve benaderingen om de katalytische prestaties te verbeteren door de bindingssterkte van tussenproducten te variëren. Om het geïsoleerde elektronische effect te bestuderen zonder de effecten van geometrie, werden voor Hoofdstuk 3 uniforme deposities van Au-Cu bimetaalfilms met gecontroleerde samenstelling gemaakt. De opname van Au in het Cu metaal kan de elektronische structuur van de d-band aanzienlijk hervormen en verzwakt hiermee met name de bindingssterkte van $^*\text{CO}$. Net als bij de vlakke Au-Pt-legeringen kan de elektronische structuur van de d-band in Au-Cu-legeringen worden afgestemd door de samenstelling te variëren en zo de $^*\text{CO}$ -bindingsenergie in deze bimetaalsystemen aan te passen. De activiteit en selectiviteit voor de reductie van CO_2 tot CO werd

geleidelijk verbeterd met toenemend Au-gehalte, waaruit blijkt dat het elektronische effect zelf niet alleen de lineaire schaalrelatie kan verbreken zonder nanostructuur-engineering. Dit moedigt ons aan om geïntegreerde strategieën te onderzoeken, waaronder het systeemontwerp en de operationele condities, en om te kijken naar andere onbekende mogelijkheden van de bestudeerde katalysatoren.

Om de unieke operationele overwegingen te begrijpen die van invloed kunnen zijn op de katalytische activiteit en ons vermogen om nauwkeurig gegevens te verzamelen, bespreekt hoofdstuk 4 de fijne kneepjes van het gebruik van gasdiffusielagen voor CO₂-elektroreductie via drie hoofdonderwerpen: assemblage, operatie en post-analyse van meetgegevens. Er werd vastgesteld dat de verschillen in het testen en optimaliseren van de katalysatorprestaties tussen traditionele H-cellen op water basis en gasdiffusie-elektroden niet triviaal zijn, en er veel nieuwe protocollen moeten worden opgesteld om een goede monstervoorbereiding, registratie van gegevens en productidentificatie te garanderen. Met de juiste zorg en aandacht kan het grote veld van katalysatoronderzoekers die werken aan CO₂-elektroreductie echter gebruik maken van bestaande infrastructuren om de wetenschappelijke ontwikkeling van deze technologie te versnellen. Dit hoofdstuk is bedoeld als informatiebron voor katalysator-onderzoekers die willen overstappen op het testen van katalysatoren onder hoge stroomdichtheden, en als versterking van de behoefte aan fundamenteel onderzoek dat onder praktische omstandigheden wordt uitgevoerd.

Zoals aangetoond in Hoofdstukken 3 en 4, wordt het begrijpen van elektrochemische CO₂-reductie in gasdiffusiesystemen gecompliceerd door het grote aantal onderling verbonden factoren die de prestaties beïnvloeden. Daarom hebben we in Hoofdstuk 5 geprobeerd om experimenten uit te voeren en met transportmodellering te combineren om de geheimen van het gasdiffusiesysteem verder te ontplooien. Er werd gevonden dat CO₂RR die werkt op een Cu-gedeponiseerd GDL onder hoge stroomdichtheid een vergelijkbare selectiviteit vertoont, ongeacht de initiële oppervlaktetoestand, de bulk-pH van het elektrolyt en het buffervermogen van anionen, waardoor

voor drie standaard elektrolyten vergelijkbare C_2H_4 -selectiviteiten werden gevonden tussen de 50 - 55% bij 300 mA/cm^2 . Door een massatransportmodel af te leiden dat het transport van zowel CO_2 als producten door de gasdiffusie-elektrode omschrijft, hebben we verder een extra hulpmiddel ontwikkeld om de waargenomen prestatieverschillen van koperkatalysatoren te beoordelen. In Hoofdstuk 5 hebben we onze aandacht ook specifiek gericht op de concentratie van opgelost CO in de katalysatorlaag bij hogere stroomdichtheden, die groter bleek te zijn dan die van verzadigd CO , zelfs bij kleine Faradaïsche efficiënties. Aangezien CO altijd wordt geproduceerd in kleine hoeveelheden in alle gevallen van CO_2 -reductie op koperelektroden, en CO in staat is te reageren aan het oppervlak van de elektrode, is modellering van de lokale reactieomgeving noodzakelijk om de waargenomen katalytische activiteit volledig te beschrijven. Deze resultaten kunnen ook een extra verklaring bieden voor de hoge waargenomen C_2H_4 -selectiviteit op koperelektroden in veel gerapporteerde gasdiffusielaag configuraties.

Tot slot wil ik wijzen op mijn persoonlijke visie op toekomstige inspanningen op het gebied van de elektrochemische omzetting van CO_2 . Als doel om CO_2 -elektrolyse onder hoge stroomdichtheden (ampèreklasse) te laten werken, trekken elektrochemische cellen die zowel direct gasvormige CO_2 als stromend elektrolyt kunnen benutten steeds meer aandacht van onderzoekers. Binnen deze cellen verandert de omringende reactieomgeving van katalysatoren dramatisch tijdens de razendsnelle elektrolyse. De exploitatie van in-situ/operando-experimentele methoden, gekoppeld aan multischaal modellering, zou een grote bijdrage kunnen leveren aan de uitgebreide analyse van reactiemechanismen en de lokale reactieomgeving (vooral in het elektrolyt/microporeuze laag regio van de GDE). Om een hogere efficiëntie en een profitabele economische output te bereiken, zou de verkenning ook moeten worden uitgebreid naar het gehele elektrolyseproces. Momenteel zijn de belangrijkste reactanten CO_2 en H_2O , wat leidt tot zeer beperkte producten. Met een beter begrip van de lokale reactieomgeving, zal de studie van kathodische en anodische producten met complexe bindingen, zoals C-N-bindingen, het reactiepad van CO_2 verder verbreden, waarbij tegelijkertijd

een mogelijk lagere totale celspanning kan worden bereikt, wat leidt tot hogere energie-efficiëntie en meer economische voordelen.

Acknowledgements

Finally, I am at the last stage of my PhD. Through this unforgettable journey, I received lots of reliable help, making every step count. Before hopping off at the stop of my PhD, I would like to thank everyone who has supported me to arrive here.

I would like to express my deepest appreciation to my promoters. Thanks, **Prof. Wilson Smith**, for giving me the opportunity to join this wonderful team and work with so many great people. I enjoy all of our bi-weekly meetings, which are like gas stations on the highway supplying endless motivation. Thanks for your support and trust. I also sincerely appreciate **Prof. Bernard Dam**. The wisdom elegantly shared by a senior scientist makes me rethink my work and life. Thank you so much for your helpful advice and guidance, especially in the last year of my PhD, which was full of unusual circumstances.

Words cannot express my gratitude to **Dr. Thomas Burdyny**, my co-promotor, the captain and gentleman, selfishly considered as my dear friend. I respect and thank you from the bottom of my heart. You are so responsible, considerate, and generous, thanks for all the meetings and casual talks. I'm so lucky to have your guidance through the hard times. Your overflowing teaching talent has already leaked out when you were trying to teach me some Dutch pronunciations before you are awarded 'Teacher of the Year'. We have witnessed your energy, persistence, and intelligence and your transformation from a postdoctoral to an assistant professor. You are the one that shows us how we chase our scientific careers successfully.

I would like to give my appreciation to the committee (**Dr. Simelys Hernandez**, **Dr. Yuguang Li**, **Prof. Fokko Mulder**, **Prof. Sixto Giménez**, and **Prof. Johan Padding**). Thank you for your efforts to take part in my PhD defense and evaluate my work.

Without effective collaborations, part of this thesis could never be accomplished. Special thanks to **Prof. Sixto Giménez** and **Prof. Juan**

Bisquert, for the impressive insights on electrochemical impedance spectroscopy. **Drialys Cardenas**, thank you for organizing the lab equipment and helping me with Spanish. I really enjoy the time working at Universitat Jaume I, which is wonderful and rewarding. When I struggled to set up the experiments with carbon monoxide, thanks to **Prof. Jan Philipp Hofmann** (currently at TU Darmstadt), **Longfei Wu** (currently at TU Berlin), these experiments could come true in TU Eindhoven, along with a lot of inspiring discussions in the lab.

I am also grateful to the pillars of MECS: **Prof. Fokko Mulder**, **Prof. Andreas Schmidt-Ott**, and **Prof. Hans Geerlings**, for all the shared thoughts and inspiring comments during the group meetings and coffee breaks. I would like to extend my gratitude to **Dr. Kristina Djanashvili** for the support and help when I started my study in Delft and for the professional training on NMR. Also, thanks should go to **Dr. Eduardo Mendes** for being my mentor.

Many thanks to our proficient technical staff: **Herman, Joost, Bart, Marcel, Ben, Duco, Stephen, Ruben, Astrid**, for the professional technical support and pleasant humor. Much appreciation to our friendly secretaries: **Roos, Heleen, Rajshree, Noortje**. Thank you for the assistance with all the administrative stuff, which makes the MECSians' life much easier.

Thanks should also go to my officemates: **Marijn, Nienke, Fahimeh, Erdem**, for creating such a nice atmosphere in the office. I also acknowledge the members of the MECS group: **Mark** (thanks for the summary translation and hilarious moments!), **Divya, Bartek, Digda, Recep, Nate, Giorgio, Steffen, Marco, Dowon, Hugo, Martin, Davide, Bernhard, Diana, Audrey, Kailun, Anirudh, Sanjana, Siddhartha, Jicheng Feng, Yaolin Xu**, for the talks about science and life, cheers through hard times and priceless smiling faces.

Many thanks to my friends in Delft, **Qian Liu, Meng Zhao, Ming Li, Fuweng Zhang, Chong Liu, Guanna Li, Dapeng Song, Riming Wang, Yiming Wang, Kai Zhang, Xiaohui Sun, Liangyong Chu, Anping Cao, Quan Pan, Zhen Liu, Min Wang, Xinlei Liu, Xuerui Zhang, Wenjun Yang, Meixian Shan, Dengyang Guo, Zhaolong Li**, thanks for the

interdisciplinary talks and joyful moments in the train, around the table, in the corridor or gym. **Wuyuan Zhang**, thank you for being my earnest friend and my brother all these years. Besides your help and consideration, your persistence in real life also motivates me a lot. **Ming Ma**, I'm extremely grateful to you for introducing me to join this wonderful group. **Ding Ding**, I believe you are the best Chinese PhD cook in Delft. Thanks for the delicate food and your hometown tea that cheer me up on the rainy days.

I'd like to recognize the friendship in the science community: **Mingchun Luo**, **Xingli Wang**, **Wen Ju**. I am also thankful to my supervisor during master study, **Prof. Shiwei Lin**, and my friend **Dr. Jianjun Liao**. Special acknowledgment is given to the Chinese Scholarship Council for financial support.

I would like to express my gratitude to **my parents**. Thank you for the unconditioned love, support and encouragement. I could not have undertaken this journey without **Jing**. Through those ups and downs, you are always aside to share the pains and laughs. Thank you for making my life more colorful and meaningful.

Kai Liu (刘楷)

List of publications

1. **Kai Liu**, Wilson A. Smith, Thomas Burdyny*. Introductory Guide to Assembling and Operating Gas Diffusion Electrodes for Electrochemical CO₂ Reduction. *ACS Energy Letters*, 2019, 4(3): 639-643.
Most read articles in ACS Energy Letters of 2019.
Highlighted by editors in virtual issue: "Why Seeing is Not Always Believing: Common Pitfalls in Photocatalysis and Electrocatalysis"
2. **Kai Liu**, Ming Ma, Longfei Wu, Marco Valenti, Drialy Cardenas-Morcoso, Jan P. Hofmann, Juan Bisquert, Sixto Gimenez, Wilson A. Smith. Electronic Effects Determine the Selectivity of Planar Au–Cu Bimetallic Thin Films for Electrochemical CO₂ Reduction. *ACS Applied Materials & Interfaces*, 2019, 18:16546-16555.
3. Ming Ma*, **Kai Liu**, Jie Shen, Recep Kas, Wilson A. Smith*. In Situ Fabrication and Reactivation of Highly Selective and Stable Ag Catalysts for Electrochemical CO₂ Conversion. *ACS Energy Letters*, 2018: 1301-1306.
4. Mark Sassenburg, Reinier de Rooij, Nathan Taylor Nesbitt, Recep Kas, Sanjana Chandrashekar, Nienke J. Firet, Kailun Yang, **Kai Liu**, Marijn A. Blommaert, Martin Kolen, Davide Ripepi, Wilson A. Smith, Thomas Burdyny*. Characterizing CO₂ reduction catalysts on gas diffusion electrodes: Comparing activity, selectivity and stability of transition metal catalysts. *ACS Applied Energy Materials*, 2022.
5. **Kai Liu**, Shiwei Lin*, Jianjun Liao, Nengqian Pan, Min Zeng. Synthesis and Characterization of Hierarchical Structured TiO₂ Nanotubes and Their Photocatalytic Performance on Methyl Orange. *Journal of Nanomaterials*, 2015, 2015: 8.
6. Jianjun Liao, Shiwei Lin*, Yue Yang, **Kai Liu**, Wencai Du. Highly Selective and Sensitive Glucose Sensors Based on Organic Electrochemical Transistors Using TiO₂ Nanotube Arrays-Based Gate Electrodes. *Sensors and Actuators B: Chemical*, 2015, 208: 457-463.
7. Jianjun Liao, Shiwei Lin*, **Kai Liu**, Yue Yang, Ruirui Zhang, Wencai Du, Xiaogan Li. Organic Electrochemical Transistor Based Biosensor for Detecting Marine Diatoms in Seawater Medium. *Sensors and Actuators B: Chemical*, 2014, 203: 677-682.

Curriculum Vitae

Kai Liu was born on September 2, 1989 in Shaanxi Province, China. He earned his Bachelor and Master degree in Material Science and Engineering from Hainan University in 2012 and 2015. In the same year, he started his PhD study at TU Delft. He finished his doctoral dissertation under the supervision of Prof. Wilson A. Smith, Prof. Bernard Dam and Dr. Thomas Burdyny in the Materials for Energy Conversion and Storage (MECS) group at the Chemical Engineering department. His research focuses on developing electrocatalysts to convert CO₂ into value-added chemicals within various local reaction environments to study the reaction mechanism and achieve enhanced performance.

